UNIVERSITY OF BIRMINGHAM

Lithium Ion Conductivity in Hydrogen Storage and Battery Materials

by

Matthew Howard

Supervisors: Prof. Peter Slater and Dr. Paul Anderson

A thesis submitted to The University of Birmingham

for the degree of Doctor of Philosophy

The School of Chemistry,

College of Engineering and Physical Sciences

The University of Birmingham

September 2015

Dedicated

to

my parents

Abstract

In this thesis the role of lithium ion conductivity in lithium conducting garnets as potential solid state electrolytes for lithium ion batteries and lithium halide nitrides for solid state hydrogen storage materials is researched.

The role of order and disorder on in the lithium sublattice of garnet type materials is investigated. Showing that ordering can cause a change in the unit cell symmetry resulting a tetragonal unit cell. Due to the ordering a drop in the Li ion conductivity is observed. Through a small amount of trivalent doping into the lithium sublattice it is possible to create disorder and hence a change in the unit cell to cubic and an enhancement in the conductivity.

For the first time work conducted in this thesis shows evidence for possible H^+/Li^+ exchange occurring in air. This exchange was seen to have varying effects on the low temperature lithium ion conductivity, highlighting the need to take care when preparing and measuring these materials

The structure of an antifluorite-type lithium chloride nitride were resolved following inconclusive literature reports. It is shown for the first time that it is possible for these materials to hydrogenate these materials and they have potential as possible solid state hydrogen storage materials.

The ionic conductivities of the lithium halide nitrides were measured and compared to that of lithium nitride, and their hydrogen storage properties were related to the ionic conductivity.

Acknowledgements

I would like to thank my supervisors Prof. Peter Slater and Dr. Paul Anderson for firstly giving me this opportunity and also for their guidance over the duration of my PhD.

Dr. Olli Clemens not only for his help with all things Topas based but also his friendship and humour keeping me going at all times.

Thanks go to collaborators Dr. Kevin Knight (HRPD) for his help with the neutron diffraction experiments at ISIS and Dr. David Apperley at the University of Durham NMR service for his data collection. Dr. Pooja Panchmatia at University of Huddersfield for her computational calculations. Prof. Venkataraman Thangadurai for the H^+/Li^+ studies.

Jackie Deans for welcoming me to the floor and showing me the ropes and her constant help throughout the three years at Birmingham

Floor 5 and my project students Grant, Becky, Nick and Matt for the help and friendship during my PhD and hopeful for many years to come. Special thanks to George, Geoff and Phil and their loyal support to the moor pool heritage trust.

Finally I'd like to thank my family for their love and support and especially my parents for never giving up on me.

Table of Context

1. Introduction

With fossil fuel resources running out at a fast rate, considerable research has been performed to find new ways to improve our energy network, such as the use of renewable energy technologies. One major issue with these systems is their intermittency of supply, and so there is a need to improve our energy storage capabilities to overcome these problems[1, 2]. Two ways of storing chemical energy are either in batteries, or *via* production of hydrogen and its storage. In this thesis both these areas have been researched.

With the demand for light weight, higher voltage, longer lifetime and rechargeable batteries, extensive research into new materials for Li ion batteries has been performed and some of the systems proposed for the electrolyte will be discussed with a particular focus on solid state electrolytes.

An alternative storage technology to the use of batteries is the production and storage of H_2. Hydrogen is an ideal fuel to use, as it has a high energy density, light weight and is a highly abundant element. Hydrogen can be stored either as a liquid or a gas, although both requires a substantial amount of energy to compress and cool the hydrogen to allow it be stored in large quantities safely. Research into alternative ways of storing hydrogen has been carried out worldwide. This has led to developments in metal hydrides and metal complex hydrides as potential solid state hydrogen storage materials.

In both the Li ion battery and H_2 storage areas, high ionic conduction is believed to be important to ensure good performance[3-8]. The aim of this project was to investigate the Li ionic conductivity of a range of materials (garnet-type materials for batteries and lithium halide nitrides for the hydrogen storage materials) for potential applications as solid state electrolytes or H_2 storage materials.

1.1 Ionic Conduction in Solids

Ionic conductivity is the transport of ions across a material. In an ideal crystalline material, all ions are arranged in a tightly packed regular arrangement, meaning there is little space for ions to be transported through the material[9]. However, in reality defects are present in materials. There are two types of stoichiometric defects: Schottky and Frenkel defects. A Schottky defect is defined as the removal of anion and cation pair that leaves vacant sites within the crystal as shown in figure 1.1[10].

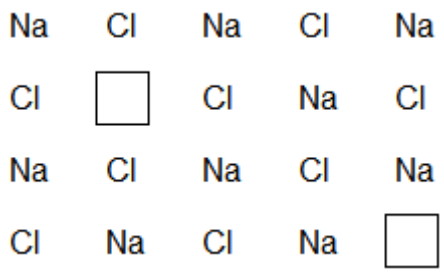

Figure 1.1 Schottky Defect in NaCl

A Frenkel defect is defined as an anion or cation moving to an interstitial site as shown in figure 1.2[11]. These types of defects are known as intrinsic defects.

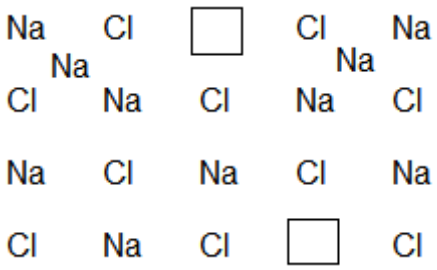

Figure 1.2 Frenkel Defect in NaCl

Defects can also occur due to variation in stoichiometry; these defects are known as extrinsic defects. Extrinsic defects can occur by doping a stoichiometric crystal with an atom which

has a different valency to that of the host crystal i.e. replacing a small amount of Na^+ with Ca^{2+} in NaCl. Here two Na cations will be replaced by one Ca cation to retain charge balance and thus creating vacancies in the cation sites.

Ion defects are essential for ionic conductivity as they allow ions to be transported *via* them. For example in the case of vacancy defects, an adjacent ion may jump into the vacancy[9]. This transfer of the ion in turn leaves a vacant site behind, in to which another ion can be accommodated; this conduction mechanism is known as vacancy migration.

For an ion to be able to move into the vacant sites created by the presence of defects in the crystal structure, it must have sufficient energy to overcome the activation energy barrier for this process. The activation energy is a key factor in determining the likelihood of these migrations. The activation energy (E_a) can be deduced from the Arrhenius expression for conductivity in equation 1.1,

$$\boldsymbol{\sigma = \left(\frac{A}{T}\right) e^{(-Ea/RT)}} \qquad \textbf{(1.1)}$$

where σ is the conductivity, T is the temperature (Kelvin), A is the pre-exponential factor, and R is the molar gas constant.

As cations generally have smaller ionic radius than anions, they are commonly the most mobile ions and this is why they have attracted a large amount of interest. Typically alkali metal cations Li^+, K^+, and Na^+, have been widely researched in this respect as the low charge is also beneficial for ionic conduction.

1.2 Electrolyte Materials in Li Ion Batteries

Rechargeable Li ion batteries require a material (solid/liquid) in which lithium ions can diffuse between the lithium containing transition metal oxide cathode to the anode, which is typically a graphite anode or some other form of carbon. This material must have high Li ion

conductivity but low electronic conductivity and is known as the electrolyte[12]. A rechargeable (secondary) battery design is shown in figure 1.3. Most work in this field has focused on liquid electrolytes, due to their typically higher ionic conductivities than solids. However, solid electrolytes do have several potential advantages, such as allowing for miniaturisation, as well as no leakage problems and improved safety (non-flammable). In this section, solid state Li ion conducting materials, which have proposed for electrolyte applications, will be discussed.

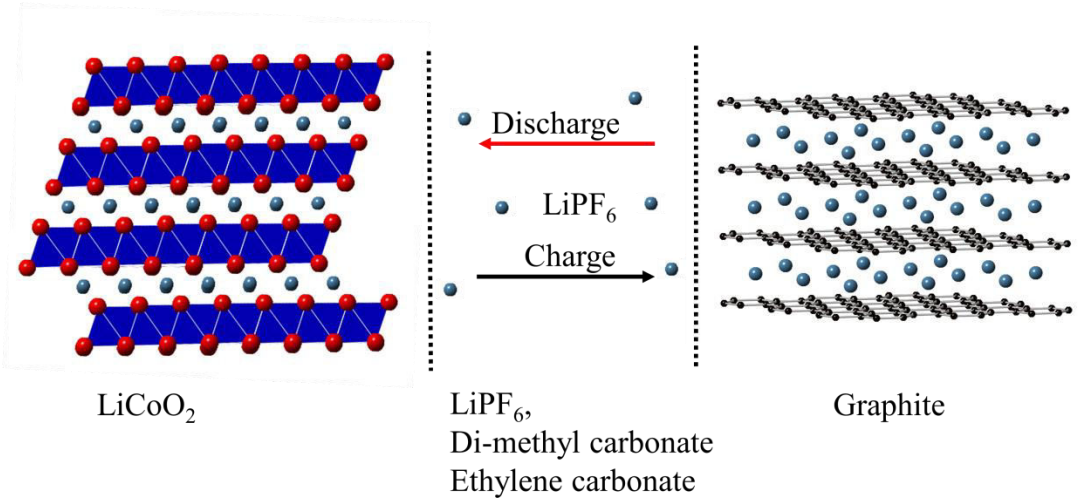

Figure 1.3 Typical secondary battery design

1.2.1 $(La/Li)_{1-x}TiO_3$ Perovskite Materials

The first synthesis of $Li_{0.5}La_{0.5}TiO_3$ was carried out by Brous et al.[13] replacing the divalent A cation in $ATiO_3$ with trivalent La and monovalent Li ions. Much work has since been carried out on the electrical properties of the $Li_{0.5-3x}La_{0.5+x}TiO_3$ type materials. Inaguma et al. [14] observed that with an increase in temperature, a large dielectric loss and dielectric relaxation occurred. This led to the idea that these materials may show high lithium ion mobility. The first conductivity studies were carried out by Belous et al., [15] who showed that the La ions

stabilize the perovskite structure, while the Li ions are responsible for carrying the charge resulting in high ionic conductivities.

This led to research into the structural features of the $Li_{3x}La_{(2/3)-x}\ Vac_{(1/3)-2x}TiO_3$ (~0.04 , $x \leq$ ~0.16) series [15-18] in order to help explain these high conductivities. The actual structure of this material is still debated, with simple cubic [14, 15, 17, 19, 20], hexagonal [21], tetragonal [15-18, 22, 23], and orthorhombic distorted cells all reported [14-18, 23]. The simple cubic cell is shown in figure 1.4. The key factor in determining the high conductivity is, however, both the Li content and the number of lattice vacancies present. The highest bulk lithium ion conductivity observed at room temperature 1×10^{-3} S cm^{-1} for $Li_{0.33}La_{0.557}TiO_3$ [24]. However, though bulk conductivities are high for this system, the total conductivity is reduced due to significant grain boundary resistive effects [25].

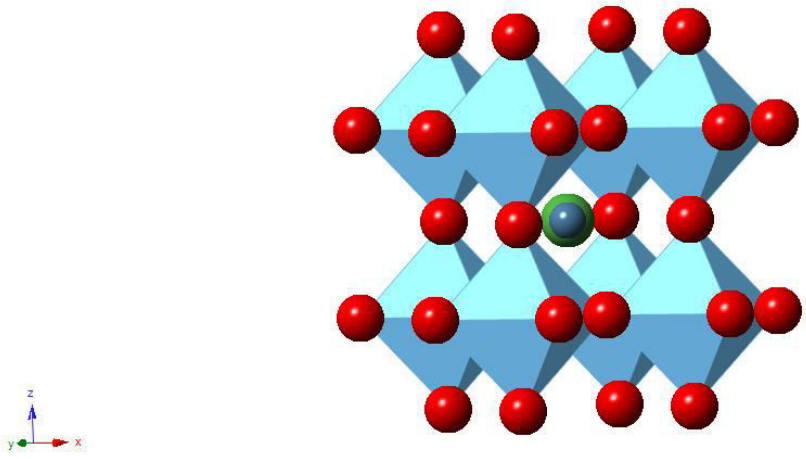

Figure 1.4 Cubic Perovskite structure of $La_{0.5}Li_{0.5}TiO_3$ (La = Green spheres, Li = Dark blue spheres, Ti = Light blue polyhedra, O = Red spheres)

1.2.2 Lithium-containing NASICON Materials

During the 1960's, layered β-($Na_2O \cdot 11Al_2O_3$) was investigated in detail, where high Na^+ ion diffusion between the alumina layers was observed [26, 27]. These materials are only two dimensional cation conductors, and so Hong and Goodenough et al. [28, 29] prepared an alternative framework structure capable of Na^+ diffusion through three dimensions. These materials were known as Na Super Ionic Conductors (NASICON) with the general formula $Na_{1+x}Zr_2P_{3-x}Si_xO_{12}$. Other phosphate compositions were subsequently reported to display the NASICON structure. The general formula of all these is $A_x(MM')_2P_3O_{12}$ where A can be alkali ions (Li^+ , Na^+ etc.), Alkaline earth ions (Mg^{2+}, Ca^{2+}, Sr^{2+}) or H^+, NH_4^+, Cu^{2+}, Cu^+, Ln^{3+}. The M and M' position can be divalent, trivalent, tetravalent, or pentavalent metal ions. In all these systems, silicon, arsenic or sulphur can also be substituted onto the phosphorus site.

While all possess the general NASICON structure, different compositions can have different cell symmetries, including rhombohedral [30-41], monoclinic [38-43] , orthorhombic [43-47], and triclinic [31, 35, 48-53]. In all cases the structure can be considered as a rigid three dimensional framework with PO_4/SiO_4 tetrahedra sharing corners with $M(M')O_6$ octahedra. This leaves channels in the framework where the conducting ions are positioned (A sites). There are two different positions for the "A" site: type 1 is along the c-axis in-between two $M(M')O_6$. The structure along the c-axis consists of ribbons of $O_3MO_3AO_3M'O_3$ in which the A cation has a distorted octahedral coordination. Type 2 A cations are located in-between the ribbons. The ribbons are connected along the a-axis by the PO_4 tetrahedra and these A sites are larger than the type 1[54, 55]. An example of NASICON structure with type 1 and 2 "A" positions is shown in figure 1.5. While the early work on these systems focused on Na ion conduction, they have since attracted interest in terms of Li ion conduction. The highest Li ion conductivity reported

was for $Li_{1+x}Ti_{2-x}M_x(PO_4)_3$ (M = Sc, Al x = 0.3) ($\sigma_{25\,^{\circ}C} = 7 \times 10^{-4}$ S cm^{-1}) [56]. However, these materials have proved difficult to sinter and reduction of Ti^{4+} also occurs when in contact with Li metal.

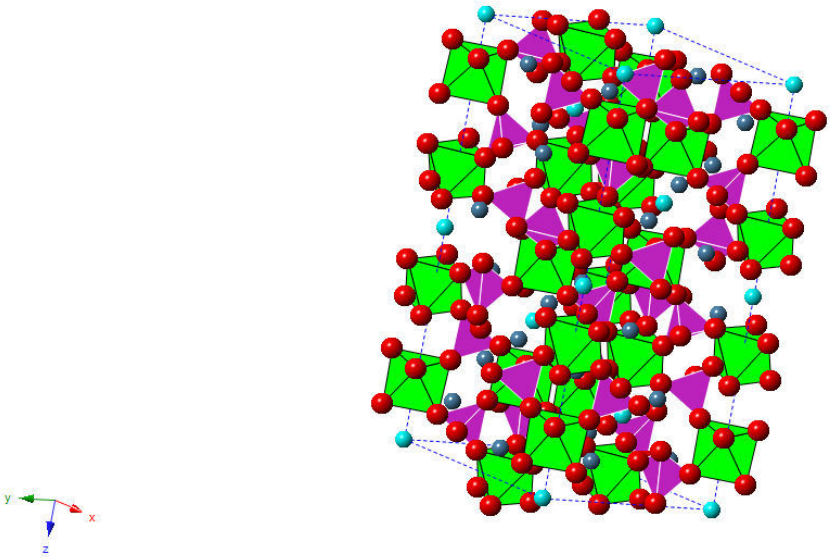

Figure 1.5 Typical NASICON framework (Li1 = Light blue spheres, Li2 = Dark blue spheres, Ti = Green polyhedra, P = purple polyhedra, O = Red spheres)

1.2.3 α-Li_4SiO_4 and LISICON

Stoichiometric Li_4SiO_4 is reported to have poor Li ion conductivity even at elevated temperatures ($\sigma_{300\,^{\circ}C} = 2 \times 10^{-5}$ S cm^{-1}). It is possible to improve the Li ion mobility by producing solid solution ranges of Li_4SiO_4 and Li_4GeO_4 or Li_4TiO_4 [57-59]. For example, for the composition $Li_4(Si_{0.6}Ti_{0.4})O_4$ the Li ion conductivity rises to 5×10^{-4} S cm^{-1} [57]. The ionic conductivity can be improved further by substitution of Si^{4+} with P^{5+} to form a solid solution series of $Li_{4-x}Si_{1-x}P_xO_4$,with the highest reported conductivity when x = 0.4 (Li ion conductivity reported to be $\sigma_{100\,^{\circ}C} = 1 \times 10^{-4}$ S cm^{-1}). The improved ionic conductivity from the parent material is due to the creation of Li ion vacancies in the structure [60-62]. Similar effects can be seen through As or V doping [63, 64]. Phase diagram studies have shown that the

Li_4SiO_4 rich end adopts a monoclinic-type Li_4SiO_4 structure, whereas in the intermediate range of *x*, the structure adopted is the γ-Li_4SiO_4 type, known as LISICON (Lithium Super Ionic Conductor). The first LISICON material reported was $Li_{14}Zn(GeO_4)_4$ which is a member of the $Li_{2+2x}Zn_{1-x}GeO_4$ ($-0.36 \leq x \geq 0.87$) system [65, 66]. The Li ion conductivity of $Li_{14}Zn(GeO_4)_4$ was reported to be $\sigma_{300\ ^\circ C} = 0.125$ S cm^{-1}. However, although the high temperature ionic conductivity is excellent, the low temperature conductivity is significantly reduced ($\sigma_{25\ ^\circ C} = \sim 10^{-7}$ S cm^{-1}). The large difference in conductivity with temperature is due to an interstital conduction mechanism, which is highly temperature dependent. H^+/Li^+ exchange has been reported in the systems by Sebastian et al. for systems where $x = 0.5, 0.75$, yet not observed in the parent material γ-Li_2ZnGeO_4 [67]. It has been proposed that the exchange occurs in the highly conducting phases and not the parent material due to the parent material's lack of interstitial Li^+, further supporting the theory of an interstitial-based conduction mechanism. LISICONs are considered to be ideal for high temperature battery applications due to their excellent Li ionic mobility at high temperatures and their poor Li ion mobility at low temperatures allowing for long term storage at room temperature (figure 1.6 shows the crystal structures of α-Li_4GeO_4 and γ-Li_4GeO_4).

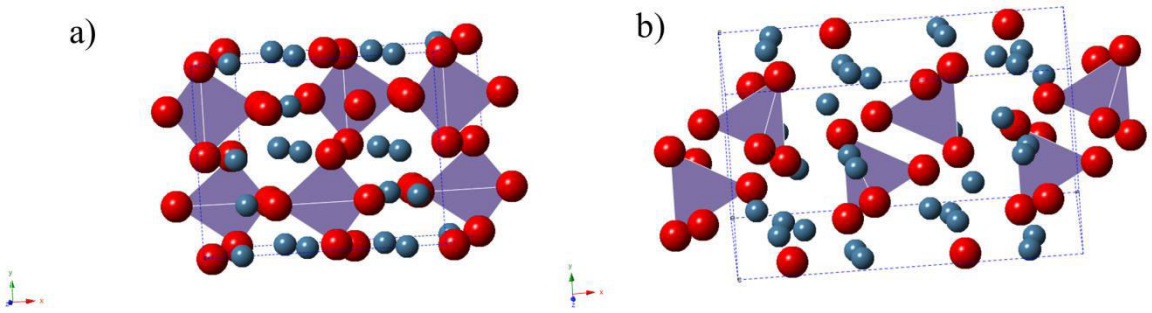

Figure 1.6 Crystal structure of a) α-Li_4GeO_4 b) γ-Li_4GeO_4 (Li = Blue spheres, Ge = Purple polyhedra, O = Red spheres)

1.2.4 Other lithium ion conducting solids

Na-β-alumina was one of the first reported alkali ionic conductors. It has a 2D layered structure. A Li derivative $Li_2O.11Al_2O_3$ with extremely high room temperature Li ion conductivity (~10^{-3} S cm^{-1}) has also been reported. However, this material is highly hydroscopic and hard to synthesise anhydrous[68].

Another reported Li ion conductor is the ramsdellite type material, $Li_2MgSn_3O_8$, which has a low conductivity at high temperature $\sigma_{300\ ^\circ C} = 1.2 \times 10^{-8}$ S cm^{-1} [69]. However, this can be improved ($\sigma_{300\ ^\circ C} = 5 \times 10^{-4}$ S cm^{-1}) by replacing Mg^{2+} with two Li^+ cations leading to the incorporation of Li^+ ions into interstitial sites[70]. However, this improvement in conductivity is still insufficient for practical applications.

West et al.[71] have reported a solid solution series of vanadomolydbates $LiMg_3VMo_2O_{12}$ based on previous reported orthorhombic double molybdate $Li_2M_2(MoO_4)_3$ (M = M^{2+}). Structurally this comprises two unique Li/Mg octahedra and Li/Mg trigonal prisms and two unique Mo/V tetrahedra. A phase change at high temperature was observed, which results in good Li ionic mobility of $\sigma_{500\text{-}600\ ^\circ C} = 1 \times 10^{-3} - 4 \times 10^{-2}$ S cm^{-1} [71].

Another system $Li_2NaTa_7O_{12}$, was first reported by Grims et al. and exhibits a layered framework of Ta_7O_{19} which is made up of TaO_6 octahedra and Ta_7O_7 pentagonal bipyramids, with Na located in the pentagonal tunnel in the *c* direction. The ionic conductivity was, however, low even at high temperature ($\sigma_{300\ ^\circ C} = 2 \times 10^{-7}$ S cm^{-1}) [72].

1.2.5 Garnet Materials

Garnet materials were first proposed as potential Li ion conducting solid electrolytes in 2003 by Thangadurai et al [1], who prepared the garnets $Li_5La_3M_2O_{12}$ (M= Ta, Nb), showing lithium ion conductivity on a par with other highly Li^+ ion conducting materials. An initial reported

advantage of the garnets was that they showed chemical stability when exposed to air, moisture and lithium electrode [73]. However, recent studies have contradicted this assertion, suggesting Li^+/H^+ exchange can occur in air [2, 3, 74-80] or when submerged in an organic acid or water[79, 81-84].

The ideal garnet structure has a formula of $A_3B_2C_3O_{12}$ with space group $Ia\bar{3}d$. Each of the A, B, C cations show distinct coordination numbers towards oxygen: A is eight coordinate, B is octahedral, and C is tetrahedral. In terms of the Li ion conducting garnets, excess Li is required. For these systems, the conventional 8 coordinate (A) and 6 coordinate (B) sites are fully occupied, while partial occupancy of the tetrahedral (C) sites is observed, with additional Li in interstitial sites not normally occupied in the garnet structure[1, 5, 6, 8, 73, 85-101].

As mentioned, in the ideal garnet structure the C site has a total occupancy of 3. O'Callaghan et al. prepared a series of lithium containing garnets $Ln_3Te_2Li_3O_{12}$ (Ln = Y, Pr, Nd, Sm–Lu) with this ideal stoichiometry. They reported the Li ionic conductivity to be very low even at elevated temperatures (e.g. $\sigma_{600\ ^\circ C}$ = ~10^{-5} S cm^{-1}). As the Li is fully ordered on the ideal tetrahedral site it was suggested that the two octahedral interstitial sites are key to the conduction mechanism[102]. Therefore, in order to improve the ionic conductivity it is essential to increase the Li content so that Li will occupy these interstitial octahedral sites.

Following the initial reports on the synthesis of such garnets containing higher Li contents, the exact crystal structure and the Li distribution had been highly debated. Mazza [103] reported in 1988 that the crystal structure of $La_3M_2Li_5O_{12}$ (Nb, Ta) was similar to that of the ideal garnet structure, whereas from single crystal X-ray diffraction studies Hyooma and Hayashi[104] suggested an alternative space group $I2_13$. It was not until Cussen [73] used powder neutron diffraction that the Li distribution was elucidated (figure 1.7a) . He showed that the space group was as Mazza suggested ($Ia\bar{3}d$) and that the Li occupies both the ideal

tetrahedral and the two distorted octahedra, which allows an increase in the Li content above 3. This excess Li improves the Li ion conductivity of $La_3Ta_2Li_5O_{12}$ with reports of $\sigma_{bulk(25\ ^\circ C)} = 3.9 \times 10^{-4}$ S cm^{-1} [105]. It has been shown that it is possible to replace Nb and Ta, in $La_3M_2Li_5O_{12}$ (M = Nb, Ta) with Bi, Sb or In [85, 87, 97, 106, 107] and replace La with Pr, Nd, Ba, or K [94, 97, 106].

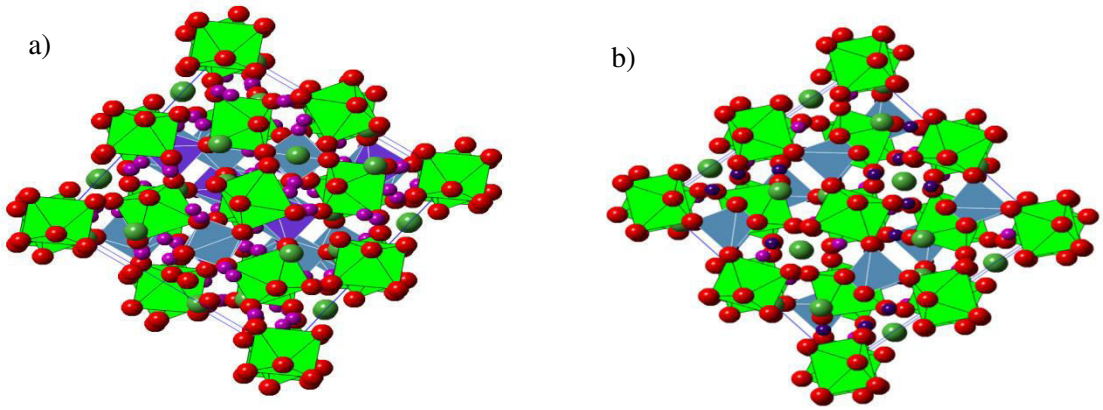

Figure 1.7 a) Crystal structure of cubic Li containing garnet b) tetragonal Li containing garnet (Green spheres La, green octahedra Zr, Blue tetrahedra Li1, light purple spheres Li2 distorted octahedra, dark purple spheres Li3 distorted octahedra, purple tetrahedra Ga)

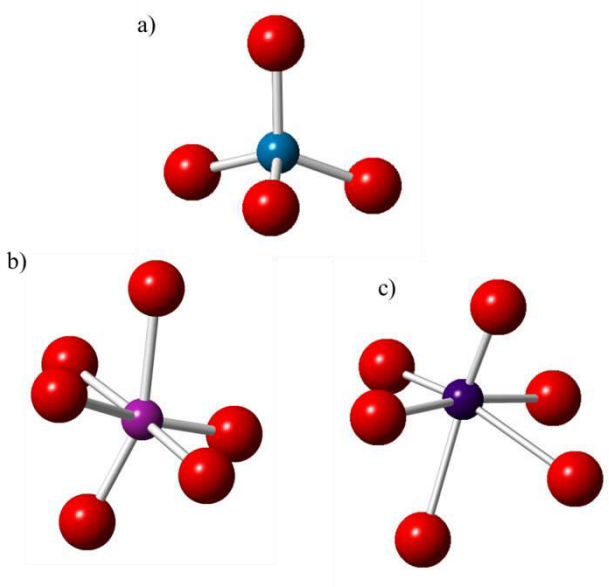

Figure 1.8 Three different types of lithium coordination a) Li1 b) Li2 c) Li3 in $La_3Sn_2Li_7O_{12}$

In addition it has been shown that it is possible to increase the Li content further by replacing the trivalent La^{3+} with divalent cations resulting in $La_{3-x}A_{1-x}M_2Li_{5+x}O_{12}$ (A = Mg, Ca, Sr, Ba, and M = Nb, Ta) with compositions up to $x = 1.6$ reported[96, 99, 108-111]. As noted above, due to the low X-ray scattering factor of Li it has been difficult to determine the Li distribution over the different sites in these systems and this has highlighted the importance of neutron diffraction studies in these materials. It was found that the substitution of La with the divalent ions and tri/tetravalent ions for pentavalent Nb/Ta ions would cause increased occupancy of the distorted octahedral Li2 and Li3 sites and decrease in occupancy of the tetrahedral site, thus decreasing the number of vacancies in the octahedral sites and increasing them in the tetrahedral sites compared to the garnets containing 5 Li atoms per formula unit. Clustering of the Li ions can also occur in these materials, so as to avoid short Li–Li bond distances. Typical Li ion conductivity values of $\sigma_{25\ ^\circ C} = \sim 10^{-5}$ S cm^{-1} [112] have been reported for garnets containing 6 Li atoms per formula unit.

By co-doping with Y on the B site and Li it is possible to increase the Li content to 6.5 Li per formula unit which gives one of the best room temperature Li ion conductivities in the garnet type material of 2.7×10^{-4} S cm^{-1} [89]. It has also been reported that increasing the ionic radius (Ca to Ba) of the dopant on the A site results in improved lithium ion mobility attributed to a broadening of the bottlenecks in the conduction pathway[113].

Murugan et al.[111] showed it is possible to accommodate up to 7 Li by substituting Nb/Ta for Zr to give $La_3Zr_2Li_7O_{12}$. This compound has caused a large degree of interest and particular controversy. Initially, this was reported to have cubic symmetry and display very high Li ion conductivities ($\sigma_{25\ ^\circ C} = 3.1 \times 10^{-4}$ S cm^{-1})[114]. However, subsequently other groups reported tetragonal symmetry (figure 1.7b) with low conductivity ($\sigma_{27\ ^\circ C} = 1.63 \times 10^{-6}$ S cm^{-1})[115]. This confusion of the true symmetry of Li-stuffed garnets containing 7 Li atoms per formula unit further highlights the importance of understanding the lithium sublattice through neutron

diffraction studies. Such studies have shown that the 3 different Li sites can be fully occupied in the garnet structures. Slater et al.[116] showed that it is possible to replace Zr with Sn to form a tetragonal $La_3Sn_2Li_7O_{12}$. Through neutron diffraction studies they showed that the tetragonal distortion is caused by ordering of the Li sublattice to avoid short Li–Li bond distances, which is achieved by having one Li in the ideal garnet tetrahedral coordination, four Li ions in the Li2 site and two Li ions in the Li3 sites[116]. In theory full occupancy of these crystallographic sites would add up to a possible 9 Li per formula, however, in reality only up to 7 sites can be occupied, as further occupation above this level would lead to unfavourably short Li–Li interactions. Hf substitution for Zr also causes the formation of a similar tetragonal garnet.

As mentioned earlier, work on $La_3Zr_2Li_7O_{12}$ has led to reports of cubic phases with high Li ion conductivity [111, 117-121] and tetragonal phases with low Li ion conductivity[2, 75, 76, 115, 122, 123]. The cubic samples are often heated to high temperatures (higher than 1000°C) and for long heating time (over 12 hours). This can potentially give rise to Li volatility or cause reactions between the sample and the crucible causing Al incorporation. Both of these can cause Li to leave the structure causing disorder in the Li sublattice resulting in a cubic unit cell and hence the high Li ion conductivity. Following the reports of Al incorporation from the crucible during the synthesis, research into determining the dopant site and also what other dopants could be doped to improve the conductivity has been performed. There have been reports (including examples in this thesis) of a number of different trivalent or tetravalent cation dopants that are able to be introduced onto this site including Ga, Ge, In and Si. Through neutron diffraction, solid state NMR and computational calculations it has been confirmed that the preferred dopant site is the ideal tetrahedral (Li1) site[75, 124-129]. It has also been reported that it is possible to lower the Li content in $La_3Zr_2Li_7O_{12}$ *via* doping on the octahedral B site with Sb, W, Nb, Ta, or Cr [122, 123, 130-135]. All doping strategies were shown to

improve the Li ion conductivity *via* the creation of disorder in the Li sublattice. It is also possible to dope or fully change the cation present on the A site from La to Nd, Sr, or Ca[3, 135-137]. This thesis shows that it is possible to prepare a range of other phases with high Li contents and hence tetragonal symmetry (see chapters 3, 4 and 7).

In order to understand the conduction mechanism of the garnets, a number of diffraction techniques have been used. Firstly O'Callaghan and Cussen used powder neutron diffraction and NMR studies on $La_{3-x}Ba_xTa_2Li_{5+x}O_{12}$ in order to understand the Li occupancy of the tetrahedral and octahedral sites. They found a high displacement parameter in the tetrahedral site in the $x = 1$ system. Through their NMR studies they showed that there was no change in the distribution of the Li when $x = 1$. This showed that the displacement of the Li in the tetrahedral and octahedral sites was in fact due to static disorder. As 1 ideal tetrahedral Li is face sharing with four octahedral Li, and in turn the octahedra face share with two tetrahedra, any displacement of the Li sites away from neighbouring Li would result in it being shifted towards other neighbouring Li sites. However, if one of the neighbouring sites is vacant then the bond distance of the Li of neighbouring octahedra and tetrahedra would increase. This therefore means that only two out of three of neighbouring tetrahedra-octahedra-tetrahedra can be occupied. The destabilizing effect on the Li within this octahedral site is key to the high Li ion mobility in these systems[92]. Further proof on the importance of the octahedral site was highlighted again by O'Callaghan et al. Using ^{6}Li NMR they showed no Li1 to Li2 hopping[138] but showed hopping from one edge sharing octahedron to another which causes the high Li ion conductivity. Furthermore Ramakumar et al. [139] showed through, investigating the effects of Li concentration, that it essential to have Li distributed over both tetrahedral and octahedral sites. Low Li concentrations (3 Li per formula unit) resulted in low lithium ion conductivity and high activation energies, due to lithium being solely located on the tetrahedral site, and for conduction to occur the mobile ion needed a vacant octahedral site to

"jump" to. Baral et al.[140] have claimed that the tetrahedral site is immobile in the conduction process and that the octahedral Li atoms move around the tetrahedral lithium.

In order to understand the conduction process and to complement structural studies a number of computational modelling calculations have been investigated. Wang et al. [141] have shown through static lattice simulations that with respect to the local structure of the lithium atoms, ordering increases with increasing lithium content and that overall a lower lithium occupancy in the tetrahedral site is favoured compared than that suggested through the averaged Rietveld refinements. However, other modelling studies suggest the Li ion is unstable in the ideal tetrahedral site and this is key in triggering the lithium reconfiguration[142, 143]. Still there is no definitive answer to the true conduction mechanism with a number of reports that both mechanisms are feasible[100]. We have also used complementary computational modelling with structural refinements to determine the preferred dopant site of trivalent cations [3] (discussed in chapters 4). Density functional theory calculations have been used to investigate the chemical stability of tetragonal garnets against CO_2 and H_2O[144] which showed that the chemical stability of the garnets are similar to both CO_2 and H_2O and the partial pressure is key to determining the stability in these environments.

In order to be considered as an electrolyte in Li ion batteries a material must show a good chemical stability and chemical compatibility. Gao et al. showed that a reaction occurred on heating $La_3Bi_2Li_5O_{12}$ with $LiCoO_2$ to 600 °C, showing that these materials are not compatible at this temperature[85]. However, $La_2BaTa_2Li_6O_{12}$ has been reported to be compatible with $LiCoO_2$ up to 400 °C. In other compatibility studies, $La_3Zr_2Li_7O_{12}$ has been shown to be chemically stable to molten Li[111] yet when compatibility studies were performed between thin films of $LiCoO_2$ and $La_3Zr_2Li_7O_{12}$, an intermediate reaction layer which reduced the electrochemical performance was observed[145]. Fully chargeable and dischargeable solid state batteries of Li/$La_3Zr_2Li_7O_{12}$/Li and $LiCoO_2$/ $La_3Zr_2Li_7O_{12}$/Li have been reported. The latter,

however, showed low cycling capacity and high interfacial resistance[146]. More recently Ca and Nb doped $La_3Zr_2Li_7O_{12}$ has been reported to work well as an electrolyte in an all solid state battery with $LiCoO_2$ and Li metal[147]. Narayanan et al. reported a good lithium ion conductivity with good chemical stability towards high voltage spinel cathodes[89] for $La_3Nb_{1.25}Y_{0.75}Li_{6.5}O_{12}$.

Moreover, while it was initially thought that these Li ion conducting garnets were stable when exposed to air, recent reports have shown that this is not the case and that H^+/Li^+ exchange can occur in air[3, 74-76, 148, 149] or *via* being submerged in organic acids and aqueous solutions [2, 74, 79, 81-84, 150-152]. The work in this thesis showed for the first time (see chapter 3) that H^+/Li^+ occurs in air and that the exchange improved the grain boundary resistance which lowered the overall total Li ion conductivity in Ga doped $La_3Zr_2Li_7O_{12}$ [75]. We have also shown that the changes in conductivity on exposure to moisture is due to bulk effects and not due to surface conduction along the lateral edges of the prepared pellet[3] (chapter 4). It has also been reported that the exchange can be reduced by sintering the sample in dry O_2[148]. In this thesis we have also determined the location of the exchanged H^+ *via* powder neutron diffraction studies and shown that it was located within the Li octahedra directed toward the Li at the centre[82] (chapter 5). Exposure to air for extended periods of time will cause decomposition of the material[149]. It has also been reported that exposure to CO_2 can induce a phase transition from tetragonal to cubic showing that these materials are extremely sensitive to different atmospheres[150, 153, 154].

As well as research into improving the lithium ion conductivity through doping studies, many researchers have attempted alternative synthetic and sintering approaches. Al doped $La_3Zr_2Li_7O_{12}$ was sintered *via* field-assisted sintering technology (FAST) showing extremely high pellet density (99.8%) with a short sintering time (10 minutes). This method led to an increase in the Li ion conductivity compared to the conventional sintering method[155] or

nebulized spray pyrolysis[156] . Sintering aids have been used to improve the conventional sintering method, one example being the addition of a small amount of Li_3BO_3 and Al_2O_3, which was reported to lower the sintering temperature[147]. Simply changing the lithium source from Li_2CO_3 to $LiOH.H_2O$ result has been reported in more spherical and narrower particles, which in turn resulted in an improved lithium ionic conductivity[157]. Other preparation methods for garnet type materials have seen aerosol or chemical vapour deposition which gave a highly dense film without the need for annealing[158, 159].

1.3 Hydrogen Storage Materials

With hydrogen having a gravimetric energy density of 120 MJ kg^{-1} and liquid hydrogen having a volumetric density of 8.4 MJ L^{-1} it provides an excellent alternative to fossil fuels. A problem with hydrogen storage is that liquid hydrogen requires a large amount of energy to cool to cryogenic temperatures and hydrogen gas requires large amounts of energy to achieve high pressures; both methods also add weight to the storage system. The U.S Department of Energy set a list of criteria that a hydrogen storage material must meet if it is to be used in mobile applications[160];

1. A high gravimetric density (7.5 wt.%)
2. Hydrogen delivery temperature (-40 – 85 °C) and pressure (5 bar)
3. Fast kinetics
4. Reversible and capable of 1500 de/rehydrogenation cycles
5. Safe and non-toxic
6. Cost effective

This has led to research into new materials for hydrogen storage including metal hydrides.

1.3.1 Lithium Nitride as a hydrogen storage material

In 1930, the initial characterisation of α-Li_3N structure began. Zintl and Brauer[161] used single crystal diffraction data to determine its structure. The structure was then re-determined by Rabenau and Schultz [162]. The α-Li_3N structure is unique; it is made of hexagonal 'graphite-like' layers of hexagonal planar Li with a N at the centre of each hexagon. The hexagons of Li_6N are capped both above and below in the *ab* plane by a Li atom, thus connecting the layers along the *c*-axis (3 dimensional). This gives the N atom a total coordination of 8 in hexagonal bipyramidal geometry. The Li located within the hexagon have trigonal planar coordination geometry and the Li atoms located above the hexagon are linearly coordinated to the N atoms, as shown in figure 1.9.

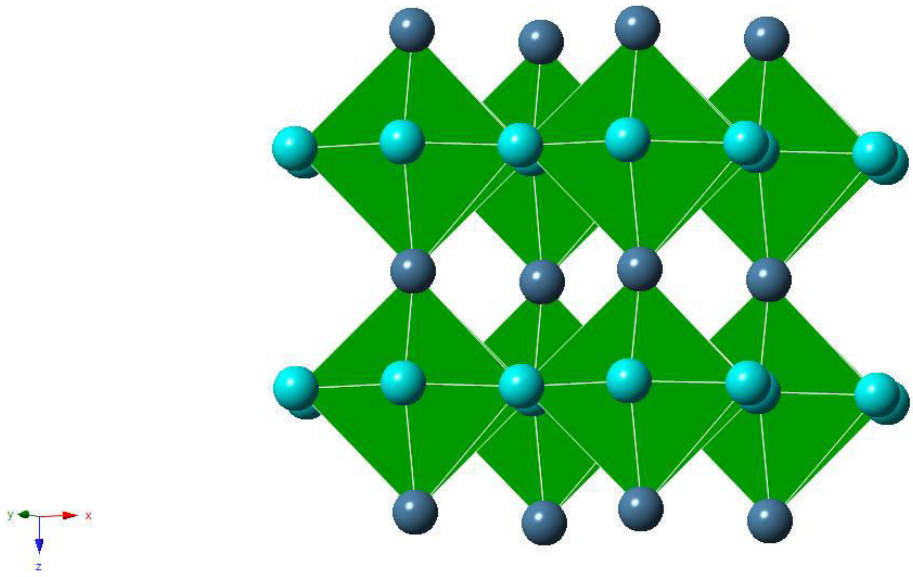

Figure 1.9 Crystal structure of α-Li_3N (Li1 = Light blue spheres, Li2 = Dark blue spheres, N = Green polyhedra)

With the improvements in state of the art techniques it was found that there are more phases of Li_3N under increased pressure. β-Li_3N was first discovered through elevated pressure ^{7}Li-NMR studies of Li_3N[163]. The phase transition occurs at 4.2 kbar at 300 K. Through X-ray

diffraction studies, the β phase retains similar structural features to the α phase. In the β phase, however, the Li-N layers change from a composition of Li_2N to LiN due to the N being shifted from a simple hexagonal packing to hexagonal close packing. The N coordination geometry is a trigonal prism capped on all five faces. β-Li_3N is isostructural with Li_3P (Na_3As type) shown in figure 1.10. The γ-Li_3N phase was first observed at pressures above 10 GPa [164] and is assumed to be isostructural with Li_3Bi. Phase transitions between Na_3As and Li_3Bi structure types have also been observed[165, 166].

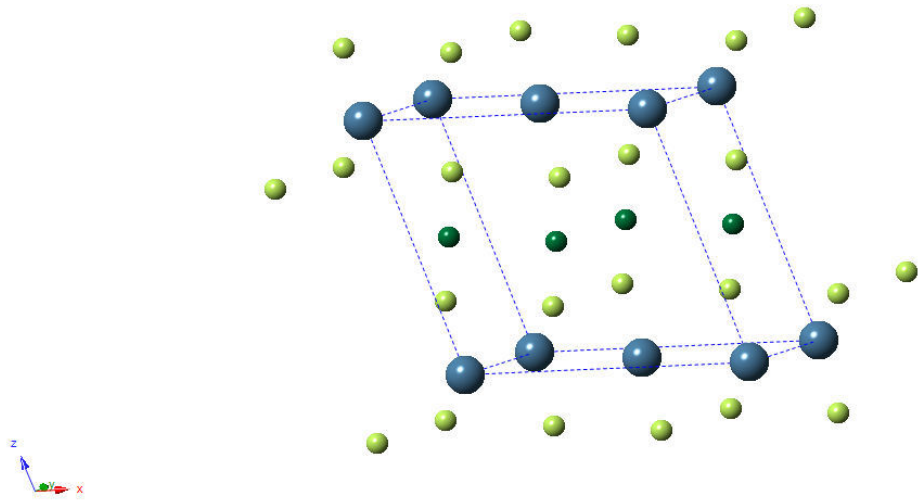

Figure 1.10 Crystal structure of β-Li_3N (Li1 = Dark blue spheres, N1 = Dark green spheres, N2 = Light green spheres)

Li_3N has been reported as one of the most highly Li ion conducting materials with ionic conductivities $\sigma_{\alpha(25\ ^\circ C)} = 5.8 \times 10^{-4}$ S cm^{-1} and $\sigma_{\beta(25\ ^\circ C)} = 2.1 \times 10^{-4}$ S cm^{-1}. In the α phase the conduction mechanism is site-to-site hopping within Li_2N layers, and the Li atoms that cap the hexagonal layers are immobile, whereas the β phase conducts *via* diffusion within the pure Li plane [167].

Li_3N was first considered as a potential dehydrogenation parent material in 1911[168]. Chen et al. then exploited the potential of the two step equation given in equation 1. 2.

$$Li_3N + 2H_2 \leftrightarrow Li_2NH + H_2 + LiH \leftrightarrow LiNH_2 + 2LiH \quad \textbf{(1.2)}$$

The majority of the research on this particular system is based on the second half of the reaction which will be discussed in section 1.3.2., as the reverse step of the first part of the reaction is deemed unfavourable due to high reaction enthalpy causing high desorption temperature and slow reaction kinetics[4, 169-172]. Powder neutron diffraction studies have been performed to understand the hydrogenation/deuteration of Li_3N. It was found that the deuteration/hydrogenation occurs *via* a 'quasi-imide' phase $Li_{2+y}NX$ (X = H, D) and that the absorption is dominated by changes in the stoichiometry of this phase [169, 173]. However, it was also found that increased pressure (5 bars) would result in non-stoichiometric products not being observed [174]. Upon balling milling, α-Li_3N will undergo the aforementioned phase transition to β-Li_3N. It was reported that commercially bought Li_3N exhibits improved hydrogen uptake compared to milled or pre-heated Li_3N. It was determined that the presence of β-Li_3N is detrimental to the reaction mechanism [175]. However, it has been reported that the use of carbon in combination with Li_3N improved the hydrogen storage properties[176, 177].

1.3.2 Amides and Imides as Hydrogen Storage Materials

Amides and imides are attractive materials for hydrogen storage, as they have a theoretically high capacity to store hydrogen (6.5 wt.%) and low operating temperatures. However, they currently have poor absorption kinetics and the release of trace amounts of ammonia which has limited their practical use.

$LiNH_2$ was first synthesised in 1894 by Titherley [178]. Further work was carried out [179] to find a more efficient way to prepare the materials; this was achieved by heating Li_3N under hydrogen at 220–250°C. Chen et al. [170] (as mentioned in section 1.3.2) proposed the reaction

pathway shown in equation 1.2. Due to its more favourable reaction kinetics the second half of the reaction has seen worldwide research.

Chen et al.[170, 171] were the first to suggest that $LiNH_2$ would react with LiH to release hydrogen, while Hu and Ruckenstien [180] showed that $LiNH_2$ undergoes decomposition to Li_2NH and NH_3. This is then followed by LiH reacting with NH_3 to give H_2 and $LiNH_2$. The cycle continues until all $LiNH_2$ and LiH has reacted. The reactions are given in equation 1.3 and equation 1.4. Research into confirming this reaction mechanism has been reported[181, 182]

$$2LiNH_2 \rightarrow Li_2NH + NH_3 \quad \textbf{(1.3)}$$

$$NH_3 + LiH \rightarrow LiNH_2 + H_2 \quad \textbf{(1.4)}$$

Li–Mg–N–H systems were first suggested by Zhitao[183] in 2004. These systems are based upon **e**quation 1.5. In this equation four H atoms (5.87 wt.%) can be absorbed by one $Li_2Mg(NH)_2$ formula unit. These systems showed improved hydrogen absorption/desorption conditions[184]. The lower hydrogen desorption temperature occurs due to $Mg(NH_2)_2$ releasing NH_3 at lower temperatures than lithium imide.

$$Li_2Mg(NH)_2 + 2H_2 \leftrightarrow Mg(NH_2)_2 + 2LiH \quad \textbf{(1.5)}$$

It has been reported for both $LiNH_2$[185] studies and $Mg(NH_2)_2$[186] that improvements have been observed on K doping. It is thought that the thermodynamically favourable conversion of LiH to KH occurs, which may act as a catalyst to the release of hydrogen in these systems. Other doping studies have included the incorporation of Al into the $LiNH_2$, which again had positive effects on the cycling of hydrogen absorption/desorption[187, 188].

Other reports have suggested[172, 189-191] that including a small amount of $TiCl_3$ into the reaction mixture of equation 1.2 improves the absorption/desorption kinetics by lowering the

hydrogen desorption temperature to between 150 to 250°C. However, the incorporation of Ti metal is not desirable as it increases cost.

David et al. [192] have reported the importance of Li ion mobility in equation 1.2. They suggested the importance of short lived Frenkel defects in the octahedral site as a possible mechanism for the decomposition of $LiNH_2$ to Li_2NH.

In 1983 Gotoh [193] patented a series of lithium imide–halides that showed high Li ion conductivity and also low activation energy for conductivity . Matsuo et al.[194] then reported a new system $Li_3(NH_2)_2I$ which showed very high room temperature lithium ion conductivity of 1.7×10^{-5} S cm^{-1} . The reported conductivity is 4 orders greater than that of $LiNH_2$ at the same temperature.

Anderson et al. [4] showed that by incorporating halides into lithium amide systems, hydrogen was released at a lower temperature and that the release of ammonia was not detected as a side product. Also the dehydrogenation products of these materials showed improved hydrogen absorption properties by being hydrogenated faster than Li imide. They proposed from this work that halides improve Li ion conductivity which aids in both the dehydrogenation and rehydrogenation stages. Borschulte et al. also emphasized the importance of ion mobility in borohydrides and amides[195]. More recently Davies et al.[196-198] reported that it is possible to reduce the chloride and bromide content in halide-containing lithium amide chloride and magnesium-doped lithium amide chloride whilst still maintaining the improved hydrogen storage properties. Li et al. reported high ionic conductivity in Li-Mg-H-Br systems with improved hydrogen desorption at ~120°C[199]. Cao et al. recently reported that the bromide amide $Li_2Br(NH_2)$ desorption process is NH_3 mediated rather than affected ion mobility due to $LiNH_2$ being confined in Br cages[200].

1.3.3 Lithium Halide Nitrides

Lithium nitride halides $Li_{3-2x}N_{1-x}Hal_x$ (*Hal* = Cl, Br, I) were synthesised in 1964 by Sattlegger [201]. However, full structural characterisation was not carried out till over 30 years later[202-209].

For the chloride-containing phases two structural types have been reported. An antifluorite-type phase has been reported with a number of different stoichiometries (Li_5NCl_2 and $Li_9N_2Cl_3$). Powder neutron diffraction studies by Marx [207] showed that the anions form a cubic close packed array with a ratio of 1:2 of N to Cl, and Li occupying 5/6 of the tetrahedral holes. Marx also reported that this phase will order under long annealing of the antifluorite structure[207]. The ordered structure is based upon ordered N and Cl atoms in a 1:2 ratio in a close packing arrangement. The anions stack along the hexagonal axis in an ABABCBCACA sequence. Here the N layers are sandwiched by two chloride layers forming a cubic close packed arrangement. A hexagonal close packed arrangement is formed by the Cl layers, where they have a Cl and a N layer either side. The anion arrangement is distorted from the ideal close packing, and the structure contains three different Li sites. The first site (Li1) is located in triangular voids of the N layers and is displaced towards a neighbouring Cl, this site contains 2/5 of the Li in the structure. A further 2/5 of the Li are located in tetrahedral holes of NCl_3 (Li2) and the remaining 1/5 (Li3) are in octahedral holes formed from Cl layers. The crystal structures of ordered and disordered Li_5NCl_2 are shown in figure 1.11. The Li ion conductivity of the antifluorite-type phase was reported to be the highest of the lithium halide nitrides $\sigma_{bulk\ (105\ °C)} = 5 \times 10^{-5}$ S cm^{-1} [210].

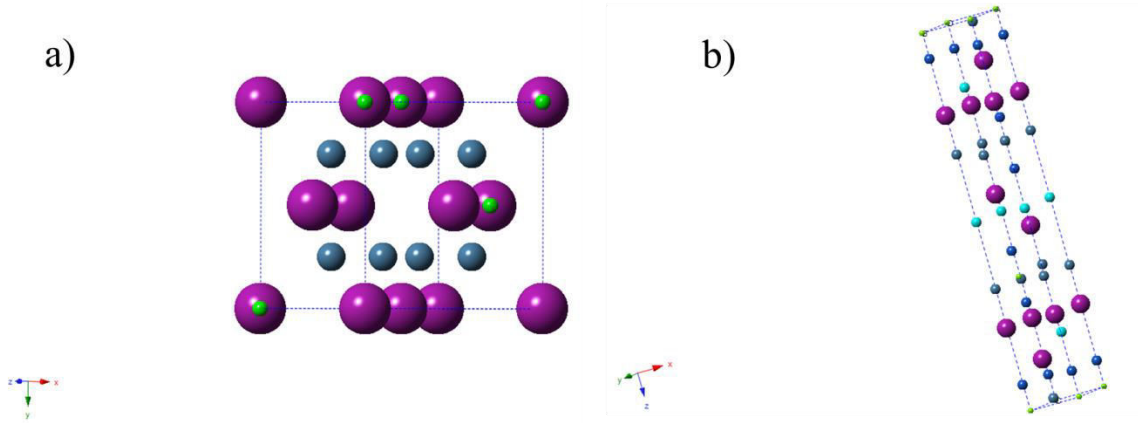

Figure 1.11 a) Disordered antifluorite structure of Li_5NCl_2 b) ordered Li_5NCl_2 (Li1 = Dark blue spheres, Li2 = Dark blue spheres, Li3 = Royal blue spheres, N = Green spheres, Cl = Purple spheres)

Marx also reported a new rhombohedral Li_4NCl phase [202]. Here the anions form a cubic close packed arrangement of ABCABCA. The N and two Li sites form a hexagonal bipyramidal coordination similar to that of Li_3N. The Li atoms within the nitrogen layer are shifted along the *c*-axis towards the Cl atoms (figure 1.12).

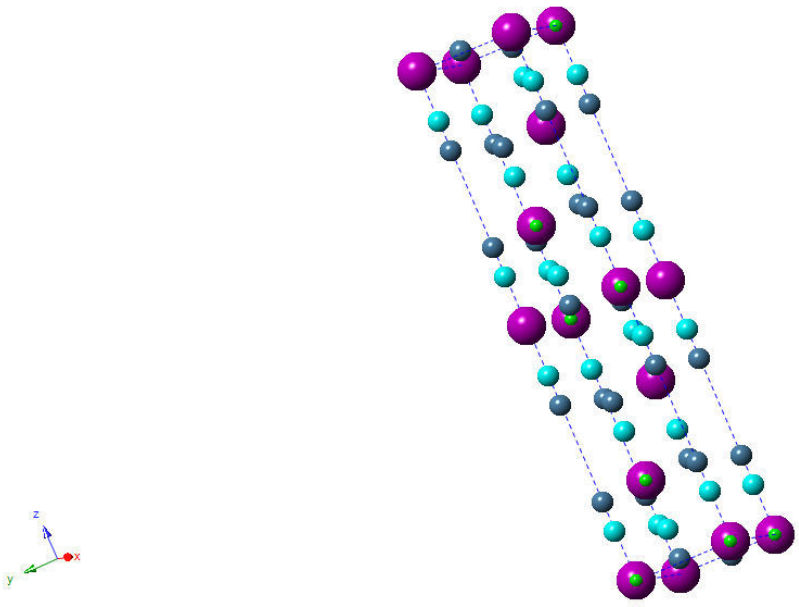

Figure 1.12 Crystal structure of Li_4NCl (Li1 = Dark blue spheres, Li2 = Dark blue spheres, N = Green spheres, Cl = Purple spheres)

For the bromine-containing lithium halide nitrides, a total of 3 different phases have been reported. First of these was Li_6NBr_3 by Sattlegger and Hahn [201]. They reported a cubic *fcc* structure with the Li atoms being ordered in an octahedron around a central N atom. As for the Cl system, Marx used both room temperature, elevated and cryogenic neutron diffraction studies to determine the crystal structures and show temperature dependent phase transitions. It was shown that Li_6NBr_3 has a complex temperature behaviour showing 4 different phases [203, 206] (figure 1.13).

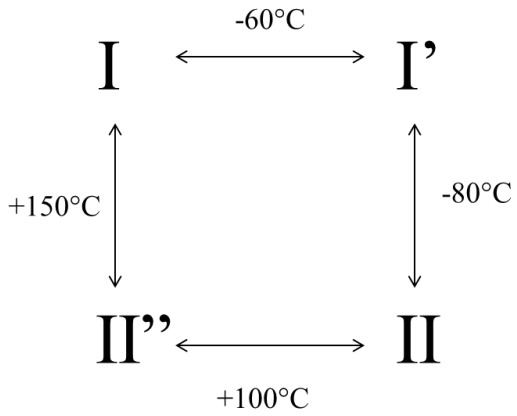

Figure 1.13 Phase transitions due to temperature of Li_6NBr_3

Marx investigated two possible Li distributions for the room temperature phase (Li_6NBr_3-I). The first model contained disordered Li atoms over distorted tetrahedral sites and the second model had the Li disordered around a nitrogen octahedron. However, they were unable to distinguish fully between the two models[206].

The phase transitions can be described as Li_6NBr_3-I being the high temperature thermodynamically stable phase, Li_6NBr_3-II being the low temperature thermodynamically stable phase with I′ and II″ being metastable variants of I and II.

Li_6NBr_3-I′ is an anti-form of the cryolite structure (Na_3AlF_6). The Li_6NBr_3-I to Li_6NBr_3-I' transition may be characterised by the Li atom repelling the Br coordination sphere and the

ordering of the Li sublattice to minimise short Li–Li bond distances. The transition from Li_6NBr_3-I′ to Li_6NBr_3-II has yet to be characterised, but it has been proposed that it occurs in a similar fashion to that of α-AgI to γ-AgI [211, 212], which involves anion rearrangement. Li_6NBr_3-II has the $TiFe_3$ structure with only a slight distortion of the cubic close packed N and Br, with Li fully ordered in ¾ of the tetrahedral voids and the unit cell doubled in each direction. The metastable Li_6NBr_3-II′ also has a $TiFe_3$ arrangement of N and Br, however, here the Li is disordered over the tetrahedral voids. The N-Br arrangement in the high temperature phase can be derived from the metastable Li_6NBr_3-II′ by expanding along the *a*-axis whilst contracting along the *c*-axis. The N and Br will now form an ordered body-centred packing instead of the cubic close packing. Figure 1.14 shows all 4 structures of Li_6NBr_3. The lithium ionic conductivity of Li_6NBr_3-I was reported by Hartwig to be $\sigma_{bulk(150\ °C)} = 3.5 \times 10^{-6}$ S cm^{-1} [213].

Marx reported a further two lithium bromide nitrides, $Li_{10}N_3Br$ and Li_5NBr_2. The former has a similar structure to that of Li_3N consisting of pentagonal bipyramidal Li_7N units that share edges and vertices to form a three dimensional $Li_{10}N$. Br is located in trigonal prismatic holes formed from the Li [205]. The latter comprises a Li-N sublattice of linear vertex-sharing chains of octahedra of Li_6N along the *c*-axis, which are separated by Br chains. The anion arrangement can be described as an ordered cubic close packing [209].

Two phases have been reported for the lithium iodide nitrides, Li_6NI_3 and Li_7N_2I. The former is isostructural with Li_6NBr_3 [208], whereas Li_7N_2I can be described as framework of $Li_{13}N_4^+$, which is constructed of monocapped octahedra. The Li located at the vertices are shared between neighbouring units by a total of four octahedra. Iodine ions are located in large voids within the structure [204].

1.4 Project Objectives

The aim of the project can be separated into two sections with Li ion conductivity being the link between the two.

The first section focuses on trying to understand the role of order and disorder in the Li conductivity of Li containing garnets. Through truly understanding the Li sublattice it may be possible to improve the Li ion conductivity in these materials. As mentioned in section 1.2.5 there has been confusion regarding the true unit cell symmetry of garnets that contain 7 Li atoms per formula unit. The aim of this thesis is to investigate a range of new garnet systems to give conclusive proof that garnets containing 7 Li atoms will order and form a tetragonal unit cell, and that such Li ordering causes low Li ion conductivity. Through doping into the structure in such systems crystals it is possible to lower the Li content below 7, hence creating disorder in the Li sublattice resulting in a change in cell symmetry from tetragonal to cubic and improved Li ion conductivity. In this project we also investigate the stability of these garnet-type materials to moisture in air.

The second section is based on hydrogen storage materials. As mentioned earlier little work has been done to improve the hydrogen storage properties of the first stage of equation 1.2. It was also mentioned that the incorporation of halides into lithium amide/imide causes an improvement in Li ion mobility and the hydrogen storage properties. Here we investigate the incorporation of halides in the Li_3N structure and compare the hydrogen storage properties to the Li ion conductivity, in order to show that high Li ion conductivity can be linked to improved hydrogen storage properties. We also reinvestigate the structure of several of the lithium nitride halides to give a conclusive determination of their structures.

2. Experimental

2.1 Synthesis

2.1.1 High temperature synthesis[10, 11, 214]

The materials in this project were synthesised *via* the standard ceramic method. This involved weighing stoichiometric amounts of the suitable reagents using an analytical balance (up to ±0.1 mg accuracy). In some cases, an excess of one reagent was added to account for volatility during the high temperature synthesis. The reagents were then ground together to form a homogenous mixture. The sample is then heated to the desired temperature for the required time in an appropriate atmosphere.

Reaction between solids occurs at the interface between particles of reagents. This means that the reaction rate depends on the diffusion rates of the ions to the grain interfaces. For the ions to diffuse toward the grain boundaries they require energy. Therefore these reactions require high temperatures and long reaction times. The grain size of the product will increase as the reaction proceeds; with this the reaction rate decreases as the pathway of the reacting ions increases. To overcome this frequent regrinding between heat treatments is commonly employed to increase the rate of reaction by the creation of new interfaces between the reagent grains, and thus resulting in shorter diffusion pathways.

2.2 Characterisation Techniques [10, 11, 214]

In order to understand the properties of a material a full characterisation of the material is required. In this project a number of different techniques were used.

2.2.1 Crystallography

Crystalline materials are formed from a regular array of atoms repeated in 3 dimensions. The smallest repeating unit which shows the full symmetry is known as the unit cell. Unit cells can be determined *via* X-ray diffraction (XRD) or neutron powder diffraction (NPD)

The unit cell shape is described by several constants called cell parameters. These are the length of the sides normally represented by a, b, and c, and also the internal angles commonly known as α, β, and γ as shown in figure 2.1.

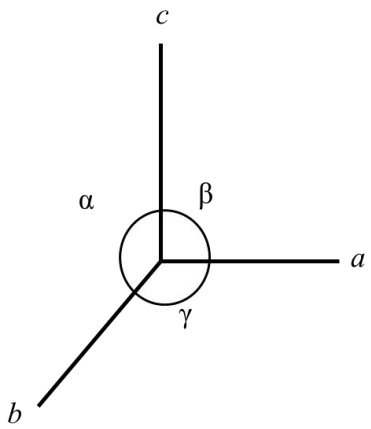

Figure 2.1 Diagram showing cell dimensions

There are 7 different possible configurations of unit cell shapes shown in table 2.1. When classifying a unit cell into one of the classes the relationship between the lattice parameter is to be considered, as each class has its own rules and symmetry requirements.

Table 2.1 The seven different crystal classes

Crystal Class	Relationship between parameters
Cubic	$a = b = c$ $\alpha = \beta = \gamma = 90°$
Trigonal / Rhombohedral	$a = b = c$ $\alpha = \beta = \gamma \neq 90°$
Hexagonal	$a = b \neq c$ $\alpha = \beta = 90°$ $\gamma = 120°$
Tetragonal	$a = b \neq c$ $\alpha = \beta = \gamma = 90°$
Orthorhombic	$a \neq b \neq c$ $\alpha = \beta = \gamma = 90°$
Monoclinic	$a \neq b \neq c$ $\alpha = \gamma = 90°$ $\beta \neq 90°$
Triclinic	$a \neq b \neq c$ $\alpha \neq \beta \neq \gamma \neq 90°$

The unit cell can be described by 4 different types of lattice relating to the position of lattice points in the unit cell (table 2.2). These describe important symmetry features of the unit cell.

Table 2.2 Unit cell types

Type of cell	Description of lattice point
Primitive (P)	Contains one lattice point at each corner
Body Centred (I)	One lattice point at each corner and one in the centre
Face Centred (F)	One lattice point at each corner and one at the centre of each face
Face Centred (A, B, or C)	One lattice point at each corner and a pair in opposite faces ***e.g.*** A has a point in centre of ***bc*** faces

Combining the four types of the unit cell from table 2.2 with the 7 different crystal systems gives 14 Bravias Lattices. The number of Bravias lattices is limited by symmetry requirements of the different crystal classes which limits the number of different combinations. The allowed Bravias lattices are given in table 2.3.

Table 2.3 The 14 Bravias lattice

Unit Cell Class	Permitted Unit Cell Type
Cubic	P, I, F
Rhombohedral	P
Hexagonal	P
Tetragonal	P, I
Orthorhombic	P, I, C, F
Monoclinic	P, C
Triclinic	P

When describing the position of atoms a fractional coordinate is used. A scale of 0 to 1 is used to describe the position on an axis taking 0 as the origin. The positions are presented as x, y and z, representing the positions along the a, b and c direction respectively. A set of coordinates of (0.75 ,0.5, 0.25) would give a position at a three quarter along the a, half way along the b, and a quarter along the c axis.

An alternative way of describing every position of the atoms in the unit cell is known as the asymmetric unit cell, which involves using a small number of lattice points and employing symmetry operations to describe the rest of the unit cell (figure 2.2).

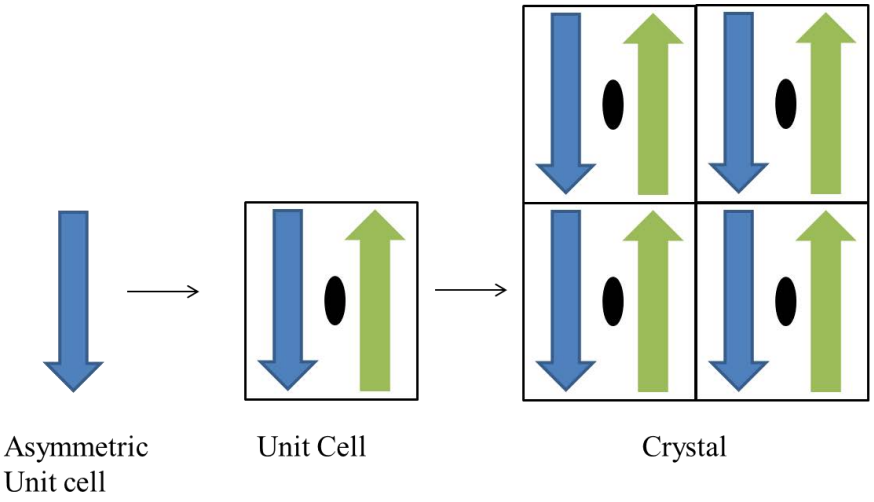

Figure 2.2 Diagram showing the relationship between the asymetic unit cell and unit cell

The symmetry operations are described by 32 point groups. When combined with the 14 Bravias lattices, these gives 230 space groups. The space group thus describes the full symmetry of the unit cell.

When cell parameters, space groups and atomic positions are known, it is then possible to describe fully the unit cell of a phase. These are the usual parameters that are reported in the literature when talking about the structure of a new material.

2.3 X-ray Diffraction

Following initial work by Max von Laue[215] in 1912 on the diffraction of X-rays by crystals, W. L. Bragg and W. H. Bragg[216] devised the technique of X-ray diffraction (XRD) which has become commonly used today for the identification of phases, refinement of structural parameters, identification of lattice strain, and crystallite size.

2.3.1 Generation of X-rays

X-rays are a type of high energy electromagnetic radiation of energy between 200eV – 1MeV. The X-rays that are used in diffraction have a wavelength between 0.05-0.25nm

which is similar to the typical interatomic spacing in a material which are normally in the region of 0.2nm [217]. This therefore makes X-rays ideal in the characterisation of solid state materials

X-rays are generated in an evacuated reinforced glass ceramic tube known as a X-ray tube. Here a tungsten cathode is heated, which produces electrons. The electrons are accelerated down the tube and collide with the anode. The impact with the anode causes a release of energy, the majority of the energy released is thermal energy, while about 1% of the energy released in the form of X-rays.

The electrons that impact on the metal anode produce a range of X-ray wavelengths as the electron interact in different ways resulting in a broad spectrum of energies. The white radiation produced is called “Bremsstrahlung” and is generally not used in diffraction. The radiation that is used in diffraction is produced when an electron from an inner shell gains sufficient energy from a colliding incident electron that it is then ejected. This electron ejection cause the atom to enter an excited state and a hole is produced in the electron shell. To fill the hole an electron drops down from an outer shell. During this process there is a release of energy. The energy that is released has a wavelength that corresponds to the energy difference between the two energy levels. The emitted radiation is characteristic of the metal used in the anode producing sharp lines over the Bremsstrahlung (figure 2.3)

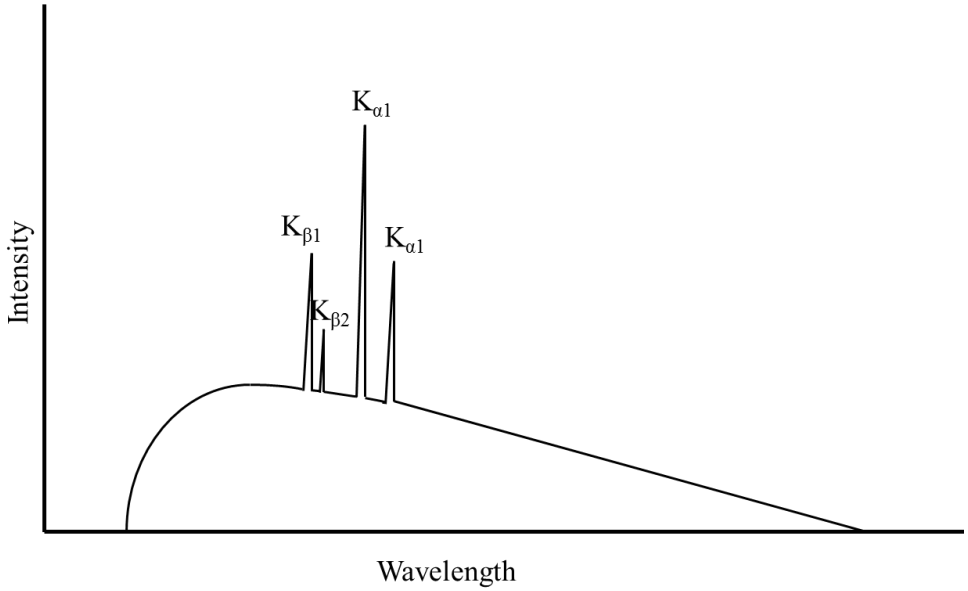

Figure 2.3 X-ray spectrum from bombardment of a metal target (Cu) with high energy electrons

The Bohr model is conventionally used for naming the shells. The K shell (1s) has no subshells, the L shell splits into L_I (2s), L_{II} ($2p_{3/2}$) and L_{III} ($2p_{3/2}$). An electron drops from the L_{III} to fill the hole in the K shell producing the $K_{\alpha 1}$ and L_{II} to the K shell produces $K_{\alpha 2}$ (figure 2.4)

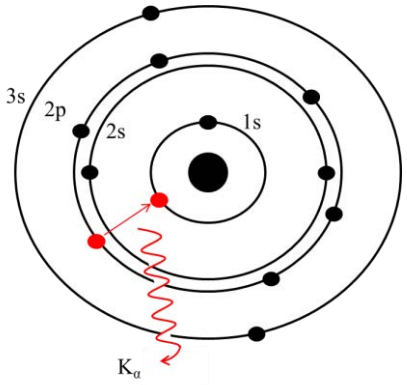

Figure 2.4 Diagram illustrating the electron transitions leading to K_α radiation from a Cu atom

A monochromator is commonly fitted to the XRD instrument. A monochromator is used to "filter" out unwanted radiation. The most common types of monochromators are either a metallic foil or a crystal system. The metal foil works by the incident X-ray beam passing

through the foil which is made of a metal in which the absorption edge lies between that of the K_α and K_β wavelengths. When using a Cu X-ray source a Ni foil is used. A crystal monochromator usually made of graphite or a germanium crystal whose lattice spacing in known, is oriented in such a way that only the $K_{\alpha 1}$ is diffracted towards the sample. In this work 3 different diffractometers were used, two Bruker D8 diffractometers with a $CuK_{\alpha 1}$ radiation source one set in transmission geometry and the second in Bragg–Brentano geometry for variable temperature studies; and a Siemens D5000 diffractometer in transmission geometry with a $CuK_{\alpha 1}$ radiation source.

2.3.2 Scattering

The potential of using a crystal structure to diffract X-rays was first identified by Max von Laue in 1912 using beryl and a photographic plate [218]. When an incident X-ray beam collides with an atom, the electrons begin to oscillate. These electrons can lose this energy through emission of an X-ray beam. This absorption and emission of X-ray beams, is a process known as scattering. When the wavelength of the incident and diffracted beam are equal then the process is known as elastic scattering as there is no loss in energy.

Figure 2.5 shows how two incident beams being scattered from an atom can differ. Here, the incident beams are being scattered by electrons A and B. If the beams continued in the forward direction then then the beams would be in phase as they have both travelled the same distance before and after scattering. As the two beams are in phase the amplitudes of the waves will combine (wavefront X) in what is known as constructive interference. Wavefront Y however, has to travel a further distance as the difference in distance is not a whole number of the wavelength and will therefore reach the detector out of phase leading to destructive interference.

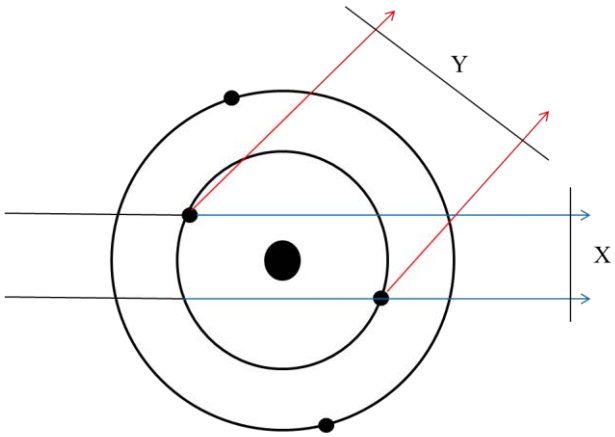

Figure 2.5 Scattering of X-ray waves by an atom

The X-ray scattering amplitude differs for each element and gives rise to the atomic scattering factor (f) which is given in equation 2.1

$$f = \frac{\textit{Amplitude of wave scattered by an atom}}{\textit{Amplitude of wave scattered by one electron}} \quad \textbf{(2.1)}$$

The scattering factor increases with atomic number. This gives some indication to the limitations of XRD technique when studying light elements such as Li, since the scattering will be dominated by heavier elements. This is why other techniques such as powder neutron diffraction are required for structural characterisation of compounds of compounds containing light elements.

2.3.3 Bragg's Law

Through experimentation von Laue derived a series of equations (2.2) to describe a crystal structure from its diffraction pattern [215]. In this approach, a crystal structure is viewed as a regular array of atoms that form a 3-dimensional diffraction grating. The equations consider rows of atoms with a spacing a occurring on the x axis, spacing b on the y axis and spacing c on the z axis. For constructive interference to occur, the pathway distance between incident and diffracted beams must equal a whole number of wavelengths which gives rise to equation

2.2 [219], where $\alpha_n$is the angle of the diffracted beam, α_0 is the angle of the incident beam and $n_x$is an integer (order of diffraction). This can be described similarly for β_n, β_o, γ_n, γ_o, n_y and n_z. Although this approach is mathematically correct it is cumbersome to use, as it requires six angles, three lattice spacings and three integers.

$$\boldsymbol{n_x\lambda = a(cos\alpha_n - cos\alpha_o)}$$

$$\boldsymbol{n_y\lambda = b(cos\beta_n - cos\beta_o)} \quad \textbf{(2.2)}$$

$$\boldsymbol{n_z\lambda = a(cos\gamma_n - cos\gamma_o)}$$

W. H. and W. L. Bragg derived a simpler method. They saw a crystal as being composed of lattice planes that reflect X-rays. Through the laws of specular reflection the angle of incidence equals the angle of reflection. Where the spacing between planes provides a path length equal to a whole number of wavelengths, then the waves undergo constructive interference. While this is an oversimplification, geometrically it is correct and this gives rise to Bragg's Law (equation 2.3) [216].

$$\boldsymbol{n\lambda = 2d_{hkl}sin\theta} \quad \textbf{(2.3)}$$

The indices that are used to describe the reflection planes are named after W. H. Miller who proposed them in 1839 [219], however their importance was not known till years after. The values of h, k and l are given from the reciprocal values of the points of intersections of the plane on the a, b and c edges of the unit cell. So the (421) plane intersects a edge at 0.25, the b edge at 0.5 and the c edge at 1 as shown in shown in figure 2.6.

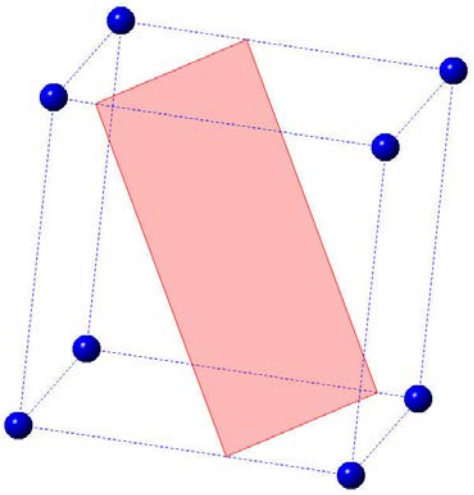

Figure 2.6 Illustration of a (421) plane in a cubic unit cell

The Miller planes are taken as the plane closest to the origin without passing through it. The spacing between two perpendicular planes is known as the d_{hkl} where hkl denotes which set of planes are being studied.

The Miller planes are only referenced to a unit cell and do not necessarily represent planes of atoms in the structure. Indeed, planes of atoms are not usually in the same place as lattice planes. For a given set of lattice planes, when diffracted X-ray beams from atoms within the unit cell interact constructively they will observed as a peak in intensity, so as long as Bragg's Law is obeyed as shown in figure 2.7.

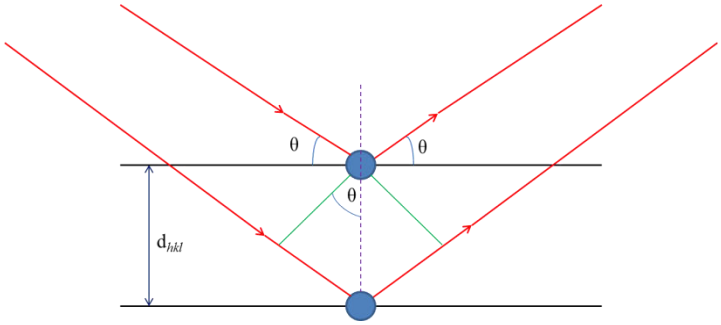

Figure 2.7 A diagram showing Bragg's Law being observed

The d_{hkl} for each set of lattice planes can be calculated by varying θ while λ remains constant. A typical plot of 2θ against observed intensity is given for a powder diffraction pattern for a crystalline material.

2.3.4 X-ray Diffractometer

Two geometries can be used when collecting fixed wavelength, laboratory powder X-ray diffraction data, either transmission (Debye–Scherrer) or reflection (Bragg–Brentano). Both measure as a function of θ. In this work Debye–Scherrer was used. This method exploited a curved perfect-crystal monochromator. The source X-rays are focused not onto the sample but beyond onto the 2θ focusing circle of the detector (figure 2.8). To obtain good quality data the sample is spun about its axis.

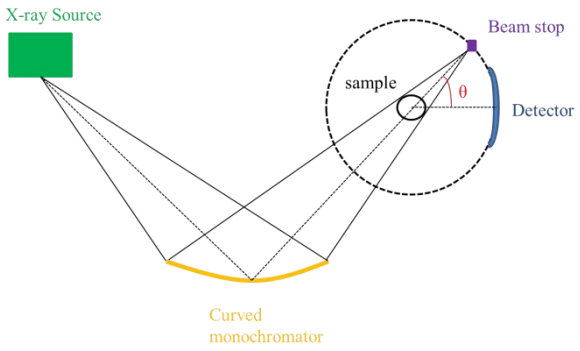

Figure 2.8 Diagram showing Debye-Scherrer geometry

To observe the (hkl) planes in a diffraction pattern then X-rays must interfere constructively. If we consider a primitive cubic unit cell, then the d spacing for the planes can be calculated *via* equation 2.4.

$$\boldsymbol{d_{hkl} = \frac{a}{\sqrt{(h^2+k^2+l^2)}}} \qquad \textbf{(2.4)}$$

This can be combined with Bragg's Law to give equation 2.5 [10].

$$\boldsymbol{sin^2\theta_{hkl} = \frac{\lambda^2}{4a^2}(h^2 + k^2 + l^2)} \qquad \textbf{(2.5)}$$

When studying materials that are not primitive cubic, some absences are seen due to additional centring and these are known as systematic absences. If we consider a face-centred unit cell (figure 2.9) with *hkl* (200) (blue) and (100) (red), the reflections from the (100) plane will be exactly out of phase, meaning that the diffracted X-ray beams will interfere destructively and therefore the (100) will not observed in the diffraction pattern. For an F-centred system an observed reflection must be from planes that have *hkl* values that either all odd or all even. For a body-centred material the sum of the indices must be all even. The systematic absences are applicable to all crystal classes and can be used to determine important information about the material being studied.

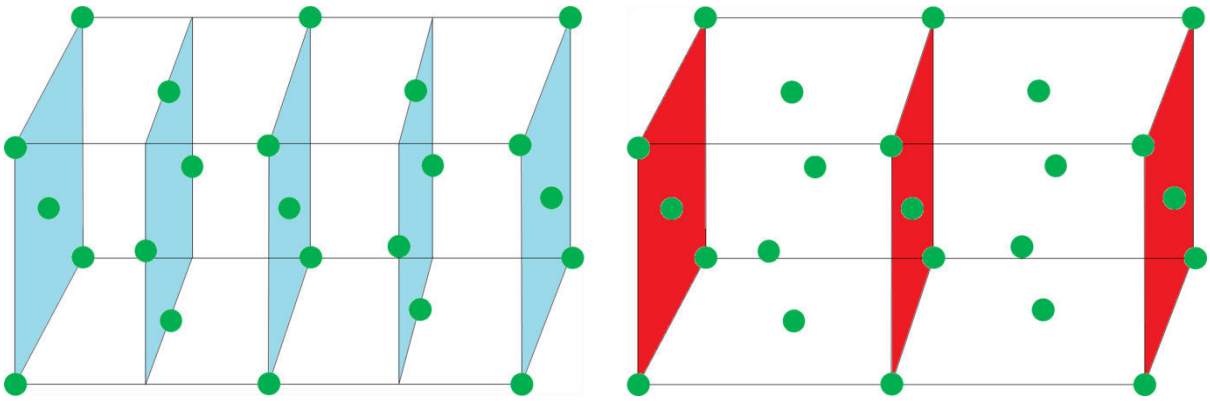

Figure 2.9 Face-centred unit cells with (200) plane highlighted in blue and the (100) plane highlighted in red

Symmetry elements with translational components (screw axis and glide plane) can also cause systematic absences. The presence of these components can be determined when analysing the systematic absences in an X-ray diffraction pattern. Figure 2.10 shows a twofold screw axis (2_1) along the *z* axis, which results in a plane of atoms between the (001) planes. This will cause destructive interference with the reflections from the (001) planes as they lie exactly half way between them. This will be the case where *l* is odd. A glide plane will effectively halve the unit cell in the glide direction. A glide plane perpendicular to the *b* axis is shown in figure 2.10; this would cause the (101) reflection to be absent as the new

plane is half a cell length from the (101), and will therefore interact destructively. Thus only when h is even, can reflections be observed. With increasing unit cell size and decreasing symmetry it becomes increasingly difficult to index diffraction patterns. Consequently for high symmetry cells such as cubic, tetragonal, orthorhombic and hexagonal it is possible to use a simple computer programme to index the pattern, however, lower symmetry cells with more peaks and bad to severe peak overlap become harder to index.

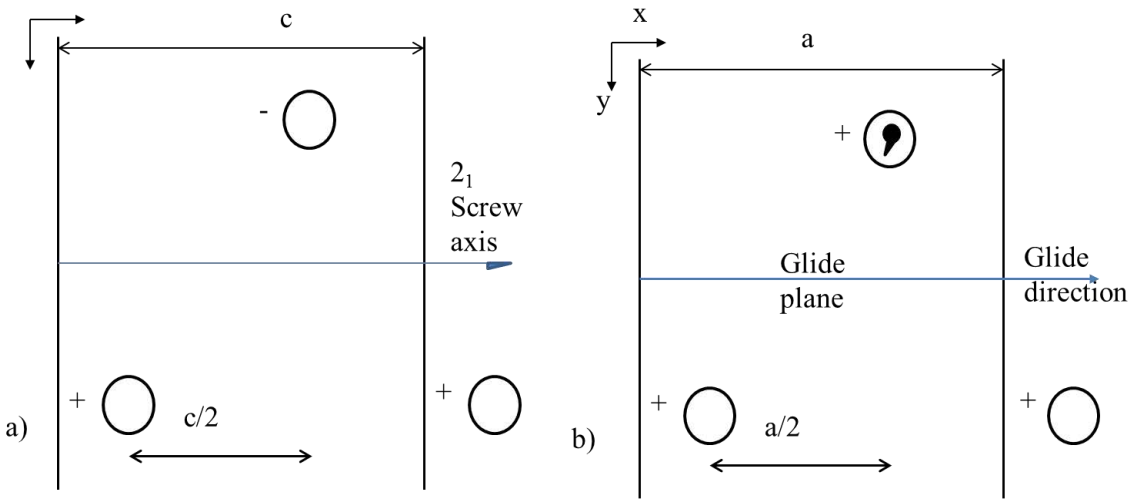

Figure 2.10 Diagrams showing screw axis and glide plane

Figure 2.11 shows a typical X-ray diffraction pattern. A large amount of information can be gathered from the diffraction pattern. The peak positions for each phase gives information regarding unit cell size, although it should be noted that instrumental factors such a zero point error and sample height error can cause shifts in the peak positions.

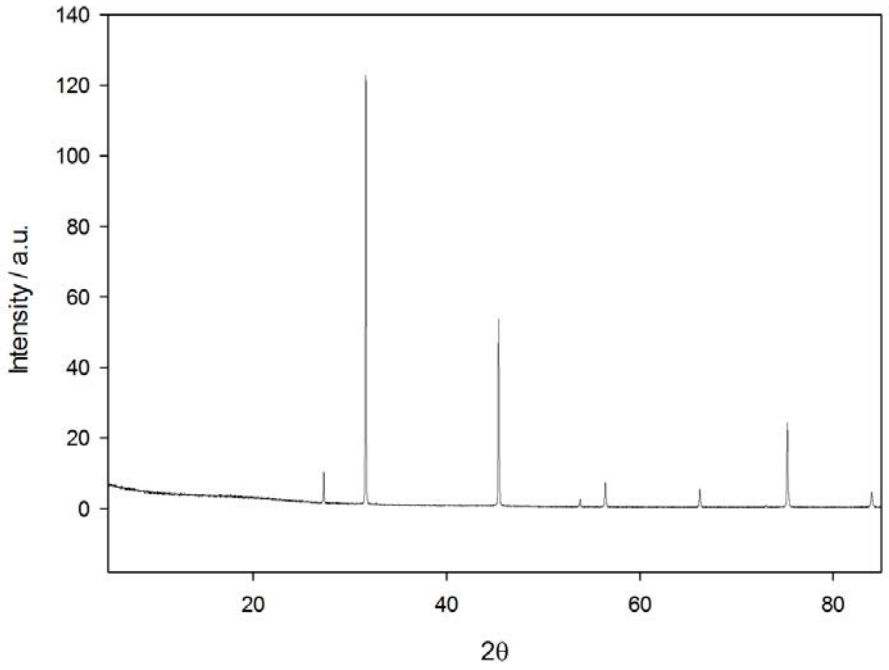

Figure 2.11 Powder X-ray diffraction of NaCl

The peak intensity can give information regarding atomic positions, thermal vibrations, phase fractions and preferred orientation effects. The individual peak intensities will also be affected by the multiplicity of the lattice planes.

The absolute intensity collected for the diffraction pattern is dependent on experimental factors such as the duration and the scattering power of the sample, as well as instrumental factors such as intensity of the applied radiation source and detector efficiency. The overall relative intensity of the Bragg peaks for one phase when compared to another phase is due to the relative abundance of that phase. When crystallite size is small then the peaks will be broader, which will decrease the peak height. The thermal motion of the atoms within the crystal can also decrease the observed peak height for that phase. Microabsorption from the sample will also have a similar effect.

The type, position and thermal motion of the atoms in the crystal structure will affect the relative intensity of a phase. As mentioned earlier systematic absences will also affect the

pattern. It is assumed for powder X-ray diffraction that the crystallites are in a completely random orientation. Should a crystallite be of a certain shape and size (plate-like or needle-shaped) then they may align with each other; this is known as preferred orientation. This phenomenon causes a disproportionate increase in the amount of diffracted intensity from lattice planes that are aligned in the crystallographic plane.

The peak shape can be affected by a number of different factors, some of which are instrumental such as the radiation source and the set-up of the instrument. The sample being studied can also affect the peak profile, and these effects can be microstructural, in particular the grain size and strain. The greatest effect on peak shape, however, is the crystallinity of the sample. Bragg's law is only completely satisfied when the crystallite size is infinite. For a crystal with finite size the diffracted peak will be spread over a 2θ range where the peak shape is related to the crystal morphology. The broadening in the Bragg peak by the sample can be used to calculate the average size of the crystals *via* the Scherrer equation.

External factors will also affect the observed diffraction pattern. The angle of the incident X-ray is one of these factors. An atom has "size" and is not an infinitely small point in space. This means incident X-rays on one part of the atom will diffract differently to those from another part of the atom. The difference in phase at low angles is small, however, at high angles the effect increases which results in destructive interference (figure 2.12). Therefore the peaks at high 2θ values have lower intensity as can be seen in figure 2.11.

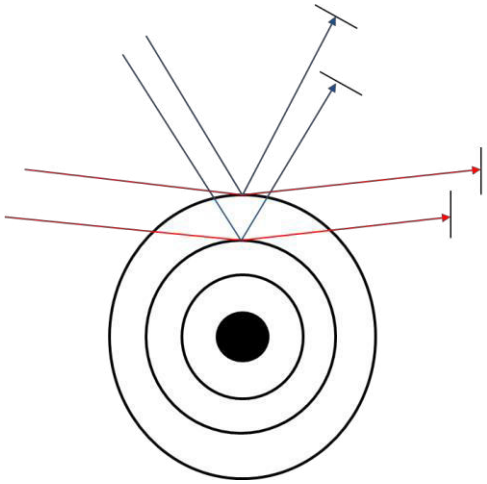

Figure 2.12 Diagram showing intensity reduction with high angle of incidence (blue) and low angle (red)

2.4 Neutron diffraction[220]

Neutron diffraction differs from X-ray diffraction in that, instead of using X-rays, which interact with the electron cloud of an atom, neutron diffraction uses neutrons, which interact with the nuclei of the atoms. This means that the factors that determine the scattering strength from an atom are not dependent on atomic number thus making it typically easier to determine the location of smaller atoms. As nuclei are much smaller than the electron cloud it also means that the reduction in intensity at high angles is significantly reduced, resulting in the situation that neutron diffraction can measure to a much lower d_{hkl} spacing than powder X-ray diffraction.

There are two main types of neutron diffraction experiments, which are "constant wavelength" and "time-of-flight". Constant wavelength neutron diffraction works in a similar manner to X-ray diffraction in that the neutrons used are a fixed wavelength, which is of the same order of magnitude as the interatomic spacing; the wavelength can be calculated from equation 2.6 (λ is the wavelength, h is Planck's constant, m is the mass of the neutron, and v is the velocity of the neutron).

$$\boldsymbol{\lambda = \frac{h}{(mv)}} \quad \textbf{(2.6)}$$

The neutrons are extracted from a nuclear reactor and then passed through a monochromator to select a single wavelength before reaching the sample. Like X-ray diffraction the wavelength is fixed and the angle is varied and thus the collected data is plotted as intensity *vs* 2θ.

In this project time-of-flight neutron diffraction was used. This method differs from constant wavelength in that here the angle θ is fixed and the wavelength is allowed to vary. In this experiment the neutrons are extracted from a pulsed neutron source and the time taken for the neutrons to travel between the neutron source and detector is recorded to determine the wavelength. The wavelength is calculated by using equation 2.7 (here t is the neutron flight time over the path length L). This wavelength can then be used in Bragg's law as discussed previously chapter 2.3.3. Typical plots for time-of-flight neutron diffraction patterns are *d*-spacing *vs* intensity.

$$\boldsymbol{\lambda = \frac{ht}{(mL)}} \quad \textbf{(2.7)}$$

It is possible to generate pulses of neutrons by accelerating a beam of negatively charged hydrogen ions through a thin foil. This removes the electrons creating a beam of protons which is then passed into a synchrotron accelerator. The protons undergo further acceleration and are then separated into two bunches. The bunches are accelerated to ~84% of the speed of light, and they then exit the synchrotron. The accelerated proton beam is then guided towards a heavy metal target such as tungsten. When the beam collides with the target it produces neutrons. Each proton collision produces approximately 20 neutrons from the target.

The instrument used in this project was the high resolution powder diffractometer (HRPD) at the ISIS facility at Rutherford Appleton Laboratories. This instrument is a very high

resolution, moderate intensity diffractometer, which three data collection banks: two ZnS scintillation detectors at 160°–176° (backscattering) and 90° and a ^{3}He-based detector at low angle (28°–32°). For the data analysis in this project only the backscattering bank was used due to the higher resolution of this bank compared to the low angle bank. As the path from the source to the sample is long for HRPD a chopper is utilised. A chopper is a disk-shaped material with slits in it; the disk spins at a precise rate so as to chop the beam between the pulses. This prevents fast neutrons from a pulse catching up with slow neutrons from the previous pulse.

Sample preparation for the experiment involves loading the sample into a vanadium can which is transparent to neutrons. It is typically standard to use a large sample size although there have been advances in technology including new wave guides which means a higher intensity beam reaches the sample that have allowed the possibility to use smaller sample sizes. It is also possible to carry out the experiment in different sample environments including heating the sample in a furnace or cooling to 4 K in a cryostat using liquid He. Performing the experiments under these types of conditions can result in additional peaks in the diffraction patterns from the stages themselves. Therefore is important to take care with the analysis to determine these unexpected peaks.

2.5 Data Analysis

2.5.1 Rietveld Analysis

With enough information it is possible to calculate an accurate diffraction pattern for a given crystal structure *via* Rietveld analysis [221-223]. The basis of Rietveld analysis uses certain structural parameter such as unit cell size and shape, the atomic positions, fractional occupancies and independent thermal parameters to build a crystallographic model. When

this information is combined with experimental parameters that describe peak shape and background shapes a diffraction pattern can be calculated.

These parameters are varied using a least-squares method until the agreement with the observed and calculated diffraction pattern is optimised. This can be shown mathematically by the minimisation of the residual S_y shown in equation 2.8.

$$\boldsymbol{S_y = \sum_i w_i (y_i - y_{ci})^2} \quad \textbf{(2.8)}$$

Where; $w_i = {}^{1}/_{y_i}$, y_i is the observed intensity at the *i*th step, and y_{ci} is the calculated intensity at the *i*th step and the sum is over all data points [223, 224].

For Rietveld analysis the choice of starting model critical i.e. there is a need to have a good starting model. The aim of the analysis is to calculate an accurate crystal structure for each of the phases present in the collected diffraction pattern. There are a number of different contributions to a diffraction pattern, which include background, peak profile functions, peak positions and peak intensities. These will now be discussed in turn.

Any collected diffraction pattern is not completely free of a background. What affects the background is of little interest in a structural refinement. Yet the background must still be fully described. The background functions are usually described by geometrical functions that will fit the background shape the best. The typically used background functions can range from linear interpolation functions [225] to polynomial equations such as the Chebyschev polynomial [226].

For each phase present in a diffraction pattern, a peak shape must also be modelled. There are a number of contributions to this peak shape, such as instrumental and sample influences. The two common mathematical descriptions of symmetric peak shapes are Gaussian and Lorentzian peak shape profiles [226]. By themselves these peak shapes are rarely adequate to

describe accurately the peak profile. A pseudo-Voigt peak shape function is commonly used, which combines both Lorentzian and Gasussian components. Instrumental effects also contribute to the peak shape, and in this project the instrumental peak shape was elucidated by refining a known crystal structure (LaB_6 or Si). This method to determine instrumental parameters was first described by Cheary [227].

The peak positions can be easily determined from the diffraction pattern, and using these it is possible to refine the lattice parameters. Again instrumental factors can affect the peak positons and these factors include zero point error.

In order to calculate the peak intensity for a Bragg peak equation (2.9) is used:

$$\boldsymbol{I_{(hkl)} = K_{(hkl)} F^2_{(hkl)} m_{(hkl)} A_{(hkl)} Lp_{(hkl)}} \quad \textbf{(2.9)}$$

where;

$K_{(hkl)}$ is a proportionality constant,

$F_{(hkl)}$ is the structure factor as described in equation 2.10,

$m_{(hkl)}$ is the multiplicity of the Bragg reflection,

$A_{(hkl)}$ is the absorption correction factor, which depends on the sample composition and the thickness in the direction of diffraction, and

$Lp_{(hkl)}$ is the Lorentz factor, which allows for the probability of observing a reflections at a given diffraction angle, and a radiation polarisation factor.

The atomic positions, site multiplicity and thermal parameters are described by the structure factor equation given in equation 2.10).

$$\boldsymbol{F_{(hkl)} = \sum_j f_j N_j exp\left[2\pi i\left(hx_j + ky_j + lz_j\right)\right] exp\left[-M_j\right]} \quad \textbf{(2.10)}$$

where

f_j is the atomic scattering factor of the *j*th atom type,

N_j is the site occupancy for the *j*th atomic site,

x_j, y_j and z_j are the atomic positions of the *j*th atom in the unit cell, and

M_j is the reduction in scattering powder due to thermal motion which is calculated using equation 2.11

$$\boldsymbol{M_j = 8\pi^2 B_j^2 sin^2\,\theta/\lambda^2} \quad \textbf{(2.11)}$$

Here B_j is related to the root-mean-square thermal displacement of the *j*th atom parallel to the diffracted beam by a factor of $1/(8\pi^2)$.

For a Rietveld refinement, the calculated intensity at any data point within the diffraction pattern is the sum of all contributions from the overlapping Bragg peaks, combined with the corrections from the sample contributions such as preferred orientation and the background. Repeating the refinement of refinable parameters, followed by recalculation of the diffraction pattern, which is then compared with the observed pattern is essential to determining which structural model is the best match to the observed diffraction pattern.

In order to determine the best fit for the calculated diffraction pattern there are a number of statistical measures that can be used. 'R-pattern' given in equation 2.12 and 'R-weighted pattern' given in equation 2.13 are used to compare the whole pattern fitting for the observed and calculated diffraction pattern at each data point.

$$\boldsymbol{R_p = \frac{\sum|y_i(obs) - y_i(calc)|}{\sum y_i(obs)}} \quad \textbf{(2.12)}$$

$$\boldsymbol{R_{wp} = \left[\frac{\sum w_i[y_i(obs) - y_i(calc)]^2}{\sum w_i[y_i(obs)]^2}\right]^{1/2}} \quad \textbf{(2.13)}$$

where $y_i(obs)$ is the observed intensity at the ith point, $y_i(calc)$is the calculated intensity at the ith point and w_i is the weighting.

The optimum R-value for a given data set is 'R-expected' given in equation 2.14, which takes into account the error in the measured intensity.

$$\boldsymbol{R_{exp} = \left[\frac{N-P-C}{\sum w_i y_{oi}^2}\right]^{1/2}} \quad \textbf{(2.14)}$$

where N is the number of observations, P is the number of refined parameters and C is the number of constraints used. This enables the definition of further statistical measure given in equation 2.15.

$$\boldsymbol{GOF = \left[\frac{R_{wp}}{R_{exp}}\right]} \quad \textbf{(2.15)}$$

It is a particularly important statistic as it includes a number of refinable values that are used to calculate the fit, and the fit to the observed data is usually improved by increasing the number of refinable values. When the improvement in the fit is small compared to the quality of the data then the improvement in GOF will be small. When the errors related to poor data quality outweigh the errors from the structural model then GOF will be a very small value.

In the Rietveld refinement the most relevant statistical value is R_{wp}, however, it can give high values if all the peaks are not accounted for or if the background is not properly described. It can also give artificially low values should the background be large. Therefore there is a background-corrected version for this statistical measure $R_{wp'}$ as given in equation 2.16.

$$\boldsymbol{R_{wp'} = \left[\frac{\sum w_i[y_i(obs)-y_i(calc)]^2}{\sum w_i[y_i(obs)-Bkg_i]^2}\right]^{1/2}} \quad \textbf{(2.16)}$$

Numerical criteria of fit are important as they are necessary for the computational application of the Rietveld refinement and they help the programme to proceed towards an ultimate value, yet they should not be used alone. Figure 2.13 shows a typical Rietveld plot which can

be used to compare visually the observed data and the calculated fit. A difference profile between the observed and calculated patterns is shown below the diffraction pattern. If a perfect fit is achieved then this difference plot will be a straight line. Straight bars (tick marks) are used to indicate the calculated Bragg peak positions for each of the phases present in the diffraction pattern.

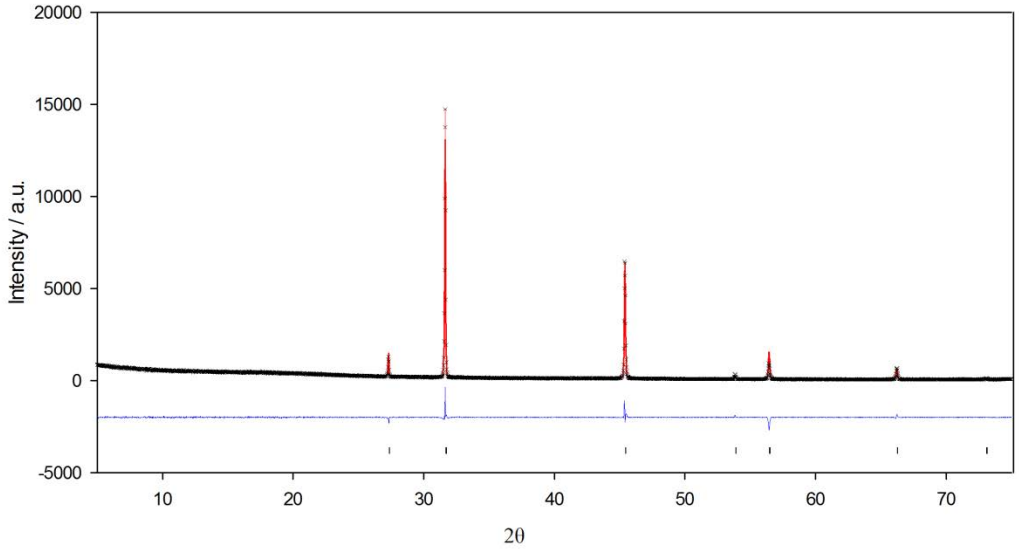

Figure 2.13 Typical Rietveld refinement profile for NaCl

2.6 A.C. Impedance Spectroscopy [228, 229]

Slutyers first reported the use of complex impedance for electrochemical analysis in 1960 [230]. Bauerle [231], a few years later, became the first to use the technique to characterize a solid (yttria stabilized zirconia). The technique has since been extensively used in a number of different fields.

2.6.1 A.C. circuit theory

A sinusoidal voltage can be expressed mathematically as shown in equation 2.17.

$$e = E \sin\omega t \quad (2.17)$$

where

E = amplitude,

ω = angular frequency of rotation, and

ω = 2πf, where

f = conventional frequency (number of complete oscillations per second) in Hertz.

The observed voltage at any time (t) is e (figure 2.14)

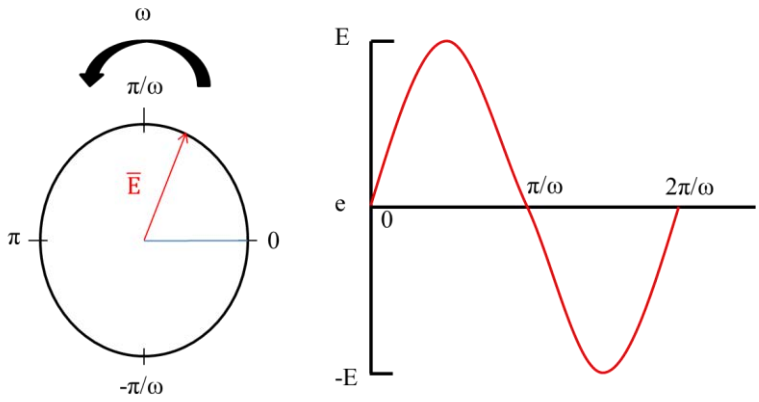

Figure 2.14 Phasor diagram for an a.c. voltage

In order to measure electrochemical impedance, a voltage must first be applied across the sample and then the current response is then measured. As the voltage applied is sinusoidal the response current must be sinusoidal too, however the response current may have undergone a phase shift with respect to the applied voltage. Equation 2.18 states the current including a phase angle (∅) which shows the phase separation with respect to the applied voltage. The phase separation is given a value, the sign of which is dependent on the current lagging behind or running ahead of the reference voltage.

$$\boldsymbol{i = I \sin(\omega t + \emptyset)} \qquad \textbf{(2.18)}$$

Using phasor representation, the voltage is designated $\bar{E}$ and the current $\bar{I}$. E and I have a phase angle which remains constant and is therefore ignored. This leaves the phasors as vectors having a common origin and relevant separation angle as shown in figure 2.15.

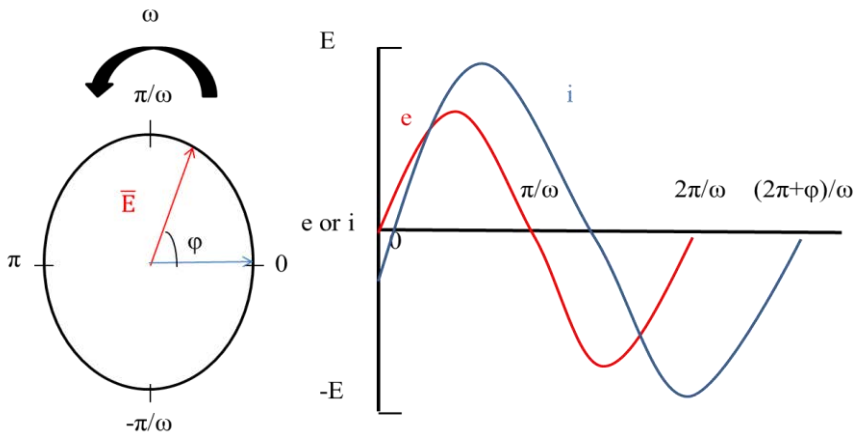

Figure 2.15 Phasor diagram showing the shift in phase between a voltage and current at a frequency ω

When applying a sinusoidal voltage to a pure resistor, the current can be considered as represented in equation 2.19, where R = resistance and Ohm's law is obeyed by $I = \frac{E}{R}$. With this there would be no phase separation between the voltage and current applied.

$$\boldsymbol{i = \left(\frac{E}{R}\right) sin\omega t} \qquad \textbf{(2.19)}$$

In the phasor notation $\bar{I} = \frac{\bar{E}}{R}$ as shown in figure 2.16.

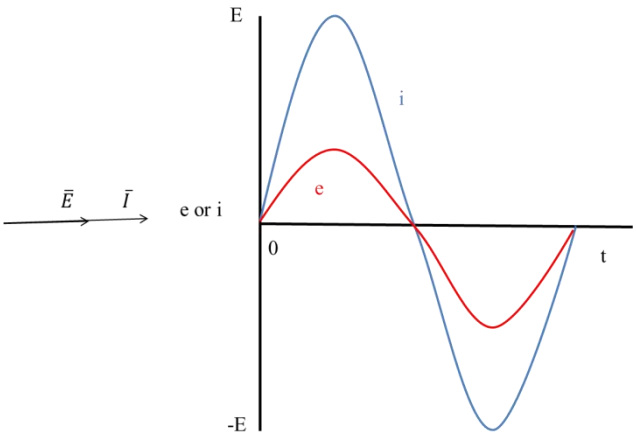

Figure 2.16 The vector relationship between an applied voltage across a pure resistor and the current passing through it

If we replace the pure resistor with a pure capacitor (C) the relationship given in equation 2.20 results.

$$\boldsymbol{i = C\left(\frac{de}{dt}\right)} \qquad \textbf{(2.20)}$$

Including the capacitance reactance $X_i = \frac{1}{\omega C}$, the relationship is fully described in equation 2.21 where the phase angle is $\frac{\pi}{2}$ and the current is ahead of the applied voltage as shown in the phasor diagram in figure 2.17.

$$\boldsymbol{i = \frac{E}{X_c}\sin\left(\omega t + \frac{\pi}{2}\right)} \qquad \textbf{(2.21)}$$

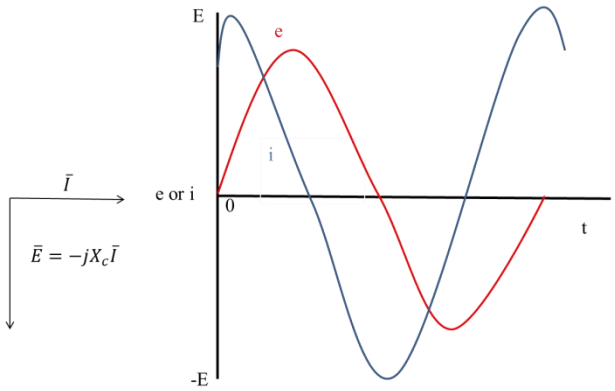

Figure 2.17 Vector relationship between an applied a.c. current and resulting current through a pure capacitor

As can be seen in the vector diagram, the rotation has expanded into a plane. To describe this, complex notation can be used for the component along vertical axis (ordinate component). The ordinate component is therefore assigned as imaginary although in actual terms both components are real in that they are described by the phase angle. The normal convention is to plot the current on the abscissa as shown in figure 2.17, and therefore the voltage can now be described by equation 2.22 where $j = \sqrt{-1}$

$$\bar{E} = -jXc\bar{I} \quad \textbf{(2. 22)}$$

If equation 2.19 is taken into account ($I = \frac{E}{R}$), X_c must carry a resistance component. Resistors are not dependent on frequency but in the case of X_c the magnitude falls as frequency increases. This can be seen clearly when considering a resistor and capacitor in series. When the voltage ($\bar{E}$) is applied across the circuit, the applied voltage is equal to the voltage drop across the individual components, giving equation 2.23 and equation 2.24.

$$\bar{E} = \bar{E}_R + \bar{E}_C \quad \textbf{(2.23)}$$

$$\bar{E} = \bar{I}(R - jX_c) \quad \textbf{(2.24)}$$

The vector (Z) is called the impedance and is given in equation 2.25, and therefore the relationship of voltage and impedance is given equation 2.26.

$$Z = R - jX_c \quad \textbf{(2.25)}$$

$$\bar{E} = \bar{I}\bar{Z} \quad \textbf{(2.26)}$$

This relationship of the components of the voltage and current that is being applied can be summarised in equation 2. 27, where Z_{Re} is the real component and Z_{im} is the imaginary component.

$$\bar{Z}(\omega) = \bar{Z}_{Re} - j\bar{Z}_{Im} \quad \textbf{(2.27)}$$

In this case $Z_{Re} = R$ and $Z_{Im} = X_c = \frac{1}{\omega C}$. The magnitude of Z ($|Z|$) is given in equation 2.28.

$$|\bar{Z}| = \sqrt{R + X_c} = \sqrt{Z_{Re} + Z_{Im}} \quad \textbf{(2.28)}$$

The balance between the resistance and capacitive components in series is described by the phase angle. The phase angle (∅) is equal to zero if only the resistive component has influence, and if only a capacitive component has influence then the phase angle is equal to $\frac{\pi}{2}$. With systems that exhibit a mixture of resistive and capacitive influence then the phase angle is intermediate. The phase angle (∅) is given by equation 2.29.

$$tan\emptyset = \frac{X_c}{R} = \bar{Z}_{I_m}/\bar{Z}_{R_e} \quad \textbf{(2.29)}$$

Impedance is a "real world" generalisation of resistance and consequently therefore equation 2.26 can be considered as a generalised description of Ohm's Law which includes both real and imaginary components. Impedance varies with applied frequency, and this can be plotted on a Nyquist plot which shows $Z_{Im}\ vs.\ Z_{Re}$ for values of ω, which when plotted results in a semi-circle. Due to the similarities of impedance and resistance, rules analogous to those that govern resistance can be exploited to analyse more complex systems and circuits.

The inverse of impedance is admittance, and this is represented as a variation of conductance. equation 2.30 shows the generalised Ohm's law which is written to include admittance.

$$\bar{I} = \bar{E}Y \quad \textbf{(2.30)}$$

When studying parallel circuit models the admittance can be useful, as the overall admittance of a circuit is the sum of the admittances, which is a straightforward and simple way to analyse a circuit model that is parallel.

There are two models that are available when discussing solid state lithium ion conductors using A.C. impedance spectroscopy. The models were proposed in the 1970s and they predict the same response shown in figure 2.18. The first model is the Point Charge Model [232], which assumes the mobile species to be point charges within a continuous dielectric. In this model the distribution of the mobile ions through the electrolyte and at the electrodes is not taken

into account. The second model is the Finite Ion Size Model [233]; this model considers the distance of the mobile ions to their nearest electrode, and also assumes that other charged species are immobile. The two model predictions are the same only if there is only one mobile species and the electrodes are blocking.

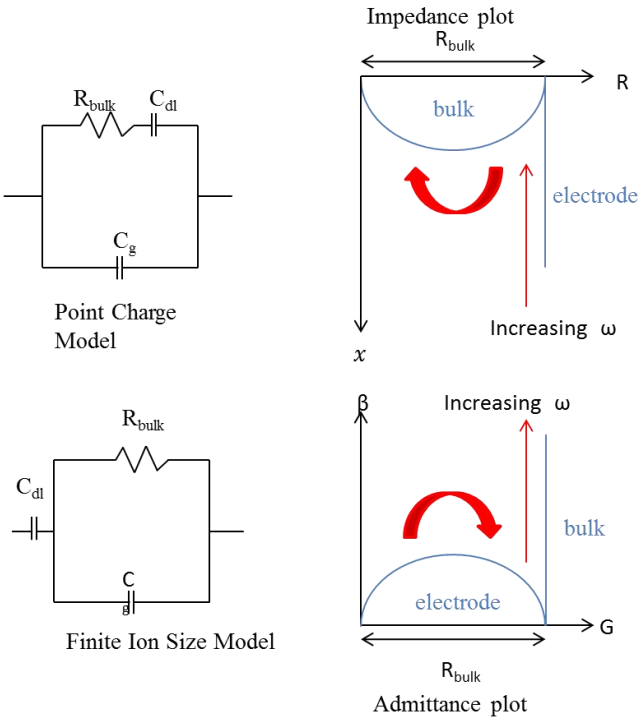

Figure 2.18 Equivalent circuits for the two models (Point Charge and Finite Size) showing both impedance and admittance plots.

The models are based upon equivalent circuits which consist of a two electrode electrochemical cell with a conducting solid electrolyte represented by resistors and capacitors. C_{dl} represents a double layer capacitor which is typically an order of magnitude larger than the geometric capacitor (C_g) if there is good electrolyte–electrode contact and the sample being measured has a high ionic conductivity. At low frequencies, the bulk resistance (C_{dl} and R_{bulk}) dominates whereas at high frequencies C_g and R_{bulk} dominate.

For an ideal measurement of a lithium ion conducting material, a single crystal that is perfectly attached to two perfectly flat electrodes would be required. The mobile ion would then move through the material *via* the mechanism that exists within the material. This mechanism can be generalised as a series of "hops" over potential energy barriers along the direction of the applied field. It is possible to model this through an equivalent circuit which consists of parallel resistive and capacitive components. However, in reality samples are more complex and therefore result in a more complex spectrum. There are a number of contributing factors that can affect the measurement: the powdered nature of the sample, the extent of the sintering and hence the grain size, and also the size of the grain boundary component. The roughness of the surface can cause a less than ideal connection between the electrolyte and electrode. In addition poor adhesion of the conductive paste to the pellet can also affect the measurement. Furthermore, the result will also be affected by charge transfer processes across the interface when using blocking electrodes.

The measurement is conducted over a broad frequency range (1–10^7 Hz) [229]. The applied voltage is a logarithmic stepwise function of frequency. If considering a model of a parallel resistor (R) and capacitor (C), then if the time constants (given in equation 2.31) of the components vary sufficiently, it is possible to resolve the components.

$$\bar{\omega}_{max} RC = 1 \qquad (2.31)$$

In particular, if the time constants differ by several orders of magnitude then the components are clearly distinguishable. However, when they are close together, this will cause the semicircles to overlap, making it difficult to distinguish between two parallel RC components running in series. When analysing the data, the collected data are plotted with the capacitive component ($\bar{Z}_{Im}$) *vs.* the resistive component ($\bar{Z}_{Re}$). From such a plot it is possible to determine R values from the intercept with the $\bar{Z}_{Im}$axis and the C values can be calculated by applying the equation 2.31 to the frequency at the maximum of each semicircle. Typically the

R and C values are calculated using computer software by fitting equivalent circuits to the data. From the C values it is possible to assign a component to a physical phenomenon, and a list of these values and phenomena are given in table 2.4 [229].

Table 2.4 Table showing the link between C values and physical phenomena[229]

Capacitance / F cm^{-1}	**Phenomenon Responsible**
10^{-12}	Bulk
10^{-11}	Minor, second phase
$10^{-11} – 10^{-8}$	Grain boundary
$10^{-10} – 10^{-9}$	Bulk Ferroelectric
$10^{-9} – 10^{-7}$	Surface layer
$10^{-7} – 10^{-5}$	Sample–electrode interface
10^{-4}	Electrochemical reactions

For the lithium ion conducting materials measured in this project the values of most interest are those of the bulk and grain boundary contributions, example diagram shown in figure 2.19. The magnitude of the grain boundary contribution is affected by the sintering of the pellet. The sintering conditions have an influence on the pellet density as well as a number of other factors. The bulk component value is indicative of the conductivity through the grains, which is dependent on the material that is being measured. The ideal spectrum is shown in figure 2.19 where two distinct regions can be assigned to the bulk and grain components.

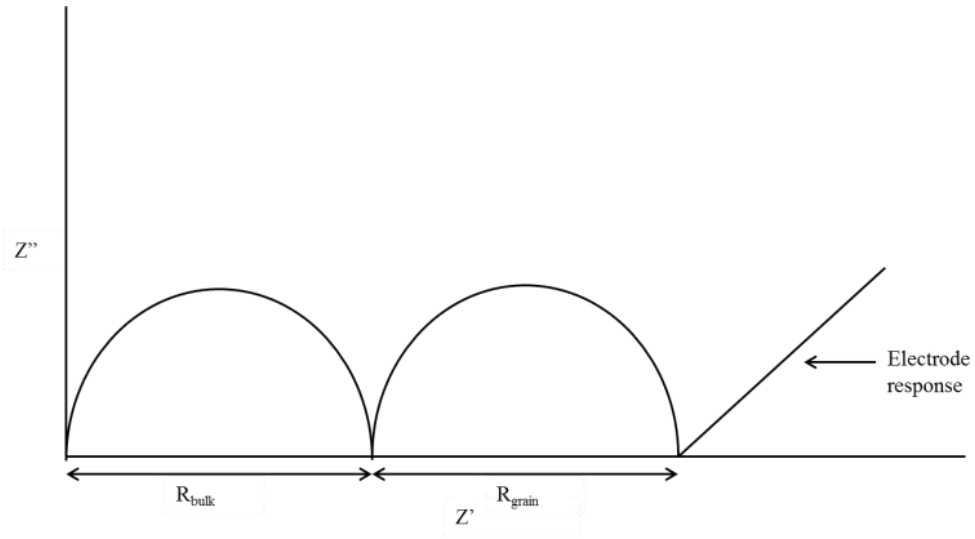

Figure 2.19 Ideal representation of impedance spectra for a solid electrolyte material with bulk and grain components

In the literature the value that is reported is "conductivity". This can be calculated from the resistance obtained from the spectra using equation 2.32 where σ is conductivity, R is the resistance, and F_g is the geometric factor which describes the shape and size of the sample being measured given in equation 2.33 where l is the sample thickness (cm) and A is the surface area .

$$\boldsymbol{\sigma = \frac{1}{R} \times F_g} \quad \textbf{(2.32)}$$

$$\boldsymbol{F_g = \frac{l}{A}} \quad \textbf{(2.33)}$$

Measurements are more often non-ideal. The data analysis software used to fit the semicircles is called Zview 2.8 [234], which can allow the possible separation of the two semi-circles to obtain the individual component values using equivalent circuits. It is essential to have a good understanding of the physical properties of the materials being measured in order to analyse the data properly in this way. In particular, it is possible to fit different equivalent circuits as shown in figure 2.20, with the different models giving the same impedance spectra. A distorted arc can also be encountered instead of a perfect semicircle, as shown in

figure 2.21, which can be caused by non-ideality of the material or by overlapping semicircles.

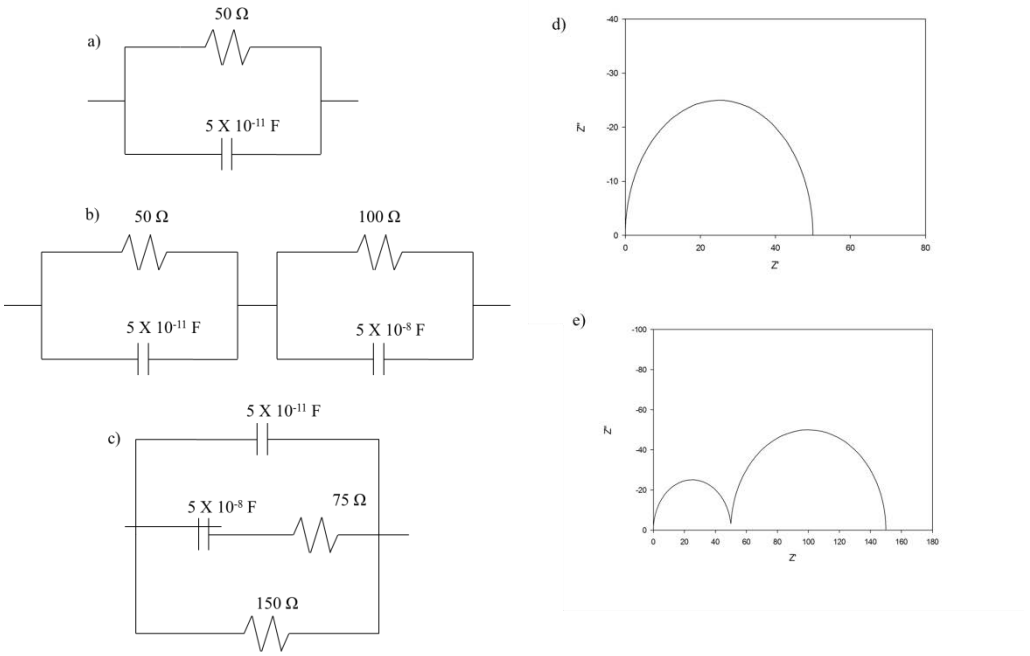

Figure 2.20 Simple RC circuits and the simulated Nyquist plots a) produces plot d), while b) and c) give plot e)

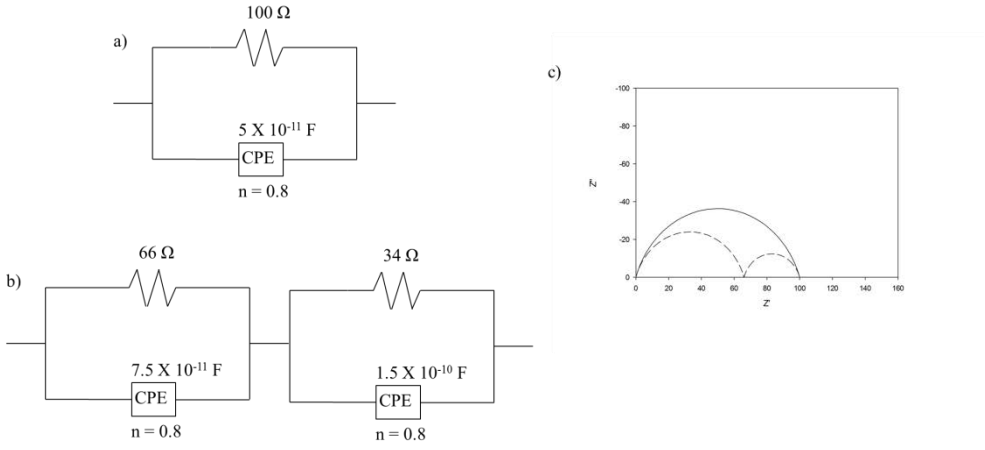

Figure 2.21 Distorted arc and two equivalent circuit models that produce the same arc

When considering a manufactured resistor which is only designed to show an ideal resistive component, it will show a small amount of capacitance and inductance due to it occupying a finite space and the elements are distributed over the space. The ideality of the resistor is restricted to a limited frequency range, as it is not a point element which is assumed in the

mathematical model. A non-homogenous system, where the elements are distributed non-regularly, can result in a distributed relaxation time and resistance. When considering an ionic conductor that conducts through a hopping model, the different local surroundings of the charge carriers can cause a distribution of hopping energies.

Using a constant phase element (CPE) in the circuit given in equation 2.34 can account for the distribution of relaxation times, which is related to the depression angle of the arc.

$$\boldsymbol{Z_{CPE} = \frac{1}{Q_0(j\omega)^n}} \quad \textbf{(2.34)}$$

Here $Q_0 = 1/|Z|$ when ω is equal to 1. When n is equal to 1, then it is an ideal capacitor, and when n is equal to 0 then it is an ideal resistor. Allowing for this non-ideality can improve the fitting of the data when using equivalent circuits. It can be seen in figure 2.21that the same impedance data also can be obtained by using two separate semi-circles. When comparing the capacitance values of the CPE it can be seen they are very similar, and therefore the system can be understood as a distribution of elements. This uncertainty highlights the importance of understanding the physical model, and also shows that is it possible that the equivalent circuit can be simplified further for the system.

In characterising ionic conductors, impedance measurements are collected over a range of temperatures, and can be measured in different atmospheres. It is possible to calculate the activation energy for the conduction process. With changes in temperature the activation energy can also change, which can be a sign of a change in conduction pathway or a change in symmetry. Equation 2.35 shows the temperature dependence of conductivity, which is a related to the Arrhenius-type function. The activation energy is calculated from the gradient of a plot $\mathrm{Log_{10}}$ (σT / S $\mathrm{cm^{-1}}$ K) against $\mathrm{T^{-1}}$ / $\mathrm{K^{-1}}$.

$$\boldsymbol{\sigma T = A \exp^{-Ea/RT}} \quad \textbf{(2.35)}$$

Two instruments were used for this project; a Hewlett Packard 4192A Impedance Analyser and a N4L PSM1735 phase-sensitive multimeter with impedance analysis interface. The frequency range was 1–13000 kHz and the applied voltage was 0.1 V.

2.6.2 Design and testing of air-sensitive A.C. impedance spectroscopy rig

Due to the sensitivity of the lithium halide nitrides and lithium nitride to oxidation when oxygen is present in the atmosphere, a new A.C. impedance containment rig needed to be designed and built. The requirements for the ring were to be as follows:

- Containing rig must be air tight from leaks of O_2 during experiments and transferring from the Ar-filled glovebox and the furnace and impedance analyser
- Must be able to be placed and removed from the argon-filled glovebox easily
- Must be the correct size to have the sample in the centre (hotspot) of the furnace
- Must have ports to allow gas flow in and out of the containment rig
- Must be able to withstand temperatures in excess of 400°C
- Must have connection wires to the A.C. impedance analyser and temperature probe reader
- Sample pellet must be in good contact with the wires that connect to the impedance analyser
- Must be able to record accurately the temperature as close as possible to the pellet position
- The rig must not become short circuited during movement or during the experiment
- Materials used must not add to the resistance of the pellet

To ensure that there was no leakage into the rig when the pressure inside the rig was equal to the pressure outside, quick fit connections were used between any interconnecting piece of

the rig. To help prevent the leakage further high vacuum grease could be applied to these areas.

To allow protective gases to flow over the sample while being analysed, connecting tubes were to be added, however, these would require taps to prevent air leaking into the sample chamber before the protective was connected.

To allow for transfer of the rig in and out of the argon-filled glovebox, the dimensions of the largest port on the glovebox were measured and all final measurement dimensions of the assembled rig were not to be bigger than those of the large glovebox port.

As the centre of a furnace is the point at which the temperature of furnace is closest to its programmed temperature. The point at which the pellet would be located in the rig during the experiment had to be measured and included in the design process. This was also true with the positioning of the thermocouple within the chamber; it was required to be close to the pellet in order measure the temperature accurately.

As the experiments would require high temperatures the material that the rig was to be constructed out of must be able to withstand temperatures greater than that of the maximum temperature of the experiment. As quartz has a melting point of >1000°C it is an ideal material to use to construct the rig out of.

As the A.C. impedance analyser and temperature probe require connections to wires within the rig to allow for analysis, wires exiting the rig were required. At the point of exit for the wires a seal would be required to prevent leakage of O_2 into the chamber. These wires could then be used in conjunction with a foil made from the same material (i.e. Pt, Ag or Au) to connect the pellet to the analyser. Silver was chosen as connecting wire as the conductive paste used to adhere to the surface of the pellet was also silver as it required less high

annealing temperatures than gold or platinum. Also Ag would also add negligible resistance the readings collected from A.C. impedance spectroscopy.

To prevent the silver wires from touching causing a short circuit, an alumina tube with 3 bored holes was used, into which the Ag wires and thermocouple were threaded. Alumina was used due to its high melting point.

Figure 2.22 shows the resulting design of the rig.

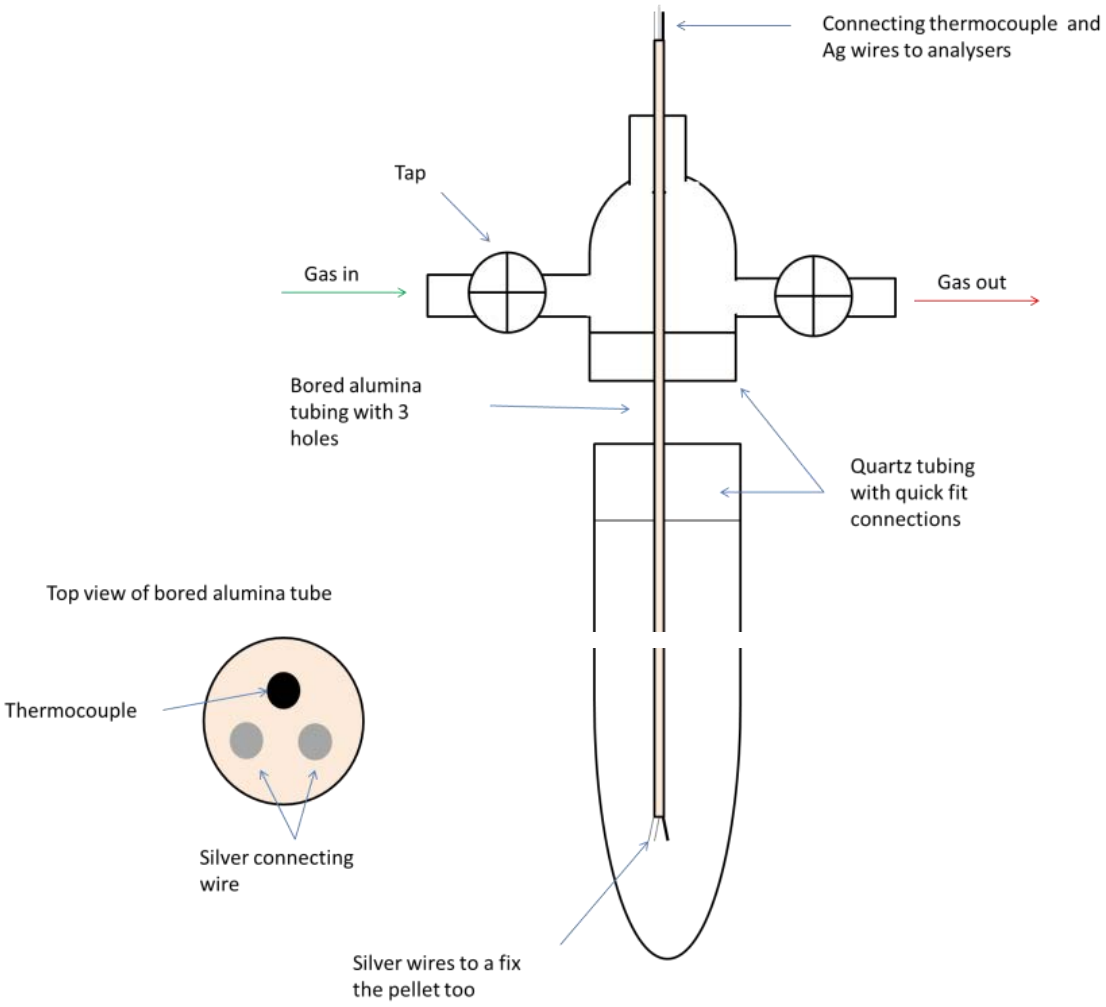

Figure 2.22 Schematic diagram of air-sensitive A.C. impedance containment rig

Figure 2.23 shows the final constructed rig.

Figure 2.23 Finished constructed air-sensitive A.C. impedance containment rig

To ensure that the rig worked correctly, testing was required. To start, the A.C. impedance of an air-stable material was measure. The material used was $Ce_{0.9}Gd_{0.1}O_{1.95}$ (CGO). A pellet of CGO was pressed into a pellet and sintered at 1200°C for 12 hours. Resulting in a pellet with 92% theoretical density. Ag paste was used to ensure a good electrical contact. Figure 2.24 shows the Arrhenius plot of CGO measured using the air-sensitive rig designed above and previously measured sample in a standard rig. As it can be seen it is in good agreement with previously measured sample. It was therefore determined that tests on air-sensitive Li_3N would be required to test how well sealed the rig is. X-ray diffraction patterns were collected before and after the measurements and no change in the diffraction pattern was observed (figure 2.25); again the Arrhenius plot showed good agreement with previous reports (figure 2.26).

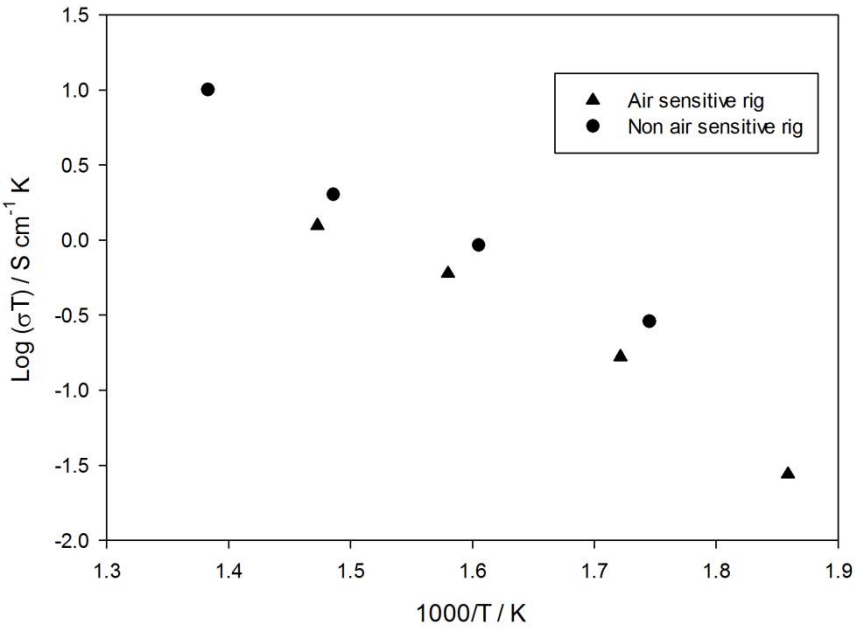

Figure 2.24 Arrhenius plot of CGO measured using the air-sensitive rig (triangle) and non air-sensitive rig (circle)

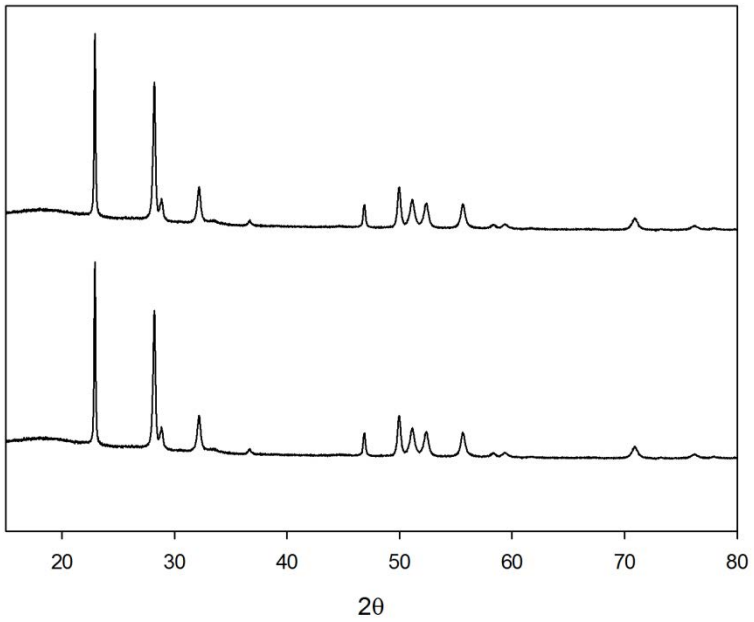

Figure 2.25 X-ray diffraction pattern of a) Li_3N after sintering b) Li_3N after A.C. impedance measurements

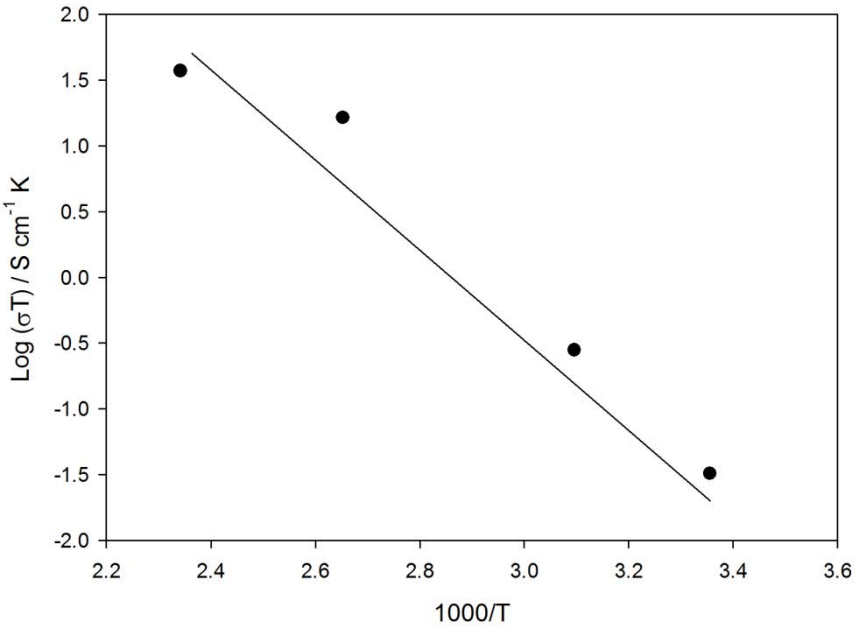

Figure 2.26 Arrhenius plot of measured Li_3N (circles) and reference plot (line)[235]

After completing these series of tests it was determined that all criteria had been met in the design stage and that the rig was working correctly providing reliable results.

2.7 Solid State Nuclear Magnetic Resonance Spectroscopy [236, 237]

Nuclear magnetic resonance (NMR) spectroscopy is an experimental technique, which is capable of providing the local environmental configuration of nuclei. It can be used to complement or back up other techniques such as X-ray/neutron powder diffraction. NMR is able to exploit the magnetic properties of atomic nuclei of the material, which have an intrinsic nuclear spin momentum. All elements including their isotopes have a nuclear spin quantum number (I) which has a value of n/2 (n is an integer). However not all nuclei are NMR active. The spin quantum number must be non-zero and the nuclei will have a magnetic moment (μ) (equation 2.36). γ is gyromagnetic ratio, the ratio of magnetic dipole moment to angular moment, which is characteristic of an isotope of a particular element. In this study ^{71}Ga was the nucleus investigated, which has a spin quantum number of 3/2

$$\boldsymbol{\mu = \frac{h\gamma}{2\pi}[I(I+1)]^{1/2}} \quad \textbf{(2.36)}$$

Nuclear moments orient themselves when a magnetic field is applied; a nucleus of spin I will have 2I + 1 possible orientations. These are identified by the magnetic quantum number (m_I) which has values of I, I−1 , I−2 I−3, etc. ^{71}Ga has values −3/2, −1/2, 1/2, 3/2. A nucleus where I = 3/2 will have energy levels split as shown in figure 2.27, which is known as Zeeman splitting. NMR transition selection rules state that $\Delta m_I = \pm 1$. The transition energy is given in equation 2.37. As $\Delta E = h\nu$, the energy difference between each of the energy levels has a corresponding frequency, which is given in equation 2.38). NMR measures these energy transitions.

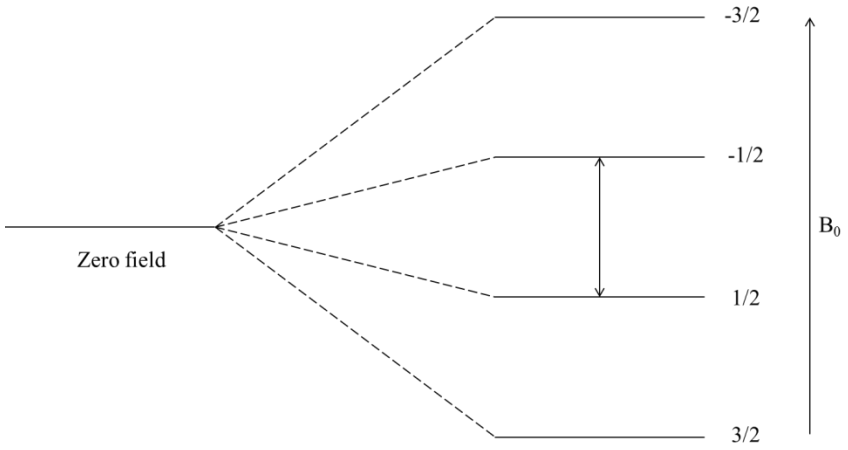

Figure 2.27 Energy levels for a nucleus where I = 3/2 in a magnetic field

$$\boldsymbol{\Delta E = \frac{\gamma h B}{2\pi}} \quad \textbf{(2.37)}$$

$$\boldsymbol{\nu = \frac{\gamma B_0}{2\pi}} \quad \textbf{(2.38)}$$

Transitions between energy levels occur when a radiofrequency with the same energy as the splitting is applied.

2.7.1 Chemical shift

When a crystal structure containing the nuclei under investigation is subjected to a magnetic field, the electrons within the structure shield the nuclei from the applied magnetic field. The applied field is therefore not equal to the field experienced by the nuclei. The difference, which is referred to as the nuclear shielding, is proportional to the applied field.

The definition of the chemical shift is the difference between the resonance frequency of a particular nucleus and that of the standard reference (equation 2.39). It is reported in the δ scale (ppm)

$$\boldsymbol{\delta} = \left(\frac{\boldsymbol{v} - \boldsymbol{v_{ref}}}{\boldsymbol{v_{ref}}}\right) \times 10^6 \qquad \textbf{(2.39)}$$

Chemical shifts are determined by different chemical environments such as coordination number, nearest neighbour type, type of next nearest neighbour and crystallographic inequivalence. Changes in the chemical environments would result in a change in the electron density and therefore changing the shielding effect of the electrons, which results in a change in the chemical shift.

2.7.2 Quadrupolar Interaction

Spectral line shape can be affected by the symmetry of the charge distribution of the nucleus. A nucleus with I = ½ has a spherical electrical charge distribution, which results in a Gaussian line shape. Nuclei that have I ≥ 1 have a non-uniform electric charge distribution. This causes distorted spheres and a charge gradient across the nucleus. These nuclei are quadrupolar (^{71}Ga is therefore quadrupolar). An interaction between an electric field gradient and the non-spherical charge distribution caused, results in a change in the energy level in addition to the Zeeman Effect. The interaction strength is measured as the quadrupole moment. This results in broader line widths, making it difficult to determine reliable chemical shifts.

For nuclei with spin I > ½ the non-spherical symmetry of the nuclear electric charge distribution interacts with any electric field gradients, altering the previously equally split Zeeman levels. When applying a magnetic field to a nucleus where I =3/2 (^{71}Ga), the four previous degenerate states become distinct energy levels, described by the magnetic quantum number m_I figure 2.27. The effect of the first order quadrupolar interaction with the electric field gradient is that it disrupts each of the energy levels by a small amount. The small disruption causes satellite peaks to appear either side of the most intense peak in the spectrum due to the non-central energy level transitions ($m \neq 1/2$) being shifted, while the main central transition is not affected. The first-order disruption of the energy levels is shown in figure 2.28.

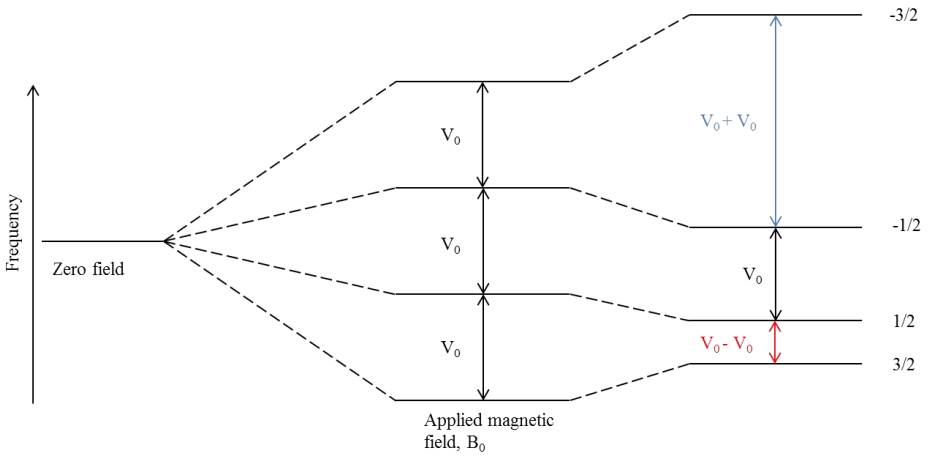

Figure 2.28 Quadrupolar splitting of the nuclear spin energy levels in an applied magnetic field

When the quadrupolar coupling is sufficiently strong, a second order disruption occurs in addition to the first-order effects. The energy bands are shifted again, which results in the central line undergoing a significant anisotropic broadening.

Collecting the spectra at high field can help to minimise the second order quadrupolar broadening, because the intensity of the quadrupolar interaction is inversely proportional to the field strength.

2.7.3 Magic Angle Spinning

When using solution NMR the rapid molecular movement averages many line broadening interactions to zero. In solid state NMR these interactions, however, are not reduced to zero and so result in broad lines. However, it is possible to reduce line broadening by using the technique of magic angle spinning. This involves spinning the sample about an axis at an angle θ (54.7°) to the applied magnetic field. The line broadening term contains the expression $3\cos^2\theta-1$; when θ = 54.7° the term then becomes zero. In some cases the spinning rate is not sufficient enough to remove all the interactions and the spectra will then contain a main central line with spinning side bands. Only first order quadrupolar interactions can be suppressed in this way as the second order interactions contain different line broadening terms that require θ to equal 30.6° and 70.1° to eliminate. It is necessary to run multiple quantum magic angle spinning NMR to supress these broadening effects.

2.8 Raman Spectroscopy [238]

Raman spectroscopy is a form of vibrational spectroscopy that can be used to observe molecular and crystal vibrations by the process of Raman scattering. The sample is irradiated with a single wavelength of radiation (from infrared to ultraviolet). The scattered radiation from the molecules, which is shifted by one unit of vibrational energy, is detected. The difference between that energy and the incident energy is what is of interest in vibrational spectroscopy.

During scattering the incident light interacts with the molecule causing the electron cloud surrounding the constituent nuclei to become polarised to form a short lived excited state known as a "virtual state". The energy of this excited state is dependent on the energy of the incident radiation. This state relaxes quickly as it is unstable. On relaxation a photon is released of a different energy. In scattering events, only the electron cloud is involved and the difference in energy between the two photons (incident/scattered) will be very small due to electrons being light. This form of scattering is known as Rayleigh scattering, and can be regarded as elastic. Occasionally in scattering events nuclear motion may be induced in the molecule. Here a significant amount of energy may be transferred between the photon and molecule. These events are inelastic and known as "Raman scattering". The energy differs here between the incident photon and the motion induced in the molecule. In Raman spectroscopy the nuclear motions induced by inelastic scattering events are of the form of molecular vibrations. Figure 2.29 shows the energy exchange during the scattering processes.

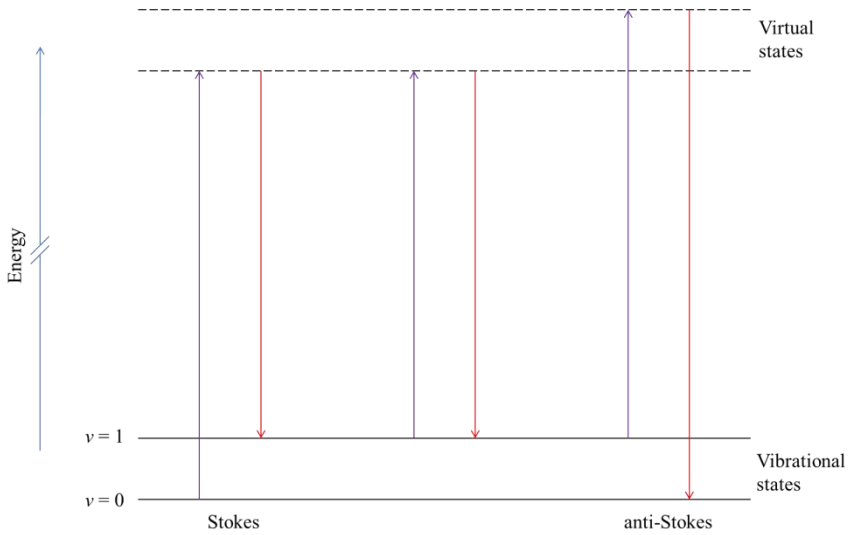

Figure 2.29 Diagram showing the energy exchange during the scattering process

The majority of scattering events are Rayleigh type, where there is no change in the energy of the photons involved. In Raman scattering the absorption of the energy of the lowest vibrational state (ground) causes the molecule to be excited to a higher vibrational state (excited). The scattered photon will therefore be reduced in energy by the energy of excited state, and this is known as Stokes scattering. If a molecule, which is excited to the vibration state $v = 1$ as shown in figure 2.29, undergoes scattering, the vibrational energy is transferred to the scattered photon, increasing the energy relative to that of the incident radiation. This is known as anti-Stokes scattering. The majority of molecules when at room temperature have their lowest energy vibrational state of $v = 0$ as shown in figure 2.29 and therefore Stoke scattering is the dominant form of Raman scattering used in Raman spectroscopy. If the temperature is increased, the relative amount of anti-Stokes to Stokes scattering will increase. For a vibrational mode in a molecule to be Raman active it must cause the magnitude or the direction of the polarisability of the molecule to change. The bands that are the most intense are usually due to symmetrical vibrations, whereas asymmetric vibrations are weak.

In this project the Raman spectra were collected on a Renishaw inVia Raman microscope operating with a 633nm excitation laser. Samples were loaded into a sample holder in a Ar-filled glovebox to prevent oxidation of the sample.

2.9 Mass Spectrometry [239, 240]

Mass spectrometry is a technique that measures the amount of gaseous ions with a certain mass to charge ratio, known as m/z. A mass spectrometer is capable of scanning across a range of m/z ratios and is also able to determine the relative amount of each species observed. It is also possible to select certain m/z values of interest to determine the amount in a given analyte. Ions are charged species and so can be manipulated with an electromagnetic field. A mass spectrometer uses electromagnetic fields to separate the

charged ions in the gaseous phase at very low pressure, to detect the species according to their m/z values. The use of a vacuum to maintain the low pressure is essential in this process as it prevents the ions from colliding with each other. There are three main components to the mass spectrometry experiment: ionisation, separation and detection.

2.9.1 Ionisation

The ionisation process converts atoms/molecules of the analyte into charged gas phase ionic species *via* either the addition or the removal of an electron or proton. There are a number of different types of ionisation sources used in mass spectrometry; the most common for a gas phase analyte is electron ionisation, which was used in this project.

In this process an electron beam that has been generated from a tungsten filament is used to knock an electron from the analyte atom or molecule, which creates a singly charged cation. The electron beam energy is tuned to cause a significant amount of singly charged cations, but without multiple ionisations.

After the ionisation it is possible for the cations to fragment. This occurs when excess energy from ionisation causes the cation to break up into smaller pieces, and the smaller charged fragments will be detected by the mass spectrometer at correspondingly lower m/z ratio. Molecules will display a characteristic fragmentation pattern dependent on the ionisation energy used. This is helpful in phase identification of large organic molecules. The fragmentation process is an important part of mass spectrometry that should not be overlooked. For an analytical determination of an analyte, the fragmentation behaviour of the analyte should be understood.

2.9.2 Separation

The separation of charged ions takes place in the analyser and occurs due to the different m/z values. The first mass spectrometer analysers were basically a tunable electromagnet, known as a magnetic sector analyser. Here the m/z values determine how much the charged species are deflected by the magnetic field. The lighter species are deflected more by the electromagnet than the heavier species that have the same charge. By varying the strength of the magnetic field, it is therefore possible for the mass spectrometer to successfully "aim" the different m/z values at the detector.

Newer systems make use of a quadrupole mass analyser. Instead of bending the charge particles in a radius that is dependent on their m/z values, a quadrupole mass analyser uses an electric field oscillating at radio frequency, which can selectively stabilise or destabilise the species passing through it. It is possible to select which m/z values are stabilised by the frequency of the oscillation, and therefore determine which species reach the detector. m/z values that are not of interest are then scattered or neutralised in collisions and do not reach the detector. A diagram comparing these two methods is shown in figure 2.30 .

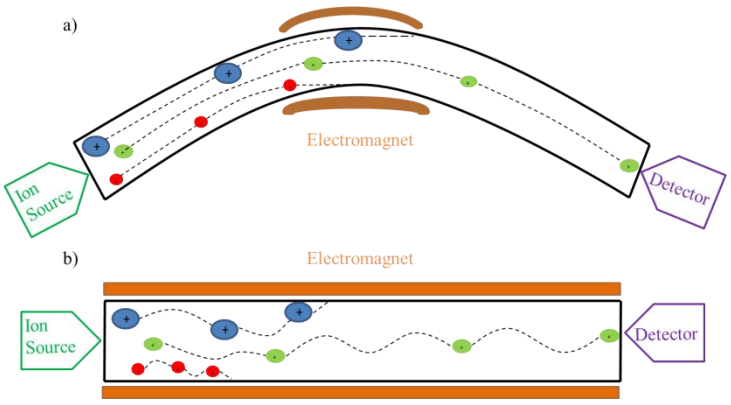

Figure 2.30 Diagrams comparing a) magnetic sector and b) quadrupole mass spectrum analysers

2.9.3 Detection

The detector measures the ion current of the m/z value hitting it, and the signal is amplified with the data output as a mass spectrum. For large ion currents produced by the majority of the analyte a Faraday cup detector can be used to both collect and separate the ions. A Faraday cup is a conducting cup that releases electrons when it is hit by a charged species. The current, which is directly proportional to the number of ions that are detected, is amplified and recorded if a greater sensitivity is required. It is possible to use a (secondary) electron multiplier; here the electrons produced *via* the collisions of the ions of interest are then amplified in a series of electrodes, each of which is at an increased potential. This creates a cascade of electrons for each of the electrodes, which results in an amplification and increased sensitivity in the order of $\times 10^6$.

2.10 Thermal Analysis

Thermal analysis is used to measure changes in a material with varying temperature. A number of techniques fall into this category and measure a range of properties including mass change, volume, and heat flow. In this project two techniques were used: thermogravimetric analysis (TGA) and temperature programmed desorption (TPD)

2.10.1 Thermogravimetric analysis (TGA) [241]

TGA is a technique that accurately measures the weight of a sample while it is being heated in a controlled atmosphere. The sample is placed in an aluminium oxide container and the weight is recorded as a starting point. The weights recorded throughout the experiment are then considered relative to the initial weight. This means that that TGA results are given in percentage weight change. The atmosphere of the experiment can also be controlled by gas flow. All measurements in this project were carried out using a nitrogen atmosphere,

however, there are a number of alternatives including air, oxygen, carbon dioxide and hydrogen. Controlling which atmosphere is used in the experiment allows us to study processes occurring in the material. To avoid oxidation occurring in the sample, then gases such as nitrogen and argon can used. By placing a thermocouple close to the sample it is possible to monitor the temperature of the sample accurately. The rate of heating can also be controlled to match the requirements of the experiment. Slow heating rates are used to obtain higher quality data. It is also possible to perform cycles of heating and cooling, or heat and hold the temperature for a set period of time. A plot of percentage weight *vs.* temperature is often reported.

In this project TGA studies were performed using a Netzsch STA 449 F1 Jupiter Thermal Analyser. The heating programme was a steady linear heat (10°/min) with a gas flow of 60 ml min^{-1}. The TGA instrument was coupled with a mass spectrometer (see chapter 2.9) to analyse any gases released on heating

3. Effect of Ga incorporation on the structure and Li ion conductivity of $La_3Zr_2Li_7O_{12}$

3.1 Publication

Title: *Effect of Ga incorporation on the structure and Li ion conductivity of $La_3Zr_2Li_7O_{12}$*

Submitted: 19th June 2012

Accepted: 10th August 2012

Information: *Dalton. Trans.*, 2012, 41, 12048-12053

Times cited: 16 (20th September 2015)

Author contributions; M.A. Howard: The synthesis of $La_3Zr_2Li_7O_{12}$ and $La_3Zr_2Ga_{0.5}Li_{5.5}O_{12}$, X-ray diffraction, neutron diffraction, A.C. impedance spectroscopy and thermogravimetric analysis studies. Analysis of ^{71}Ga solid state NMR data

O. Clemens: Guidance on combined X-ray and Neutron diffraction Rietveld refinement

E. Kendrick: Guidance on Neutron diffraction Rietveld refinement

K.S. Knight: Lead beam line scientist at HPRD Isis Rutherford Appleton Laboratories

D.C. Apperley: Running of the ^{71}Ga solid state NMR experiment at University of Durham solid state NMR facility

P.A. Anderson: Supervision to M.A. Howard

P.R. Slater: Lead supervisor to M.A. Howard

3.2 Highlights

- Confirmation that undoped $La_3Zr_2Li_7O_{12}$ is tetragonal and has a low Li ion conductivity, due to ordering on the Li sublattice.
- Doping with a small amount of Ga on the Li site leads to a change to a cubic unit cell, and a large improvement in the Li ion conductivity.
- Combined Rietveld refinement of powder X-ray and neutron diffraction data complemented by ^{71}Ga solid state NMR show that $La_3Zr_2Ga_{0.5}Li_{5.5}O_{12}$ has Ga substituted onto the ideal tetrahedral site. The presence of Ga^{3+} on the Li sites introduces vacancies in the Li sites, and consequent disorder on the Li sublattice, and hence leads to the observed enhancement in Li ion conductivity.
- Exposure to air shows evidence of some H^+/Li^+ exchange, which causes variation in the conductivity, thus illustrating the care needed when evaluating these garnet Li ion conductors.

Dalton Transactions

Cite this: *Dalton Trans.*, 2012, **41**, 12048

www.rsc.org/dalton

PAPER

Effect of Ga incorporation on the structure and Li ion conductivity of $La_3Zr_2Li_7O_{12}$

M. A. Howard,[a] O. Clemens,[a] E. Kendrick,[a] K. S. Knight,[b] D. C. Apperley,[c] P. A. Anderson[a] and P. R. Slater*[a]

Received 19th June 2012, Accepted 10th August 2012
DOI: 10.1039/c2dt31318a

In this paper we examine the effect of Ga doping on the structure and conductivity of the high Li ion content garnet-related system, $La_3Zr_2Li_7O_{12}$. Without Ga doping, $La_3Zr_2Li_7O_{12}$ is tetragonal and has low Li ion conductivity. The introduction of Ga leads to a change to a cubic unit cell, and a large enhancement in the conductivity. Prior structural studies of $La_3Zr_2Li_7O_{12}$ have shown the presence of both tetrahedral and distorted octahedral sites for Li, and the low conductivity can be explained by the ordered nature of the Li distribution. The present structural study of $La_3Zr_2Ga_{0.5}Li_{5.5}O_{12}$ shows that Ga substitutes onto the tetrahedral site. Despite the presence of non-mobile Ga^{3+} on the Li sites, the conductivity is enhanced as a result of the introduction of vacancies in the Li sites, and consequent disorder on the Li sublattice. Further work has suggested that over time in air, there is some H^+/Li^+ exchange, and consequently some variation in the conductivity.

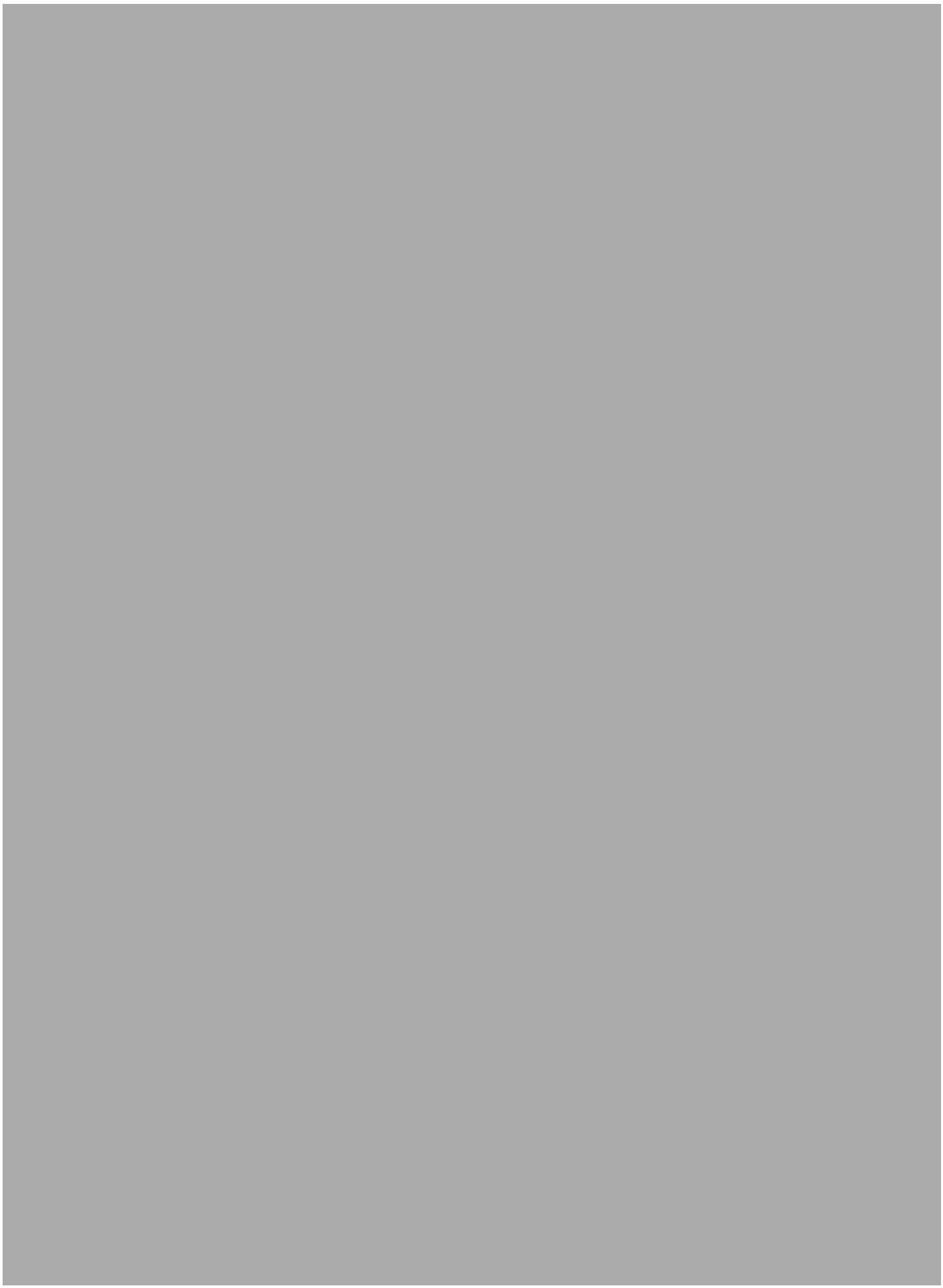

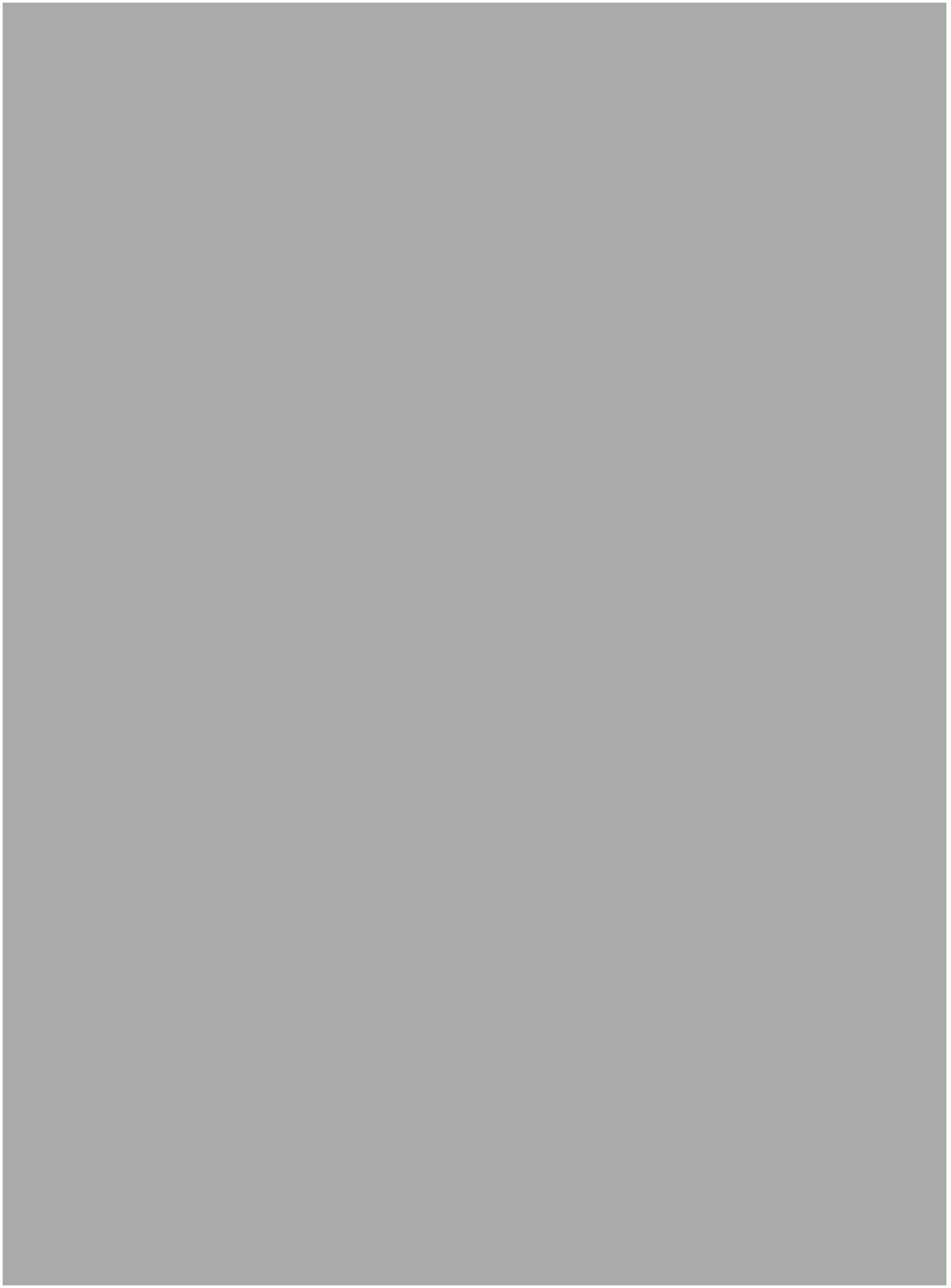

4. Synthesis, conductivity and structural aspects of $Nd_3Zr_2Li_{7-3x}Al_xO_{12}$

4.1 Publication

Title: *Synthesis, conductivity and structural aspects of* $Nd_3Zr_2Li_{7-3x}Al_xO_{12}$

Submitted: 16th Aug 2013

Accepted: 3rd Oct 2013

Information: *J. Mater. Chem.*, 2013, 1, 14013-14022

Times cited: 2 (20/09/2015)

Author contributions: M.A. Howard: The synthesis, structural characterisation and A.C. impedance studies of $Nd_3Zr_2Li_7O_{12}$ and $Nd_3Zr_2Al_{0.5}Li_{5.5}O_{12}$

O. Clemens: Guidance Neutron diffraction Rietveld refinement

K.S. Knight: Lead beam line scientist at HPRD Isis Rutherford Appleton Laboratories

P.A. Anderson: Supervision to M.A. Howard

S. Hafiz: Computational studies

P.M. Panchmatia: Lead supervisor to S. Hafiz

P.R. Slater: Lead supervisor to M.A. Howard

4.2 Highlights

- First reported synthesis, structure and Li ion conductivity of the new tetragonal garnet phase $Nd_3Zr_2Li_7O_{12}$. Like other tetragonal garnet systems, the Li is shown to be

ordered over the tetrahedral and distorted octahedral sites, and thus the Li ion conductivity is low.

- Al doping causes an improvement in the ionic conductivity of the parent material. The incorporation of Al leads to vacancies on the Li cation sublattice, and hence introduces disorder (the unit cell symmetry therefore undergoes a change from tetragonal to cubic).
- Neutron diffraction studies showed that the Al was introduced onto the ideal tetrahedral garnet site, consistent with computational modelling predictions.
- The role of moisture on the conductivity of these systems was also investigated, showing significant changes at low temperatures consistent with a protonic contribution in humid atmospheres due to the Li^+/H^+ exchange process.
- Complementary computational modelling studies are consistent with this favourable Li^+/H^+ exchange process.

Journal of Materials Chemistry A

RSC Publishing

PAPER

View Article Online
View Journal | View Issue

Cite this: J. Mater. Chem. A, 2013, 1, 14013

Synthesis, conductivity and structural aspects of $Nd_3Zr_2Li_{7-3x}Al_xO_{12}$

M. A. Howard,[a] O. Clemens,[a] K. S. Knight,[b] P. A. Anderson,[a] S. Hafiz,[c] P. M. Panchmatia[c] and P. R. Slater*[a]

Received 16th August 2013
Accepted 3rd October 2013

DOI: 10.1039/c3ta13252h

www.rsc.org/MaterialsA

In this paper we report the synthesis, structure and Li ion conductivity of a new tetragonal garnet phase $Nd_3Zr_2Li_7O_{12}$. In line with other tetragonal garnet systems, the Li is shown to be ordered in the tetrahedral and distorted octahedral sites, and the Li ion conductivity is consequently low. In an effort to improve the ionic conductivity of the parent material, we have also investigated Al doping to reduce the Li content, $Nd_3Zr_2Li_{5.5}Al_{0.5}O_{12}$, and hence introduce disorder on the Li sublattice. This was found to be successful leading to a change in the unit cell symmetry from tetragonal to cubic, and an enhanced Li ion conductivity. Neutron diffraction studies showed that the Al was introduced onto the ideal tetrahedral garnet site, a site preference also supported by the results of computer modelling studies. The effect of moisture on the conductivity of these systems was also examined, showing significant changes at low temperatures consistent with a protonic contribution in humid atmospheres. In line with these observations, computational modelling suggests favourable exchange energy for the Li^+/H^+ exchange process.

Introduction

The recent portable electronics boom has been driven by advances made in Li ion battery technology. This has led to a large amount of interest in the development of new materials with potential for use in such batteries. In terms of the electrolyte, there is growing interest in the development of new solid state electrolyte systems, which offer potential advantages in terms of cell safety and miniaturisation. In this respect, the lithium containing garnets have been attracting significant interest, following initial reports of high Li ion conductivity in such systems by Thangadurai *et al.*[1] These Li containing garnets are unusual in the sense that they show an excess of cations (Li) compared to the traditional garnet materials, which have ideal general formula $A_3B_2C_3O_{12}$ (where the A site is 8 coordinate, the B site is 6 coordinate and the C site is 4 coordinate). Thus in the Li ion conducting garnets, the conventional 8 coordinate (A) and 6 coordinate (B) sites are fully occupied, while partial occupancy of the tetrahedral (C) sites is observed, with additional Li in interstitial distorted octahedral sites not normally occupied in the garnet structure. Thus the stoichiometry of these Li ion conducting garnets can be given as $A_3B_2Li_{3+x}O_{12}$, where $0 \leq x \leq 4$ (ref. 1–14) (the value of x depends on the oxidation states of A and B). The initial work from Thangadurai and Weppner[15] on these systems reported the synthesis of the garnet materials $Li_5La_3M_2O_{12}$ (M = Nb, Ta) with high Li ion conductivities. The authors also reported that it is possible to increase the Li content by partial substitution of the La with K or alkaline earth cations, or by partial substitution of In for Nb.[16] To fully understand the Li ion conductivity of these garnet materials, it is important to have a detailed description of the structure. In this respect, initial structural studies using X-ray diffraction data led to different claims on the location of the Li sites.[17–19] This can be explained by the fact that Li has a weak X-ray scattering factor, which consequently severely hinders its effective location using X-ray diffraction. This problem can be solved through the use of neutron diffraction studies, with initial work in the area by Cussen *et al.* on $Li_5La_3M_2O_{12}$, showing that the space group was $Ia\bar{3}d$, with Li distributed over both the ideal tetrahedral garnet site and also interstitial distorted octahedral sites.[2] Cussen *et al.* also showed that the occupancy of the interstitial sites was only observed for Li contents per formula unit greater than 3, while in systems with ideal conventional garnet stoichiometry, such as $Li_3Ln_3Te_2O_{12}$ (Ln = rare earth), the Li was only present in the tetrahedral site. The Li ion conductivity for $Li_3Nd_3Te_2O_{12}$ system was consequently low ($\sigma_{total(600\ ^\circ C)} = 1 \times 10^{-5}$ S cm^{-1}), and it was concluded that occupancy of both tetrahedral and octahedral sites is the key to ensuring good Li ion conductivity.[14,20]

A number of recent modelling studies have investigated the conduction pathways within these garnet systems. These studies have suggested that the tetrahedral site plays a key role in the conduction pathway of the Li through the structure,[21–23]

[a]School of Chemistry, University of Birmingham, Birmingham, B15 2TT, UK. E-mail: p.r.slater@bham.ac.uk; Fax: +44 (0)121 4144403; Tel: +44 (0)121 4148906
[b]ISIS Facility, Rutherford Appleton Laboratory, Chilton, Oxon, UK
[c]School of Applied Sciences, University of Huddersfield, Huddersfield, HD1 3DH, UK

thus highlighting the need for both Li in the distorted octahedral sites, as well as vacancies in the tetrahedral sites.

Studies aimed at varying the Li content have shown that it is possible to prepare samples with Li contents up to 7 Li per formula unit. In such high Li content garnets, there have been reports of ordering of the Li ions, with 1 Li ion per formula unit located in the garnet tetrahedral site and the remaining 6 Li in the distorted octahedral (4 in the Li2 site, and 2 in the Li3 site) sites, not normally occupied in an ideal stoichiometric garnet.[9] The ordering of the Li atoms within the structure has been reported to be necessary to avoid short Li–Li repulsive interactions. This ordering leads to a tetragonal, rather than cubic, unit cell and a low Li ion conductivity.[9] However, differing results have been observed for the phase with composition $La_3Zr_2Li_7O_{12}$, with reports of both cubic and tetragonal cell symmetry for this system. The formation of cubic systems generally involves high synthesis temperatures (up to 1000 °C) with long heating times (over 12 h), which could give rise to Li_2O evaporation from the system leading to lower than 7 Li per formula unit and hence explaining the cubic unit cell symmetry. Other reports have suggested Al incorporation from reaction with crucibles occurs in these samples, due to the high synthesis temperature. In cases where cubic symmetry has been observed, high Li ionic conductivity was observed (*i.e.* $\sigma_{total(25\ °C)} \approx 10^{-4}$ S cm^{-1}), while tetragonal samples showed low conductivity due to the ordering of Li. In line with suggestions that Al incorporation from the crucible may be occurring, there have recently been a number of reports of doping on the Li site with Al, Ga, Ge, In and Si.[24–34] Al doping in the $La_3Zr_2Li_7O_{12}$ showed the highest conductivities, of the order of 10^{-4} S cm^{-1} at room temperature.

Another feature of these systems, that has begun to attract attention, is the possibility to partially exchange the Li^+ ions with protons.[35] While many of these studies have focused on exchange through immersion in water, or organic acids, there has been growing interest in the reactivity with moisture from the atmosphere.[36–39] Recently we reported that partial H^+/Li^+ exchange occurs in $La_3Zr_2Ga_{0.5}Li_{5.5}O_{12}$ on exposure to air, and that this partial exchange results in a reduction in grain boundary resistance, and hence an increase in the total conductivity at low temperatures.[29]

While there has been considerable work on doping within $La_3Zr_2Li_7O_{12}$, there have been no reports on the variation of the rare earth cation. To this end, we have examined the effect of varying the rare earth size, and this work showed that it was possible to synthesise $Nd_3Zr_2Li_7O_{12}$, while for smaller rare earths, a garnet phase did not form. In this paper we report the synthesis, structure and ionic conductivity of this new tetragonal phase $Nd_3Zr_2Li_7O_{12}$. In an effort to improve the ionic conductivity, we have also investigated Al doping to reduce Li content and hence change the unit cell symmetry from tetragonal to cubic. The characterisation of this Al doped material is also reported, and we also investigate the effect of exposure of the samples to moisture. The experimental work is supported by computational modelling studies into the most favourable dopant position and the energetics behind H^+/Li^+ exchange, the first such studies on these garnet systems.

Experimental

$Nd_3Zr_2Li_7O_{12}$ and $Nd_3Zr_2Li_{5.5}Al_{0.5}O_{12}$ were prepared *via* solid state reactions as follows. Stoichiometric amounts of Nd_2O_3 (99.99% purity), ZrO_2 (99% purity), Al_2O_3 (99% purity), Li_2CO_3 (99% purity) powders (with a 10% molar excess of Li_2CO_3, to account for Li_2O loss by chemical transport with traces of water yielding volatile LiOH) were ground together in an agate pestle and mortar until a homogeneous powder was achieved. The powder was transferred into an alumina crucible and then heated at 600 °C for 2 hours. The temperature was then increased to 800 °C for 12 hours. The heated powder was removed from the furnace and reground with a further 10% molar excess Li_2CO_3 added. The powder was then pressed into a pellet and the pellet was heated at temperatures of 850 °C for 12 hours for $Nd_3Zr_2Li_7O_{12}$, and 1000 °C for 4 hours for $Nd_3Zr_2Li_{5.5}Al_{0.5}O_{12}$. The garnet pellets were placed on zirconia pellets to avoid any Al incorporation from the crucible at the elevated reaction temperature. X-ray diffraction (Bruker D8 diffractometer with Cu Kα_1 radiation) was used to determine phase purity.

For conductivity measurements, pellets were pressed and heated at different temperatures and times (up 1200 °C for 1–12 hours, on zirconia pellets to avoid Al incorporation) to examine the effect of sintering temperature on the conductivity. It was found that heating for 4 hours at 1000 °C gave a density of ~82% of the crystallographic density. Higher temperature heat treatment led to the formation of significant perovskite-type impurities, attributed to Li loss, and so the sintering temperature was limited to 1000 °C. Ag electrodes were attached to the pellet using Ag paste and the pellet fired again, at 120 °C for 30 min, to give a good electrical contact between the electrode and sample. Conductivity measurements were carried out using A.C. impedance spectroscopy (Hewlett Packard 4192A Impedance Analyser) in the range from 0.1 to 10^3 kHz. Conductivity measurements were performed in wet and dry N_2 to elucidate any changes in the conductivity on exposure to moisture. In order to confirm that the conductivity changes in wet atmospheres were not simply due to surface conduction along the edges of the pellet, impedance spectra were also collected on a pellet where the lateral pellet surfaces were covered with silicon-based grease (Dow corning high vacuum grease). In these experiments electrodes were applied to the pellet with the inner circle removed to create a ring-shaped electrode (shown in Fig. 1). This experimental approach allows for water incorporation into the sample, while preventing surface conduction: such an approach was demonstrated previously by Mather *et al.* in the study of proton conduction in nano-crystalline YSZ,[40] where the authors showed that in this case the enhanced conductivity in wet atmosphere was due to surface conduction rather than bulk effects. Impedance data were analysed using ZView software[41] by fitting the data to appropriate equivalent circuits.

Neutron diffraction data for $Nd_3Zr_2Li_7O_{12}$ and $Nd_3Zr_2Li_{5.5}Al_{0.5}O_{12}$ were collected on the HRPD diffractometer, ISIS, Rutherford Appleton Laboratory. All structure refinements used the Topas suite of Rietveld refinement software.[42]

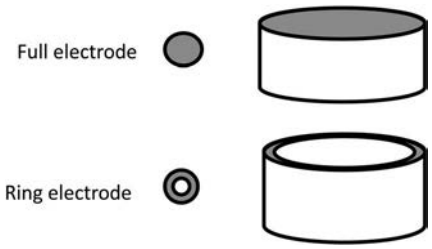

Fig. 1 Diagram illustrating ring-shaped electrode and standard electrode arrangements for conductivity measurements.

Computational methods

In this study, well established atomistic modelling methods embodied in the GULP code[44] have been used, and these methods have been reviewed elsewhere.[45,46] The calculations are based on the Born model for polar solids where the interactions between ions are represented in terms of a long-range Coulombic term plus an analytical function representing short-range repulsive and van der Waals interactions. For this study, the short-range interactions were modelled using the Buckingham potential:

$$V_{ij}(r) = A_{ij}\exp\left(\frac{-r}{\rho_{ij}}\right) - \frac{c_{ij}}{r^6} \quad (1)$$

where r is the interatomic distance and A, ρ and C are empirically derived parameters. Charged defects will polarise nearby ions in the lattice and therefore, to calculate the defect energies accurately, we included the electronic polarisability in the model, which is incorporated *via* the shell model.[47] Point defects were modelled using the Mott–Littleton approach, in which a defect is introduced into the energy-minimised lattice, and the surrounding ions partitioned into two regions.[47,48] An inner sphere of ions immediately surrounding the point defect (region 1) is then relaxed explicitly whilst the crystal bulk (region 2) is treated by computationally less expensive quasi-continuum methods.

As with previous modelling studies on protons in perovskite oxides[49] and silicate minerals[50,51] the OH interaction was treated using an attractive Morse potential (with Coulomb subtraction):

$$V(r) - D\{1 - \exp[-\beta(r - r_0)]\}^2 \quad (2)$$

Table 1 Interatomic Buckingham potentials and shell model parameters for $Nd_3Zr_2Li_7O_{12}$ and $Nd_3Zr_2Li_{5.5}Al_{0.5}O_{12}$

Interaction	A (eV)	ρ (Å)	C (eV Å^6)	γ (e)	k (eV Å^{-2})
$Li^+\cdots O^{2-}$	292.3000	0.3472	0.0000	1.00	99 999
$Zr^{4+}\cdots O^{2-}$	985.8690	0.3670	0.0000	1.35	169.92
$Nd^{3+}\cdots O^{2-}$	1995.2000	0.3430	22.5900	3.00	99 999
$Al^{3+}\cdots O^{2-}$	1142.6775	0.2991	0.0000	3.00	99 999
$O^{2-}\cdots O^{2-}$	22764.30	0.1490	43.0000	−2.86	74.92
$H^+\cdots O^{2-a}$	311.9700	0.2500	0.0000	—	—

[a] Morse intra-molecular parameters: D = 7.0525 eV; β = 2.1986 Å^{-1}; r_o = 0.9485 Å; charge O core: −1.4263, H core: +0.4263.

using parameters (listed in Table 1) developed from *ab initio* quantum mechanical cluster calculations,[50] with a point charge representation of the surrounding lattice. The dipole moment of the OH group was simulated by placing charges of −1.4263 and +0.4263 on the O and H species, respectively (overall charge −1.00) in accordance with this study. Additional Buckingham parameters were employed to simulate the interaction of the lattice oxygen atoms with the hydroxyl unit.[50,51] Lattice energies for the binary oxides required in the doping studies were calculated using the parameters listed in Table 1, whilst a correction term was added to account for the change in chemical potential energy due to the formation of LiOH and Li_2CO_3 from Li_2O using the following equations:

$$Li_2O + H_2O \rightarrow 2LiOH \quad (3)$$

$$Li_2O + CO_2 \rightarrow Li_2CO_3 \quad (4)$$

The correction term was calculated using experimental enthalpy of formation at 300 K.[52,53]

Results

Structural studies

X-ray diffraction patterns showed that the $Nd_3Zr_2Li_7O_{12}$ garnet phase was successfully prepared, with peak splitting indicative of a tetragonal unit cell. In contrast the Al doped phase, $Nd_3Zr_2Li_{5.5}Al_{0.5}O_{12}$, showed a simpler X-ray diffraction pattern, consistent with a cubic unit cell (Fig. 2). This change in symmetry is an indication that Al has been successfully doped onto one of the 3 Li sites, leading to the creation of 2 Li^+ vacancies for each Al^{3+} introduced (one Al^{3+} will replace three Li^+), and hence allowing the introduction of disorder and the change in the symmetry to a cubic unit cell.

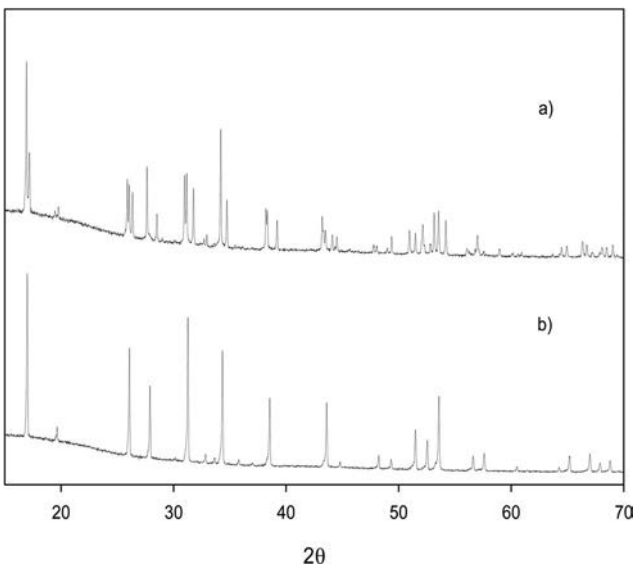

Fig. 2 X-ray diffraction patterns for (a) $Nd_3Zr_2Li_7O_{12}$ and (b) $Nd_3Zr_2Li_{5.5}Al_{0.5}O_{12}$.

Table 2 Structural parameters for $Nd_3Zr_2Li_7O_{12}$ from neutron powder diffraction data[a]

Atom	Site	*x*	*y*	*z*	Fractional occupancy
Nd1	8b	0	1/4	1/8	1
Nd2	16e	0.1271(1)	0	1/4	1
Zr	16c	0	0	0	1
Li1	8a	0	1/4	3/8	1
Li2	16f	0.1819(4)	0.4319(4)	1/8	1
Li3	32g	0.0803(4)	0.0885(4)	0.8042(4)	1
O1	32g	0.2773(1)	0.0986(1)	0.1949(1)	1
O2	32g	0.1945(1)	0.2834(1)	0.0971(1)	1
O3	32g	0.1012(1)	0.1942(1)	0.2828(1)	1

[a] Tetragonal, $I4_1/acd$, $a = 12.94711(9)$, $c = 12.5512(1)$ Å, $B_{iso,eq} = 0.25(1)$, $R_{wp} = 3.580$, $R_{exp} = 1.152$, GOF = 3.107.

Neutron diffraction data were analysed to determine the location of the Al in $Nd_3Zr_2Li_{5.5}Al_{0.5}O_{12}$, as well as the Li positions and distribution in both this and the parent $Nd_3Zr_2Li_7O_{12}$ phase. For the latter, the structure of the tetragonal garnet phase $La_3Zr_2Li_7O_{12}$ (ref. 43) with space group $I4_1/acd$, was used as an initial starting model (where La ions were replaced by Nd ions). In the refinement an empirical absorption correction was included to account for absorption from the Li and Nd in the samples (this was included in both refinements). The structure refinement confirmed the tetragonal symmetry, with cell parameters of $a = 12.9471(1)$ Å, $c = 12.5511(1)$ Å. When comparing the unit cell parameters of previously reported tetragonal $La_3Zr_2Li_7O_{12}$ with tetragonal $Nd_3Zr_2Li_7O_{12}$, a decrease in unit cell size is observed with the Nd sample, which is as expected due to the smaller size of Nd^{3+} (1.109 Å, 8 coordinate) compared to La^{3+} (1.160 Å, 8 coordinate).[54] Atomic positions were refined for $Nd_3Zr_2Li_7O_{12}$ and gave sensible values with low positional errors for the respective sites. Li occupancies were initially set at full occupancy for each site. Refinement of these Li site occupancies led to negligible change from full occupancy. The values were therefore fixed at full occupancy for the final refinement. Refinement of the atomic displacement parameters led to values with large errors, and so an overall parameter for the phase was refined. Some extra peaks were present in the neutron diffraction pattern, which could be attributed to Li_2CO_3 from the excess used in the synthesis, and the vanadium sample can used in the experiment. These were included in the refinement as secondary phases. The final structural parameters and bond distances are presented in Tables 2 and 3, with the observed, calculated and difference neutron diffraction profiles presented in Fig. 3.

In the Rietveld refinement of the structure of $Nd_3Zr_2Al_{0.5}Li_{5.5}O_{12}$, the structural model for $La_3Nb_2Li_5O_{12}$ with space group $Ia\bar{3}d$ (ref. 2) was used as a starting point, again with the replacement of La by Nd. This confirmed the cubic cell with unit cell parameters of $a = 12.8158(1)$ Å. In the first instance, it was assumed that only Li was present on the Li sites, and the occupancies of these sites were allowed to vary in the refinement. From this refinement, the occupancy of the Li1 (24d) (ideal tetrahedral) site showed a value close to zero. As Li has a negative scattering length and Al has a positive scattering length this was a good indication that Al had been successfully doped onto this site. The Al on the Li1 (24d) site was therefore added to the refinement and the occupancy of the Al was fixed at the value (1/6) expected from the initial sample composition. The occupancy of this site by Al was supported by the modelling

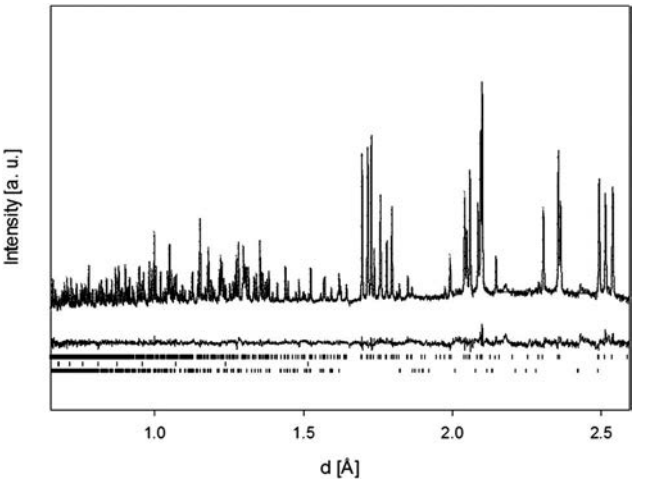

Fig. 3 The observed, calculated and difference neutron diffraction data profiles for $Nd_3Zr_2Li_7O_{12}$ (lower tick marks Li_2CO_3, middle tick marks vanadium sample can, upper tick marks $Nd_3Zr_2Li_7O_{12}$).

Table 3 Selected bond distances for $Nd_3Zr_2Li_7O_{12}$ from neutron diffraction studies, along with calculated mean bond lengths from modelling studies

Bond	Experimental bond distance	Calculated mean bond distance	Bond	Experimental bond distance	Calculated mean bond distance
Nd1–O1 [x2]	2.426(2)	2.433	Li2–O2 [x2]	1.968(6)	1.974
Nd1–O1 [x2]	2.497(2)	2.468	Li2–O1 [x2]	2.349(2)	2.342
Nd1–O2 [x2]	2.518(2)	2.536	Li2–O1 [x2]	2.379(7)	2.552
Nd1–O3 [x2]	2.568(2)	2.621	Li3–O1	1.852(6)	1.848
Nd2–O3 [x4]	2.484(2)	2.488	Li3–O2	2.035(7)	2.055
Nd2–O2 [x4]	2.580(2)	2.643	Li3–O2	2.049(7)	2.159
Zr–O2 [x2]	2.094(2)	1.975	Li3–O3	2.195(6)	2.263
Zr–O3 [x2]	2.102(2)	1.997	Li3–O3	2.719(6)	2.749
Zr–O1 [x2]	2.107(2)	2.011	Li3–O3	2.834(7)	2.919
Li1–O3 [x4]	1.889(2)	1.964			

Table 4 Structural parameters for $Nd_3Zr_2Li_{5.5}Al_{0.5}O_{12}$ from neutron powder diffraction data[a]

Atom	Site	x	y	z	Fractional occupancy
Nd1	24c	1/8	0	1/4	1
Zr1	16a	0	0	0	1
Li1	24d	3/8	0	1/4	0.35(2)
Li2	96h	0.103(1)	0.687(1)	0.574(1)	0.368(5)
Al1	24d	3/8	0	1/4	1/6
O1	96h	0.2808(1)	0.0984(1)	0.1945(1)	1

[a] Cubic, $Ia\bar{3}d$, $a = 12.8158(1)$ Å, $B_{iso,eq} = 0.32(2)$, $R_{wp} = 4.828$, $R_{exp} = 1.527$, GOF = 3.162.

studies (see next section). The Li occupancies were then constrained to equal 5.5 Li atoms per formula unit, again as expected from the sample stoichiometry. The fractional Li occupancies were then refined, giving the tetrahedral Li1 (24d) site a Li occupancy of 0.35(2) and the distorted octahedral site Li2 (96h) an occupancy of 0.368(5). Refinement of the Li3 (highly distorted octahedral) site (found to be occupied in other Li containing garnets) led to zero occupancy of this site, and so this site was removed from the refinement. As with the refinement of the structure of tetragonal $Nd_3Zr_2Li_7O_{12}$, an overall atomic displacement parameter was refined.

As before, extra peaks were observed due to the vanadium sample can which was included as a secondary phase. Final structural parameters and bond distances are presented in Tables 4 and 5. The observed, calculated and difference neutron diffraction profiles are presented in Fig. 4.

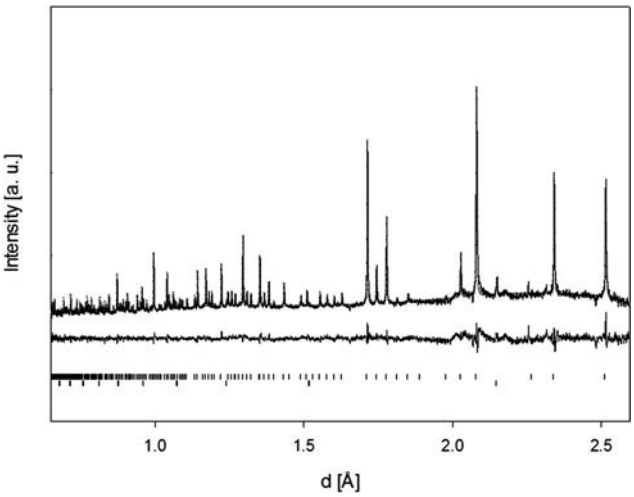

Fig. 4 The observed, calculated and difference neutron diffraction data profiles for $Nd_3Zr_2Li_{5.5}Al_{0.5}O_{12}$ (lower tick marks vanadium sample can, upper tick marks $Nd_3Zr_2Li_{5.5}Al_{0.5}O_{12}$).

Modelling studies

The interatomic potentials used for the modelling studies of $Nd_3Zr_2Li_7O_{12}$ and $Nd_3Zr_2Li_{5.5}Al_{0.5}O_{12}$ are listed in Table 1, while Table 6 shows the structural reproduction of the calculated structure, illustrating a fit to within 1% of the observed cell parameters. This represents excellent agreement especially since the modelling of these structures is not trivial given their complex nature, with Li present in both the tetrahedral and octahedral coordination sites. Fig. 5(a) and (b) show the schematic representations of both the tetragonal and cubic structures. Tables 3 and 5 list the experimental and mean calculated bond lengths for $Nd_3Zr_2Li_7O_{12}$ and $Nd_3Zr_2Al_{0.5}Li_{5.5}O_{12}$ respectively. Following the successful reproduction of the structures, defect modelling and dopant solution energies were calculated, the latter to include both trivalent cation doping on the Li sites, and H^+/Li^+ exchange.

The defect modelling suggests the most favourable intrinsic defect to be the Li Frenkel defect, see Table 7. The dopant studies in $Nd_3Zr_2Li_7O_{12}$ suggest the Li1 (tetrahedral) site to be the most favoured site for Al doping in accord with the diffraction studies. The local structural analysis from

Table 6 Structural comparisons (experimental and calculated) for (a) $Nd_3Zr_2Li_7O_{12}$ and (b) $Nd_3Zr_2Li_{5.5}Al_{0.5}O_{12}$

Parameter	Experimental	Calculated	Difference (% diff.)
(a) $Nd_3Zr_2Li_7O_{12}$			
a/Å	12.9471	12.9674	0.01993(0.15)
b/Å	12.9471	12.9674	0.0199(0.15)
c/Å	12.5512	12.5864	0.0353(0.28)
$\alpha = \beta = \gamma$	90.0	90.0	0.0(0.00)
(b) $Nd_3Zr_2Li_{5.5}Al_{0.5}O_{12}$			
a/Å	12.8158	12.8246	0.0088(0.07)
b/Å	12.8158	12.8179	0.0021(0.02)
c/Å	12.8158	12.8126	−0.0032(−0.03)
$\alpha = \beta = \gamma$	90.0	90.0	0.0(0.00)

Table 5 Selected bond distances for $Nd_3Zr_2Li_{5.5}Al_{0.5}O_{12}$ from neutron diffraction studies, along with calculated mean bond lengths from modelling studies

Bond	Experimental bond distance	Calculated mean bond distance	Bond	Bond distance	Calculated mean bond distance
Nd–O [x4]	2.469(2)	2.425	Li2–O	1.875(17)	1.937
Nd–O [x4]	2.545(2)	2.549	Li2–O	2.128(18)	2.020
Zr–O [x6]	2.110(2)	2.073	Li2–O	2.144(16)	2.109
Li1–O [x4]	1.881(2)	1.926	Li2–O	2.194(18)	2.219
Al–O[x4]	1.881(2)	1.662	Li2–O	2.518(17)	2.435
			Li2–O	2.657(16)	2.659

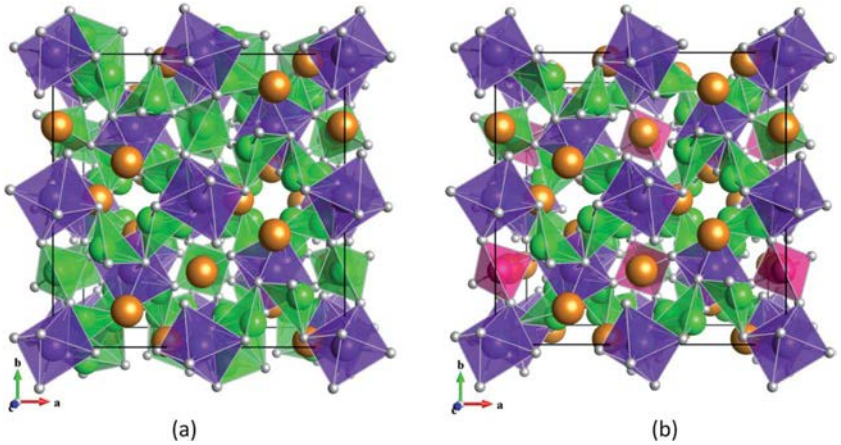

Fig. 5 Schematic representation of the structures of (a) $Nd_3Zr_2Li_7O_{12}$ and (b) $Nd_3Zr_2Li_{5.5}Al_{0.5}O_{12}$. Key: Nd – orange; Zr – purple; Li – green; O – grey; Al – pink.

the simulations indicates shorter Al–O bond lengths compared to the Li–O equivalents in the $Nd_3Zr_2Li_7O_{12}$. The Al is closer to its nearest neighbour Li3 (octahedral site) by 0.25 Å than the Li1–Li3 distance in the non-doped tetragonal structure. This might indicate why the Li3 site is not occupied by Li for the Al doped cubic sample, since this would lead to unfavourable strong cation–cation repulsion. The results also show that the nearest neighbour Li, that used to be in the octahedral coordination site, has a tendency to displace to achieve LiO_4 tetrahedral coordination, see Fig. 6(a). The next nearest lithium however remains octahedrally coordinated suggesting no long-range distortions. A similar situation is also observed for the $Nd_3Zr_2Li_{5.5}Al_{0.5}O_{12}$ phase. From these calculations Al doping on the Li sites is predicted to be favourable in accord with experimental observations.

In determining the trivalent dopant solution energies, three different mechanisms were investigated (equations shown in Table 8), where Li_2O, Li_2CO_3 and LiOH were possible by-products of the doping studies. Table 8 lists the most favourable calculated solution energies for doping a variety of trivalent atoms (Al, Ga, In) in place of Li. These M^{3+} dopants were predicted to favour the tetrahedral Li1 site. The modelling also implies that if CO_2 is present, then the formation of Li_2CO_3 is most favourable. The results therefore suggests that the atmosphere (*i.e.* partial pressures of H_2O, CO_2) used in the synthesis may have an effect on the incorporation of dopants in these garnet systems. In addition to the analysis of the incorporation of trivalent dopants, modelling of Li^+/H^+ exchange has also been investigated. Table 8 lists the two mechanisms considered for proton-exchange. The solution energies for proton exchange imply that the formation of Li_2CO_3 is more favourable than the formation of LiOH as a by-product, suggesting again that the atmosphere, which the sample is exposed to, may have a significant effect on this process. Local structure analysis of the proton environment suggests that the H^+ prefers to exchange with the Li on the octahedral site causing significant distortions as it forms a typical O–H bond (0.978 Å) with the nearest neighbour oxygen (illustrated in Fig. 6(b)). Neighbouring octahedral and tetrahedral Li sites are also slightly distorted. Local atomic distances are shown in Fig. 6(b).

Conductivity studies

Room temperature A.C. impedance measurements of $Nd_3Zr_2Li_7O_{12}$ in wet and dry N_2 recorded a very high resistance at the limit of the instrument capability. At higher temperatures, an increase in the conductivity was observed, but the conductivity remained low consistent with the ordered nature of the Li ion distribution in this phase. Arrhenius plots comparing the conductivity of the sample in wet and dry N_2 are presented in Fig. 7. A small improvement in the bulk conductivity was observed in wet N_2 experiments in the temperature range 100–400 °C. Activation energies were calculated to be 0.55 eV in wet N_2 atmosphere and 0.66 eV for the dry N_2 experiments. This improvement in the conductivity can be attributed to the effect of H^+/Li^+ exchange, which would lead to a number of consequences. The introduction of protons may lead to a protonic contribution to the conductivity, while the

Table 7 Intrinsic defects

$Nd_3Zr_2Li_7O_{12}$

Defects	Defect equations	Energy (eV)
Li Frenkel	$Li_{Li}^{\times} \rightarrow V'_{Li} + Li_i^{\cdot}$	0.78
O Frenkel	$O_O^{\times} \rightarrow V_O^{\cdot\cdot} + O_i''$	6.52
Schottky	$2Zr_{Zr}^{\times} + 12O_O^{\times} + 3Nd_{Nd}^{\times} + 7Li_{Li}^{\times} \rightarrow 2V''''_{Zr} + 12V_O^{\cdot\cdot} + 3V'''_{Nd} + 7V'_{Li} + Nd_3Li_7Zr_2O_{12}$	31.69

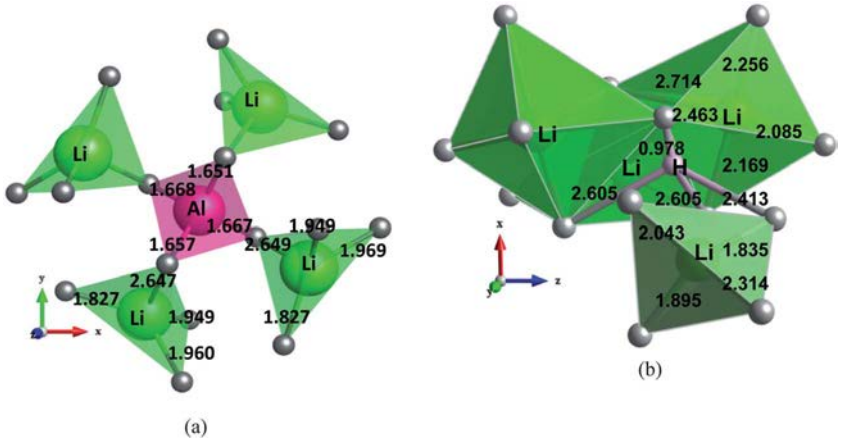

Fig. 6 Local structure of the (a) Al site where the most favourable doping site is the Li tetrahedral site, and (b) H site where the most favourable doping site was the Li octahedral site. All the distances are in ångströms. Key: Li – green and blue; O – grey; Al – pink; H – white.

Table 8 M^{3+} and H^+ doping mechanism equations and energies

$M_2O_3 + 6Li_{Li}^{\times} \rightarrow 2M_{Li}^{\cdot\cdot} + 4V_{Li}' + 3Li_2O$	(1)
$M_2O_3 + 6Li_{Li}^{\times} + 3CO_2 \rightarrow 2M_{Li}^{\cdot\cdot} + 4V_{Li}' + 3Li_2CO_3$	(2)
$M_2O_3 + 6Li_{Li}^{\times} + 3H_2O \rightarrow 2M_{Li}^{\cdot\cdot} + 4V_{Li}' + 6LiOH$	(3)
$H_2O + Li_{Li}^{\times} \rightarrow H_{Li}^{\times} + LiOH$	(4)
$H_2O + CO_2 + 2Li_{Li}^{\times} \rightarrow 2H_{Li}^{\times} + Li_2CO_3$	(5)

$Nd_3Zr_2Li_7O_{12}$

Dopant	Bond lengths	Energy (eV)
Al–O x4	1.662	0.113 (eqn (1))
		−2.172 (eqn (2))
		−1.890 (eqn (3))
Ga–O x4	1.854	3.505 (eqn (1))
		1.220 (eqn (2))
		1.501 (eqn (3))
In–O x4	1.980	3.810 (eqn (1))
		1.525 (eqn (2))
		1.807 (eqn (3))
H–O	0.978	−0.977 (eqn (4))
		−2.703 (eqn (5))

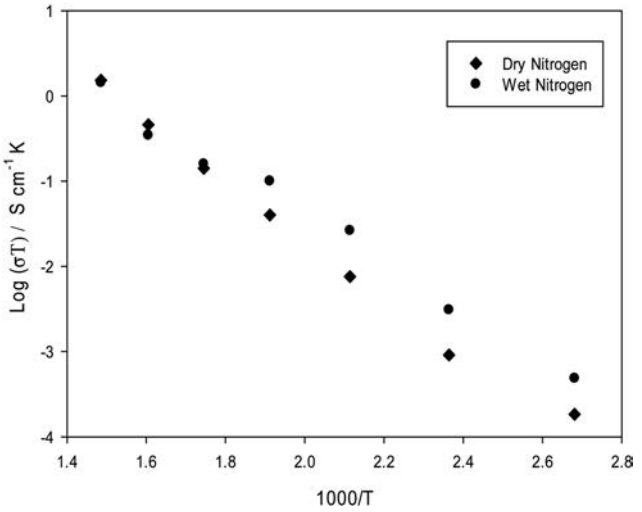

Fig. 7 Arrhenius plots of bulk conductivity for $Nd_3Zr_2Li_7O_{12}$ in wet N_2, and dry N_2, showing an enhancement for the latter at low temperatures.

creation of Li ion vacancies may increase the Li ion conductivity. The H^+/Li^+ exchange may also lead to a partial suppression of the local Li ordering, which could also account for the improved conductivity. In this respect, a recent study by Larraz *et al.* has shown that proton incorporation in the related $La_3Zr_2Li_7O_{12}$ can lead to a change from an ordered tetragonal system to a disordered cubic system.[55]

Room temperature A.C. impedance measurements for $Nd_3Zr_2Al_{0.5}Li_{5.5}O_{12}$ showed significantly higher conductivities, as expected from the introduction of Al lowering the Li content, and hence leading to disorder on the Li sublattice. Under a wet N_2 atmosphere, the impedance spectrum at RT showed a single semi-circle which was characteristic of a bulk response (Fig. 8). The conductivity was calculated to be $\sigma_{bulk(25\ ^\circ C)} = 3.9 \times 10^{-5}$ S cm^{-1}, comparable to values previously reported for other cubic Li ion conducting garnets. The activation energy was calculated to be 0.56 eV between 100 and 400 °C. For the dry N_2 atmosphere, the room temperature data showed a larger bulk semicircle, along with the beginning of a second feature attributed to a grain boundary response (Fig. 9). The bulk conductivity was calculated to be $\sigma_{bulk(25\ ^\circ C)} = 9.1 \times 10^{-6}$ S cm^{-1}, indicating a lower bulk conductivity than in the wet atmosphere. At higher temperatures, both the data in dry and wet N_2 showed the presence of two semicircles consistent with bulk and grain boundary components. Equivalent circuits were used to fit these data and are presented in Fig. 10 and 11 for the 100 °C data set. The activation energy was calculated to be 0.38 eV in the dry N_2 atmosphere between 100 and 400 °C, which is slightly lower than for the wet N_2 data.

Arrhenius plots comparing the conductivities in wet N_2 and dry N_2 are shown in Fig. 12. These data show interesting variations. In particular, at temperatures below 100 °C, the bulk conductivity is lower in dry N_2 than in wet N_2, suggesting an additional protonic contribution in the latter. However, at

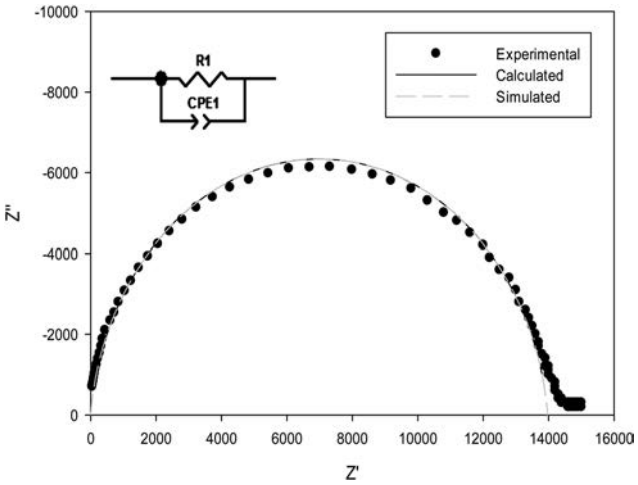

Fig. 8 Observed (circle), calculated (black line), simulated (grey dashed line) Nyquist plot at room temperature in wet N_2 for $Nd_3Zr_2Li_{5.5}Al_{0.5}O_{12}$.

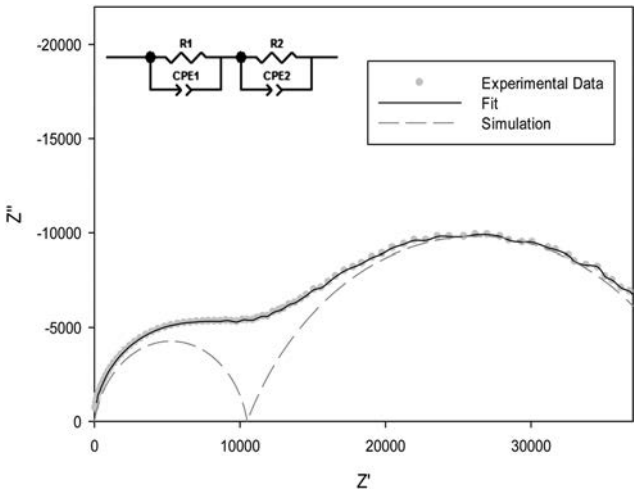

Fig. 10 Experimental (circle), fit (grey line) and simulated (dashed line) profiles for wet N_2 A.C. impedance measurements at 100 °C for $Nd_3Zr_2Li_{5.5}Al_{0.5}O_{12}$.

100 °C and above, the conductivity in dry N_2 becomes higher. The higher bulk conductivity at the temperatures above 100 °C in dry N_2 is consistent with prior studies of $La_3Zr_2Ga_{0.5}Li_{5.5}O_{12}$, where the effect of H^+/Li^+ exchange was to reduce the bulk conductivity, while enhancing the grain boundary conductivity. A similar enhancement of the grain boundary conductivity was observed for $Nd_3Zr_2Al_{0.5}Li_{5.5}O_{12}$. In this case, however, there also appears to be an enhancement in the bulk conductivity below 100 °C. It was thought that this may be related to surface conduction; recent work suggesting high room temperature proton conductivity in nano-crystalline yttria-stabilised zirconia[40] has been similarly identified as being due to surface conduction. In order to determine whether surface conduction was also a factor in the case of these garnet materials, A.C. impedance measurements were recorded on pellets, which had been coated with silicone grease on the lateral surface (as described in the experimental section; see Fig. 1). In wet N_2, the impedance spectrum (Fig. 13) showed a similar reduced bulk resistance compared to the dry N_2 experiment. (Note: the increase in resistance compared to the initial wet N_2 data set is due to the fact that in this experiment, the inner circle of Ag has been removed to create a ring-shaped electrode, leading to a reduction in the electrode area.) The fact that the conductivity is still enhanced in this experiment could be taken suggest that there is bulk rather than surface proton conduction, although given the fact that the pellet was only ~82% dense, it is not possible to discount water incorporation into the pores and resultant surface conduction along grains (as noted in the experimental section, attempts to increase the pellet density by higher temperature sintering led to significant Li loss). Possible support for the enhancement being due to bulk conduction is, however, provided by recent results by Larraz *et al.*, who have reported the presence of bulk water at low temperatures in garnet Li ion conductors.[55] Such water insertion would increase

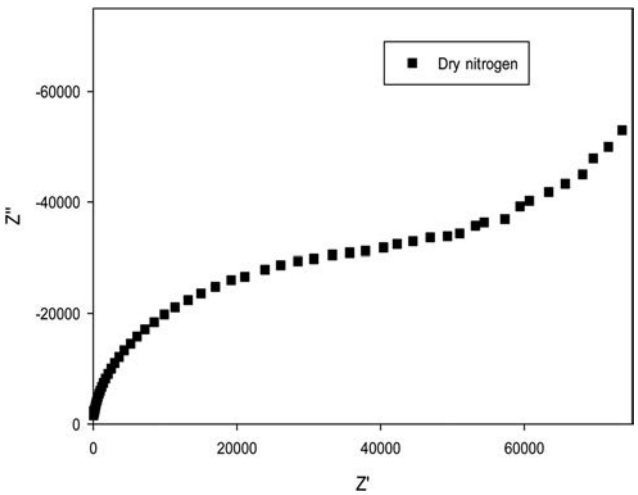

Fig. 9 Observed Nyquist plot at room temperature in dry N_2 for $Nd_3Zr_2Li_{5.5}Al_{0.5}O_{12}$.

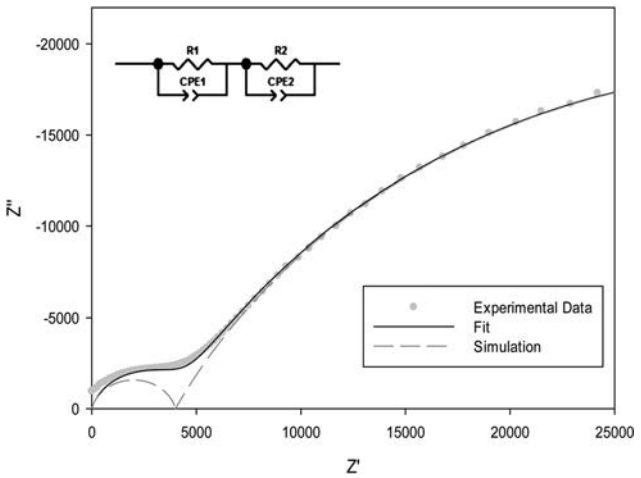

Fig. 11 Experimental (circle), fit (grey line) and simulated (dashed line) profiles for dry N_2 A.C. impedance measurements at 100 °C for $Nd_3Zr_2Li_{5.5}Al_{0.5}O_{12}$.

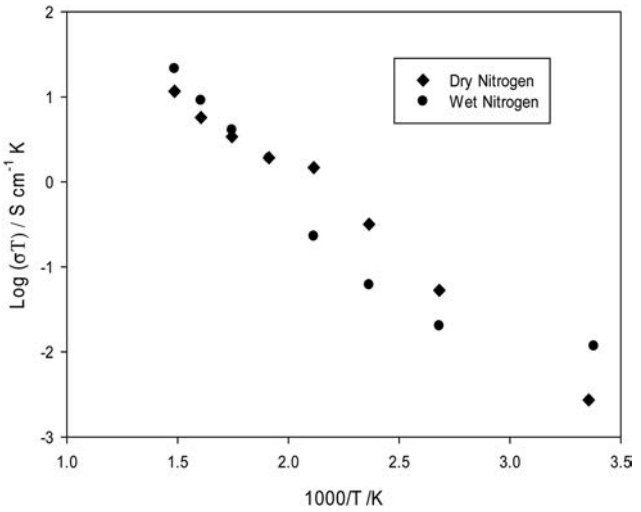

Fig. 12 Arrhenius plots of bulk conductivity for $Nd_3Zr_2Al_{0.5}Li_{5.5}O_{12}$ in wet N_2, and dry N_2.

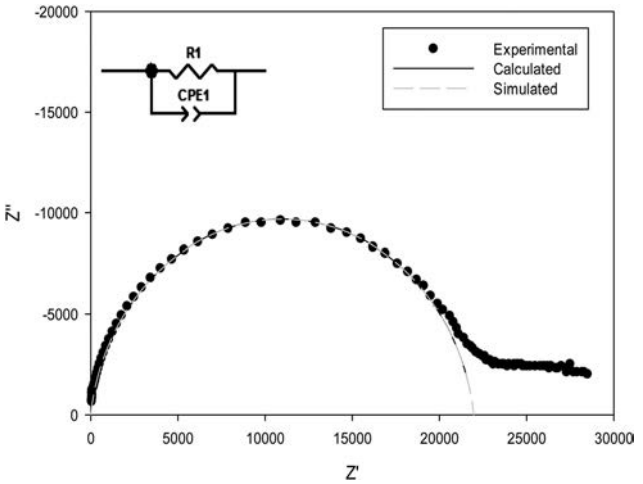

Fig. 13 Observed (circle), calculated (black line), simulated (grey dashed line) Nyquist plot for ring shaped electrode experiment at room temperature in wet N_2 for $Nd_3Zr_2Li_{5.5}Al_{0.5}O_{12}$.

the H content and so may enhance the protonic contribution to conduction leading to the observed conductivity enhancement. The results therefore suggest further work on the effect of water on these garnet materials is warranted. In particular there is a need for the preparation and analysis of dense pellets through low temperature/short heating time routes, *e.g.* spark plasma sintering, to avoid Li loss.

Conclusions

We have shown the successful synthesis of the tetragonal garnet phase $Nd_3Zr_2Li_7O_{12}$ for the first time. We have also shown that it is possible to change the unit cell symmetry to cubic by doping on the Li sites with Al. Neutron diffraction studies were used to determine that Al had been doped onto the ideal garnet tetrahedral site, also supported by the results of modelling studies. Conductivity measurements of the tetragonal $Nd_3Zr_2Li_7O_{12}$ sample showed low conductivity due to Li ordering. Doping with Al improved the conductivity *via* creating defects within the structure. It was shown that, in both samples, moisture has a significant effect on the conductivity. The elimination of the grain boundary component in wet atmospheres is especially significant, with regard to the total conductivity, and shows that care should be taken to ensure elimination of water in assessing the room temperature Li ion conductivity of these systems. The modelling studies further support the favourability of the Li^+/H^+ exchange process, with the favoured H^+ site being the distorted octahedral Li site. The modelling studies also suggest that the atmosphere may also have an effect on the degree of exchange.

Acknowledgements

We would like to thank the Engineering and Physical Sciences Research Council (EPSRC) and the University of Birmingham for financial support (studentship for MH). Neutron diffraction beamtime at ISIS, Rutherford Appleton Lab, was provided by the Science and Technology Facilities Council (STFC). The Bruker D8 used in this research were obtained through the Science City Advanced Materials project, with support from Advantage West Midlands (AWM) and part funded by the European Regional Development Fund (ERDF). O. Clemens would like to thank the German Academic Exchange Service (DAAD) for providing a postdoctoral fellowship. P. M. Panchmatia would like to thank Dr David J. Cooke, University of Huddersfield, for useful discussions on the doping mechanisms. P. M. P. would like to acknowledge membership of the UK's HPC Materials Chemistry Consortium, which is funded by EPSRC (Grant No. EP/F067496) and the use of the University of Huddersfield Queensgate Grid in carrying out this work.

References

1 V. Thangadurai, S. Adams and W. Weppner, *Chem. Mater.*, 2004, **16**, 2998.
2 E. J. Cussen, *Chem. Commun.*, 2006, 412.
3 M. P. O'Callaghan and E. J. Cussen, *Chem. Commun.*, 2007, 2048.
4 M. P. O'Callaghan, D. R. Lynham, E. J. Cussen and G. Z. Chen, *Chem. Mater.*, 2006, **18**, 4681.
5 J. Percival and P. R. Slater, *Solid State Commun.*, 2007, **142**, 355.
6 J. Percival, D. Apperley and P. R. Slater, *Solid State Ionics*, 2008, **179**, 1693.
7 J. Percival, E. Kendrick and P. R. Slater, *Solid State Ionics*, 2008, **179**, 1666.
8 J. Percival, E. Kendrick and P. R. Slater, *Mater. Res. Bull.*, 2008, **43**, 765.
9 J. Percival, E. Kendrick, R. I. Smith and P. R. Slater, *Dalton Trans.*, 2009, 5177.
10 J. Awaka, N. Kijima, Y. Takahashi, H. Hayakawa and J. Akimoto, *Solid State Ionics*, 2009, **180**, 602.
11 J. Awaka, N. Kijima, K. Kataoka, H. Hayakawa, K.-i. Ohshima and J. Akimoto, *J. Solid State Chem.*, 2010, **183**, 180.
12 S. Narayanan and V. Thangadurai, *J. Power Sources*, 2011, **196**, 8085.

13 S. K. S. Ohta, J. Seki, T. Saeki, S. Morishita and T. Asaoka, *J. Power Sources*, 2013, 53.
14 E. J. Cussen, *J. Mater. Chem.*, 2010, **20**, 5167.
15 V. Thangadurai, H. Kaack and W. J. F. Weppner, *J. Am. Ceram. Soc.*, 2003, **86**, 437.
16 V. Thangadurai and W. Weppner, *J. Solid State Chem.*, 2006, **179**, 974.
17 D. Mazza, *Mater. Lett.*, 1988, **7**, 205.
18 H. Hyooma and K. Hayashi, *Mater. Res. Bull.*, 1988, **23**, 1399.
19 V. Thangadurai, S. Adams and W. Weppner, *Chem. Mater.*, 2004, **16**, 2998.
20 E. J. Cussen, T. W. S. Yip, G. O'Neill and M. P. O'Callaghan, *J. Solid State Chem.*, 2011, **184**, 470.
21 M. Xu, M. S. Park, J. M. Lee, T. Y. Kim, Y. S. Park and E. Ma, *Phys. Rev. B: Condens. Matter Mater. Phys.*, 2012, **85**, 052301.
22 J. Han, J. Zhu, Y. Li, X. Yu, S. Wang, G. Wu, H. Xie, S. C. Vogel, F. Izumi, K. Momma, Y. Kawamura, Y. Huang, J. B. Goodenough and Y. Zhao, *Chem. Commun.*, 2012, **48**, 9840.
23 R. Jalem, Y. Yamamoto, H. Shiiba, M. Nakayama, H. Munakata, T. Kasuga and K. Kanamura, *Chem. Mater.*, 2013, **25**, 425.
24 M. Huang, A. Dumon and C.-W. Nan, *Electrochem. Commun.*, 2012, **21**, 62.
25 J. Wolfenstine, J. Ratchford, E. Rangasamy, J. Sakamoto and J. L. Allen, *Mater. Chem. Phys.*, 2012, **134**, 571.
26 J. L. Allen, J. Wolfenstine, E. Rangasamy and J. Sakamoto, *J. Power Sources*, 2012, **206**, 315.
27 J. Wolfenstine, J. Sakamoto and J. L. Allen, *J. Mater. Sci.*, 2012, **47**, 4428.
28 E. Rangasamy, J. Wolfenstine and J. Sakamoto, *Solid State Ionics*, 2012, **206**, 28.
29 M. A. Howard, O. Clemens, E. Kendrick, K. S. Knight, D. C. Apperley, P. A. Anderson and P. R. Slater, *Dalton Trans.*, 2012, **41**, 12048.
30 A. Kuhn, J.-Y. Choi, L. Robben, F. Tietz, M. Wilkening and P. Heitjans, *Z. Phys. Chem.*, 2012, **226**, 525.
31 S. Kumazaki, Y. Iriyama, K.-H. Kim, R. Murugan, K. Tanabe, K. Yamamoto, T. Hirayama and Z. Ogumi, *Electrochem. Commun.*, 2011, **13**, 509.
32 H. Buschmann, J. Doelle, S. Berendts, A. Kuhn, P. Bottke, M. Wilkening, P. Heitjans, A. Senyshyn, H. Ehrenberg, A. Lotnyk, V. Duppel, L. Kienle and J. Janek, *Phys. Chem. Chem. Phys.*, 2011, **13**, 19378.
33 A. Duevel, A. Kuhn, L. Robben, M. Wilkening and P. Heitjans, *J. Phys. Chem. C*, 2012, **116**, 15192.
34 H. Buschmann, S. Berendts, B. Mogwitz and J. Janek, *J. Power Sources*, 2012, **206**, 236.
35 T. Lina and V. Thangadurai, *Inorg. Chem.*, 2012, **51**, 1222.
36 L. Truong, M. Howard, O. Clemens, K. S. Knight, P. R. Slater and V. Thangadurai, *J. Mater. Chem. A*, 2013, DOI: 10.1039/c3ta13005c.
37 S. Narayanan, F. Ramezanipour and V. Thangadurai, *J. Phys. Chem. C*, 2012, **116**, 20154.
38 C. Galven, J. Dittmer, E. Suard, F. Le Berre and M. P. Crosnier-Lopez, *Chem. Mater.*, 2012, **24**, 3335.
39 S. Toda, K. Ishiguro, Y. Shimonishi, A. Hirano, Y. Takeda, O. Yamamoto and N. Imanishi, *Solid State Ionics*, 2013, **233**, 102.
40 C. Tande, D. Perez-Coll and G. C. Mather, *J. Mater. Chem.*, 2012, **22**, 11208.
41 D. Johnson, *ZView: a Software Program for IES Analysis 2.8*, 2008.
42 A. Coelho, *Topas Academic v4.1 Computer Software*, Brisbane, 2007.
43 J. Awaka, N. Kijima, H. Hayakawa and J. Akimoto, *J. Solid State Chem.*, 2009, **182**, 2046.
44 J. D. Gale, *J. Chem. Soc., Faraday Trans.*, 1997, **93**, 629.
45 C. R. A. Catlow, *Solid State Chemistry-Techniques*, Clarendon Press, Oxford, 1987.
46 C. R. A. Catlow, *Computer Modelling in Inorganic Crystallography*, Academic Press, San Diego, 1997, p. 340.
47 B. Dick and A. Overhauser, *Phys. Rev.*, 1958, **112**, 90.
48 N. F. Mott and M. J. Littleton, *Trans. Faraday Soc.*, 1938, **34**, 485.
49 (*a*) F. M. Higgins, N. H. de Leeuw and S. C. Parker, *J. Mater. Chem.*, 2002, **12**, 124; (*b*) D. W. Lewis, C. R. A. Catlow and J. M. Thomas, *Faraday Discuss.*, 1997, **106**, 451.
50 K. Wright and C. R. A. Catlow, *Phys. Chem. Miner.*, 1994, **20**, 515.
51 (*a*) A. Gatzemeier and K. Wright, *Phys. Chem. Miner.*, 2006, **33**, 115; (*b*) P. M. Panchmatia, A. Orera, E. Kendrick, J. V. Hanna, M. E. Smith, P. R. Slater and M. S. Islam, *J. Mater. Chem.*, 2010, **20**, 2766.
52 I. Barin and O. Knacke, *Thermochemical Properties of Inorganic Substances*, Springer-Verlag, Berlin, 1973.
53 Y. S. Touloukian and T. Makita, *Thermophysical properties of Matter*, IFI/Plenum, New York, 1970, vol. 6.
54 R. D. Shannon, *Acta Crystallogr., Sect. A: Cryst. Phys., Diffr., Theor. Gen. Crystallogr.*, 1976, **32**, 751.
55 G. Larraz, A. Orera and M. L. Sanjuan, *J. Mater. Chem.*, 2013, **1**, 11419.

5. Facile proton conduction in H^+/Li^+ ion-exchanged garnet-type fast Li-ion conducting $Li_5La_3Nb_2O_{12}$

5.1 Publication

Title: *Facile proton conduction in H^+/Li^+ ion-exchanged garnet-type fast Li-ion conducting $Li_5La_3Nb_2O_{12}$*

Submitted: 1st August 2013

Accepted: 10th September 2013

Information: *J. Mater. Chem.*, 2013, 1, 13469-13475

Times cited: 6 (18th September 2015)

Author contributions: L. Truong: Synthesis, X-ray diffraction, H^+/Li^+ exchange reactions, thermogravimetric analysis, FT-IR, Ionic conductivity studies of $Li_5La_3Nb_2O_{12}$

M. Howard: Neutron diffraction studies

O. Clemens: Guidance on neutron diffraction studies

K.S. Knight: Lead beam line scientist at HPRD Isis Rutherford Appleton Laboratories

P.R. Slater: Lead supervisor to M.A. Howard

V. Thangadurai: Lead supervisor to L. Truong

5.2 Highlights

- The successful exchange of some of the Li in $Li_5La_3Nb_2O_{12}$ for protons by immersion in water.

- First determination of location of the proton site in these exchanged garnets. The neutron diffraction studies showed that H exchanged preferentially for Li in the distorted octahedral sites.
- AC impedance measurements were carried out under different environments (3% H_2O + N_2 and 3% D_2O + N_2) on as-prepared $Li_5La_3Nb_2O_{12}$ which suggested proton conduction under humid conditions below 300 °C.
- The presence of proton conductivity was confirmed and the value was shown to be ~10^{-5} S cm^{-1} at room temperature, which is the same order of magnitude as Li ion conduction.

Journal of Materials Chemistry A

RSC Publishing

PAPER

View Article Online
View Journal | View Issue

Cite this: *J. Mater. Chem. A*, 2013, **1**, 13469

Facile proton conduction in H^+/Li^+ ion-exchanged garnet-type fast Li-ion conducting $Li_5La_3Nb_2O_{12}$

Lina Truong,[a] Matthew Howard,[b] Oliver Clemens,[b] Kevin S. Knight,[c] Peter R. Slater[b] and Venkataraman Thangadurai*[a]

Received 1st August 2013
Accepted 10th September 2013

DOI: 10.1039/c3ta13005c

www.rsc.org/MaterialsA

Garnet-type $Li_5La_3Nb_2O_{12}$, among several other Li-stuffed garnet compounds, is known to be unstable under moisture and undergoes H^+/Li^+ ion-exchange at room temperature. While there have been reports on proton-exchange in water, the transport of the protons in the garnet structure is yet to be characterized by electrical methods. In this work, proton-exchange was performed on the pellet form of $Li_5La_3Nb_2O_{12}$ for 4, 7, and 10 days, while the pellet generally showed less proton-exchange due to less surface area exposed to water, longer treatment times did allow the reaction to proceed further. Neutron diffraction (ND) studies were utilized to locate the H-site in the garnet-type structure and to confirm which Li ion sites were exchanged. For H exchanged $Li_5La_3Nb_2O_{12}$, the neutron diffraction studies indicated that H exchanged preferentially for Li in the distorted octahedral sites of the $Ia\bar{3}d$ space group (no. 230). AC impedance measurements were done on as-prepared $Li_5La_3Nb_2O_{12}$ under 3% $H_2O + N_2$ and 3% $D_2O + N_2$, which suggested proton conduction under humid conditions at 23–300 °C. $Li_5La_3Nb_2O_{12}$ shows a proton conductivity of 10^{-5} S cm^{-1}, of the same order of magnitude as Li ion conduction, at room temperature in humidity where protons seem to be incorporated from the solid and gas phase equilibrium reaction. Proton reversible Nafion electrode experiments indicate facile proton conduction in Li garnets under humidity.

6. Synthesis and Ionic conductivity of new high Li ion content garnets, $LnSr_2Ta_2Li_7O_{12}$ (Ln = La, Pr, Nd, Sm, Gd)

6.1 Draft Publication

Title: *Synthesis and Ionic conductivity of new high Li ion content garnets, $LnSr_2Ta_2Li_7O_{12}$ (Ln = La, Pr, Nd, Sm, Gd)*

Information: Submitted to *Dalton Transactions* (23rd April 2015)

Author contributions: M.A Howard: Synthesis, Li ion conductivity and thermogravimetric studies of garnet phases $LnSr_2Ta_2Li_7O_{12}$ (Ln = La, Pr, Nd, Sm or Gd), analysis of variable temperature X-ray diffraction studies

O. Clemens: Running of variable X-ray diffraction studies

P.A. Anderson: Supervisor to M.A. Howard

P.R. Slater: Lead supervisor to M.A. Howard

6.2 Highlights

- The successful synthesis of new $LnSr_2Ta_2Li_7O_{12}$ (Ln = La, Pr, Nd, Sm, Gd) garnet phases.
- The demonstration that these “Li7” garnets all adopt tetragonal symmetry consistent with Li ordering
- The demonstration that these systems are susceptible to moisture from the air, which leads to partial H^+/Li^+ Exchange

Dalton Transactions

Article

Synthesis and Ionic conductivity of new high Li ion content garnets, $LnSr_2Ta_2Li_7O_{12}$ (Ln = La, Pr, Nd, Sm, Gd)

Received 00th January 20xx,
Accepted 00th January 20xx

DOI: 10.1039/x0xx00000x

www.rsc.org/

M. A. Howard[a], O. Clemens[a,b,c], P. A. Anderson[a], P. R. Slater[a]

The abstract should be a single paragraph that summarises the content of the article In this paper we report the synthesis and Li ion conductivity of the new high Li content garnet phases $LnSr_2Ta_2Li_7O_{12}$ (Ln = La, Pr, Nd, Sm or Gd). Close inspection of the X-ray diffraction patterns indicate that these systems are mostly composed of the ordered tetragonal garnet phase, along with a small amount of cubic garnet. The presence of a small amount of cubic garnet phase can most likely be correlated with partial Li loss on synthesis as well as some degree of H^+/Li^+ exchange. The latter was supported by results from variable temperature X-ray diffraction studies and thermogravimetric analysis. In line with other tetragonal garnet systems, the Li ion conductivity is shown to be low, consistent with the ordered nature of the Li distribution, which is required to accommodate the high Li ion content.

7. Hydrogen absorption and lithium ion conductivity in Li_6NBr_3

7.1 Publication

Title: *Hydrogen absorption and lithium ion conductivity in Li_6NBr_3*

Available online: 22nd January 2015

Information: J. Alloys Compd., 645, Supplement 1 (2015) S174-S177

Author contributions: M.A Howard: Synthesis of Li_6NBr_3 and Hydrogen uptake reactions, X-ray diffraction, Raman spectroscopy, A.C. impedance spectroscopy studies

O. Clemens: Structural advisor

P.R. Slater: Supervisor to M.A. Howard

P.A. Anderson: Lead supervisor to M.A. Howard

7.2 Highlights

- Synthesis of Li_6NBr_3 *via* solid state methods and hydrogenation was successfully attempted.
- Hydrogenation of a lithium nitride halide was demonstrated for the first time.
- It was shown through powder X-ray diffraction and Raman spectroscopy that hydrogenation had gone to completion.
- The Li ion conductivity of Li_6NBr_3 and Li_3N were measured and compared using A.C. impedance spectroscopy.
- Li_6NBr_3 showed a lower conductivity than Li_3N, which may be a significant factor in the kinetics of the hydrogenation process and its higher hydrogenation temperature.

Journal of Alloys and Compounds 645 (2015) S174–S177

Contents lists available at ScienceDirect

Journal of Alloys and Compounds

journal homepage: www.elsevier.com/locate/jalcom

Hydrogen absorption and lithium ion conductivity in Li_6NBr_3

M.A. Howard [a], O. Clemens [a,b,c], P.R. Slater [a], P.A. Anderson [a,*]

[a] School of Chemistry, University of Birmingham, Edgbaston, Birmingham B15 2TT, UK
[b] Technical University of Darmstadt, Joint Research Laboratory Nanomaterials, Jovanka-Bontschits-Straße 2, 64287 Darmstadt, Germany
[c] Karlsruhe Institute of Technology, Institute of Nanotechnology, Hermann-von-Helmholtz-Platz 1, 76344 Eggenstein-Leopoldshafen, Germany

ARTICLE INFO

Article history:
Available online 22 January 2015

Keywords:
Hydrogen storage materials
Lithium nitride
Lithium bromide
Lithium ion conductivity
Powder X-ray diffraction
A.C. impedance spectroscopy

ABSTRACT

The reaction of lithium amide and imide with lithium halides to form new amide halide or imide halide phases has led to improved hydrogen desorption and absorption properties and, for the amides, lithium ion conductivities. Here we investigate the effect of bromide incorporation on the ionic conductivity and hydrogen absorption properties of lithium nitride. For the first time we show that it is possible for a lithium halide nitride, the cubic bromide nitride Li_6NBr_3, to take up hydrogen—a necessary condition for potential use as a reversible solid-state hydrogen storage material. Powder X-ray diffraction showed the formation of $Li_2Br(NH_2)$ and LiBr, and Raman spectroscopy confirmed that only amide anions were present and that the hydrogen uptake reaction had gone to completion. The lithium ion conductivity of Li_6NBr_3 at the hydrogenation temperature was found to be less than that of Li_3N, which may be a significant factor in the kinetics of the hydrogenation process.

8. Structure, lithium ion conductivity and hydrogenation properties of lithium chloride nitrides

8.1 Draft Publication

Title: Structure, lithium ion conductivity and hydrogenation properties of lithium chloride nitrides

Information: Submitted to *International journal of hydrogen energy* (10th September 2015)

Author contributions: M.A Howard: Synthesis of lithium nitride chlorides and Hydrogen uptake reactions, X-ray diffraction, Raman spectroscopy, A.C. impedance spectroscopy studies

M. Gough: Initial synthesis and hydrogenation studies for undergraduate dissertation project

O. Clemens: Structural advisor

P.R. Slater: Supervisor to M.A. Howard

P.A. Anderson: Lead supervisor to M.A. Howard

8.2 Highlights

- The synthesis and a systematic crystallographic comparison of the structures of known lithium chloride nitrides (Li_4NCl and $Li_9N_2Cl_3$) and has been carried out.
- For the first time it has been demonstrated that it is possible to hydrogenate these materials (at 250°C under 90 bar H_2). For Li_4NCl, and $Li_9N_2Cl_3$, the crystalline hydrogenated products were the known amide chlorides $Li_4(NH_2)_3Cl$ and $Li_7(NH_2)_6Cl$, respectively, which both release hydrogen reversibly on heating.
- Through Rietveld analysis of powder XRD data, it has been shown for the first time that the lithium is displaced from its 'ideal' position towards a corner of the tetrahedral site occupied by a nitride anion in $Li_9N_2Cl_3$. The relationship between the structures and ionic conductivity measurements on both chloride nitrides was investigated.

- It was found by annealing $Li_9N_2Cl_3$ at 300°C that it is metastable, decomposing on heating to LiCl and an antifluorite phase with reduced chloride content and Li ion conductivity.
- Results are broadly consistent with the thesis that ion mobility may play an important role in the hydrogenation process.

International Journal of Hydrogen Energy

ARTICLE

Structure, lithium ion conductivity and hydrogenation properties of lithium chloride nitrides

Received 00th January 20xx,
Accepted 00th January 20xx

DOI: 10.1039/x0xx00000x

M. A. Howard[1], M. J Gough[1], O. Clemens[1,2,3], P. R. Slater[1], P. A. Anderson[1]

A systematic crystallographic comparison of the structures of known lithium chloride nitrides has been carried out and for the first time their hydrogenation (at 250°C under 90 bar H_2) has been demonstrated. For Li_4NCl, and $Li_9N_2Cl_3$, the crystalline hydrogenated products were the known amide chlorides $Li_4(NH_2)3Cl$ and Li7(NH2)6Cl, respectively, which both release hydrogen reversibly on heating. These results are discussed in the context of new structural and ionic conductivity measurements on both chloride nitrides. Through Rietveld analysis of powder XRD data, it has been shown for the first time that the lithium is displaced from its 'ideal' position towards a corner of the tetrahedral site occupied by a nitride anion in Li9N2Cl3. Annealing at 300°C showed that Li9N2Cl3 is metastable, decomposing on heating to LiCl and an antifluorite phase with reduced chloride content and Li ion conductivity. Results are broadly consistent with the thesis that ion mobility may play an important role in the hydrogenation process.

9. Conclusions and further work

9.1 Conclusion

In this thesis we have investigated the structures of lithium-containing garnets and lithium halide nitrides and the effect that this has on their lithium ion conductivity and subsequently their performance for the desired application.

Several new garnet phases containing 7 lithium atoms per formula unit have been synthesised. We have shown that increasing the lithium content to 7 causes a change in the unit cell symmetry from the traditional cubic unit cell to a tetragonal unit cell. This change in the unit cell is due to an ordering in the lithium sublattice to prevent short Li–Li bond distances. The ordering causes a decrease in the Li ion conductivity due to the lack of vacancies for conduction to occur.

Nevertheless, it is possible to improve the Li ion conductivity of these garnet structures containing 7 Li atoms through doping with a small amount of trivalent (Al or Ga) cations. It was found that the preferred dopant site is the ideal tetrahedral (Li1) site which was confirmed with computational studies.

A key discovery was that these materials will undergo H^+/Li^+ exchange when left in air. This exchange can affect the ionic conductivity in a number of ways. In $La_3Zr_2Ga_{0.5}Li_{5.5}O_{12}$ it was seen that the exchange caused a reduction in grain boundary resistance thus lowering the total lithium ion conductivity. This exchange was confirmed through both variable temperature X-ray diffraction studies and thermogravimetric analysis. In $Nd_3Zr_2Li_{7-3x}Al_xO_{12}$ it was shown, through conductivity studies where the lateral surface was modified, that the observed improvements at low temperatures in the lithium ion conductivity were due to bulk effects and not due to surface conduction. It was also shown that the H^+/Li^+ exchange not only affects the cubic systems but also the tetragonal systems as improvements in the Li ion conductivity were observed.

In order to confirm and also determine the location of the exchanged H^+, neutron diffraction studies were carried out on the H^+/Li^+ exchanged $Li_5La_3Nb_2O_{12}$. These studies were able to show that the exchanged proton is located within one of the distorted octahedral Li sites, pointing towards the Li site. This work shows that the garnet materials are highly affected by moisture from air and great care should be taken when preparing and measuring their Li ion conductivity.

The structure of $Li_9N_2Cl_3$ was successfully determined through powder X-ray diffraction as there had been a number of different models for the true structure of this material.

It has been shown for the first time that it is possible for 3 different lithium nitride halide structure types to take up hydrogen. Their hydrogenation conditions were compared to that of Li_3N, which was shown to hydrogenate under less harsh conditions than the lithium halide nitrides. These results are consistent with the hypothesis that the higher Li ion conductivity of Li_3N is a key factor in kinetics of hydrogenation.

9.2 Further Work

Future work into lithium-conducting garnet materials would be to understand the effect on the conduction mechanism due to the H^+/Li^+ exchange within these materials. In this respect, more detailed computer modelling studies are warranted to investigate the conduction pathways for Li^+/H^+. The development of a true understanding of the conduction mechanisms will provide key information for optimising these materials for Li ion battery applications or pushing these materials forward into different applications., e.g. the demonstration of significant proton conductivity suggests the potential for exploitation of these systems for use as fuel cell electrolytes.

Investigations into the optimum dopant level of the trivalent cations on the ideal tetrahedral site for improved Li ion conductivity and investigations into the co-doping of trivalent cations onto this site may result in possible benefits to the ionic mobility. Furthermore, while there has been significant work on cation substitutions into these garnet electrolytes, the possibility of anion substitutions (.e.g.

F, N, S) has not been considered, and this area opens up another potential strategy for the optimisation of these systems.

As mentioned in chapter 1.2.5 there have been a number of reports of successful compatibility studies of lithium-conducting garnets with electrode materials. Work into improving the electrode/electrolyte surface interface would be beneficial should the conductivity of the garnet electrolyte be improved sufficiently for practical use.

With current developments in Li–air batteries, garnets could be used as an electrolyte or a separator within this developing technology. However, issues with H^+/Li^+ exchange must first be resolved.

Should the conductivity and exchange problems be resolved then these materials would be the ideal solid state electrolyte for all-solid-state Li ion batteries.

As the structure of Li_6NBr_3 has never been fully resolved, further structural studies could be performed. Once the structure has been determined doping studies to improve the Li ion conductivity may prove fruitful.

As lithium nitride halides showed worse hydrogen kinetics than Li_3N, possibly as a result of their lower ionic conductivity, the promise for these materials for hydrogen storage is limited at this time. However, doping studies (Mg or Al) to improve the Li ion conductivity could see these materials becoming more viable in the future.

References

1. V. Thangadurai, H. Kaack and W. J. F. Weppner, *J. Am. Ceram. Soc.*, 2003, 86, 437-440.
2. M. Cheng, E. Rangasamy, C. Liang, J. Sakamoto, K. L. More and M. Chi, *Angew. Chem. Int. Ed.*, 2015, 54, 129-133.
3. M. A. Howard, O. Clemens, K. S. Knight, P. A. Anderson, S. Hafiz, P. M. Panchmatia and P. R. Slater, *J. Mater. Chem.*, 2013, 1, 14013-14022.
4. P. A. Anderson, P. A. Chater, D. R. Hewett and P. R. Slater, *Faraday. Discuss.*, 2011, 151, 271-284.
5. J. Percival, E. Kendrick, R. I. Smith and P. R. Slater, *Dalton. Trans.*, 2009, 5177-5181.
6. J. Percival, E. Kendrick and P. R. Slater, *Solid. State. Ionics.*, 2008, 179, 1666-1669.
7. J. Percival, E. Kendrick and P. R. Slater, *Mater. Res. Bull.*, 2008, 43, 765-770.
8. J. Percival and P. R. Slater, *Solid. State. Commun.*, 2007, 142, 355-357.
9. P. P. Kumar and S. Yashonath, *J. Chem. Sci.*, 2006, 118, 135-154.
10. A. R. West, *Basic Solid State Chemistry*, Wiley, 2nd edn., 2009.
11. L. E. Smart and E. A. Moore, *Solid State Chemistry: An Introduction* Taylor & Francis Group, 3rd edn., 2005.
12. X. S. Huang, *J. Solid. State. Electrochem.*, 2011, 15, 649-662.
13. J. Brous, I. Fankuchen and E. Banks, *Acta Crystallogr.*, 1953, 6, 67-70.
14. Y. Inaguma, L. Q. Chen, M. Itoh, T. Nakamura, T. Uchida, H. Ikuta and M. Wakihara, *Solid. State. Commun.*, 1993, 86, 689-693.
15. A. G. Belous, G. N. Novitskaya, S. V. Polyanetskaya and Y. I. Gornikov, *Inorg. Mater.*, 1987, 23, 412-415.
16. Y. Inaguma, L. Chen, M. Itoh and T. Nakamura, *Solid. State. Ionics.*, 70-71, Part 1, 196-202.
17. A. D. Robertson, S. G. Martin, A. Coats and A. R. West, *J. Mater. Chem.*, 1995, 5, 1405-1412.
18. J. L. Fourquet, H. Duroy and M. P. CrosnierLopez, *J. Solid. State. Chem.*, 1996, 127, 283-294.
19. C. W. Ban and G. M. Choi, *Solid. State. Ionics.*, 2001, 140, 285-292.
20. J. S. Lee, K. S. Yoo, T. S. Kim and H. J. Jung, *Solid. State. Ionics.*, 1997, 98, 15-26.
21. J. A. Alonso, J. Sanz, J. Santamaría, C. León, A. Várez and M. T. Fernández-Díaz, *Angew. Chem. Int. Ed.*, 2000, 39, 619-621.
22. Y. Harada, T. Ishigaki, H. Kawai and J. Kuwano, *Solid. State. Ionics.*, 1998, 108, 407-413.
23. J. Ibarra, A. Várez, C. León, J. Santamaría, L. M. Torres-Martínez and J. Sanz, *Solid. State. Ionics.*, 2000, 134, 219-228.
24. A. D. Robertson, A. R. West and A. G. Ritchie, *Solid. State. Ionics.*, 1997, 104, 1-11.
25. H. Kawai and J. Kuwano, *J. Electrochem. Soc.*, 1994, 141, L78-L79.
26. K. J. Weber N, *Proc Annu Power Sources Conf*, 1967, 21, 37.
27. Whitting.Ms and R. A. Huggins, *J. Chem. Phys.*, 1971, 54, 414-&.
28. H. Y. P. Hong, *Mater. Res. Bull.*, 1976, 11, 173-182.
29. J. B. Goodenough, H. Y. P. Hong and J. A. Kafalas, *Mater. Res. Bull.*, 1976, 11, 203-220.
30. R. Norhaniza, R. H. Y. Subban and N. S. Mohamed, *J. Mater. Sci.*, 2011, 46, 7815-7821.
31. K. Arbi, M. A. Paris and J. Sanz, *Dalton. Trans.*, 2011, 40, 10195-10202.
32. H. Xie, J. B. Goodenough and Y. T. Li, *J. Power. Sources.*, 2011, 196, 7760-7762.
33. H. Aono, E. Sugimoto, Y. Sadaoka, N. Imanaka and G. Y. Adachi, *Solid. State. Ionics.*, 1993, 62, 309-316.
34. P. R. Slater and C. Greaves, *J. Mater. Chem.*, 1994, 4, 1463-1467.
35. E. Morin, J. Angenault, J. C. Couturier, M. Quarton, H. He and J. Klinowski, *Eur. J. Solid State Inorg. Chem.*, 1997, 34, 947-958.
36. A. S. Andersson, B. Kalska, P. Jonsson, L. Haggstrom, P. Nordblad, R. Tellgren and J. O. Thomas, *J. Mater. Chem.*, 2000, 10, 2542-2547.
37. V. Thangadurai, A. K. Shukla and J. Gopalakrishnan, *J. Mater. Chem.*, 1999, 9, 739-741.
38. O. Bohnke, S. Ronchetti and D. Mazza, *Solid. State. Ionics.*, 1999, 122, 127-136.

39. P. Colomban and E. Mouchon, *Solid. State. Ionics.*, 1994, 73, 209-220.
40. P. R. Rudolf, A. Clearfield and J. D. Jorgensen, *J. Solid. State. Chem.*, 1988, 72, 100-112.
41. A. Martinezjuarez, J. M. Rojo, J. E. Iglesias and J. Sanz, *Chem. Mat.*, 1995, 7, 1857-1862.
42. A. Martinez, J. M. Rojo, J. E. Iglesias, J. Sanz and R. M. Rojas, *Chem. Mat.*, 1994, 6, 1790-1795.
43. M. Catti, N. Morgante and R. M. Ibberson, *J. Solid. State. Chem.*, 2000, 152, 340-347.
44. R. Ruffo, C. M. Mari and M. Catti, *Ionics.*, 2001, 7, 105-108.
45. M. Catti, *J. Solid. State. Chem.*, 2001, 156, 305-312.
46. K. M. Begam, M. S. Michael, Y. H. Taufiq-Yap and S. R. S. Prabaharan, *Electrochem. Solid. St.*, 2004, 7, A242-A246.
47. S. Patoux, G. Rousse, J. B. Leriche and C. Masquelier, *Solid State Sci.*, 2004, 6, 1113-1120.
48. J. E. Iglesias and C. Pecharroman, *Solid. State. Ionics.*, 1998, 112, 309-318.
49. K. Arbi, M. A. Paris and J. Sanz, *J. Phys. Chem. B*, 2006, 110, 6454-6457.
50. I. A. Stenina, M. N. Kislitsyn, I. Y. Pinus, S. M. Haile and A. B. Yaroslavtsev, in *Diffusion in Solids - Past, Present and Future*, eds. B. S. Bokstein and B. B. Straumal, Trans Tech Publications Ltd, Zurich-Uetikon, 2006, vol. 249, pp. 255-262.
51. I. A. Stenina, M. N. Kislitsyn, I. Y. Pinus, I. V. Arkhangel'skii, N. A. Zhuravlev and A. B. Yaroslavtsev, *Russ. J. Inorg. Chem.*, 2005, 50, 906-911.
52. I. A. Stenina, I. Y. Pinus, A. I. Rebrov and A. B. Yaroslavtsev, *Solid. State. Ionics.*, 2004, 175, 445-449.
53. M. A. Paris and J. Sanz, *Phys. Rev. B*, 2000, 62, 810-817.
54. N. Anantharamulu, K. K. Rao, G. Rambabu, B. V. Kumar, V. Radha and M. Vithal, *J. Mater. Sci.*, 2011, 46, 2821-2837.
55. L. O. Hagman and Kierkega.P, *Acta Chem. Scand. Ser. A*, 1968, 22, 1822-&.
56. H. Aono, E. Sugimoto, Y. Sadaoka, N. Imanaka and G. Y. Adachi, *J. Electrochem. Soc.*, 1989, 136, 590-591.
57. A. R. West, *J. Appl. Electrochem.*, 1973, 3, 327.
58. I. M. Hodge, M. D. Ingram and A. R. West, *J. Am. Ceram. Soc.*, 1976, 59, 360-366.
59. K. Jackowska and A. R. West, *J. Appl. Electrochem.*, 1985, 15, 459-468.
60. Y. W. Hu, I. D. Raistrick and R. A. Huggins, *Mater. Res. Bull.*, 1976, 11, 1227-1230.
61. R. A. Huggins, *Electrochim. Acta.*, 1977, 22, 773-781.
62. R. D. Shannon, B. E. Taylor, A. D. English and T. Berzins, *Electrochim. Acta.*, 1977, 22, 783-796.
63. A. Khorassani and A. R. West, *Solid. State. Ionics.*, 1982, 7, 1-8.
64. A. Khorassani and A. R. West, *J. Solid. State. Chem.*, 1984, 53, 369-375.
65. H. Y. P. Hong, *Mater. Res. Bull.*, 1978, 13, 117-124.
66. P. G. Bruce and A. R. West, *Mater. Res. Bull.*, 1980, 15, 379-385.
67. L. Sebastian, R. S. Jayashree and J. Gopalakrishnan, *J. Mater. Chem.*, 2003, 13, 1400-1405.
68. G. C. Farrington, B. S. Dunn and J. L. Briant, *Solid. State. Ionics.*, 1981, 3-4, 405-408.
69. M. D. Lewis, N. Kimura and M. Greenblatt, *J. Solid. State. Chem.*, 1985, 58, 401-403.
70. J. Grins and A. R. West, *J. Solid. State. Chem.*, 1986, 65, 265-271.
71. L. J. Gillie, S. A. de Souza, D. Sheptyakov, N. Reeves-McLaren, D. Pasero and A. R. West, *J. Solid. State. Chem.*, 2010, 183, 2589-2597.
72. J. Grins, L. Banos, D. C. Sinclair and A. R. West, *J. Mater. Chem.*, 1994, 4, 445-447.
73. E. J. Cussen, *Chem. Commun.*, 2006, 4, 412-413.
74. C. Galven, J. L. Fourquet, M. P. Crosnier-Lopez and F. Le Berre, *Chem. Mat.*, 2011, 23, 1892-1900.
75. M. A. Howard, O. Clemens, E. Kendrick, K. S. Knight, D. C. Apperley, P. A. Anderson and P. R. Slater, *Dalton. Trans.*, 2012, 41, 12048-12053.
76. G. Larraz, A. Orera and M. L. Sanjuan, *J. Mater. Chem.*, 2013, 1, 11419-11428.
77. W. G. Wang, Q. F. Fang and G. L. Hao, *Adv. Mat. Res.*, 2012, 463-464, 123-127.
78. C. Galven, J. Dittmer, E. Suard, F. Le Berre and M.-P. Crosnier-Lopez, *Chem. Mat.*, 2012, 24, 3335-3345.
79. L. Truong and V. Thangadurai, *Chem. Mat.*, 2011, 23, 3970-3977.

80. G. Larraz, A. Orera, J. Sanz, I. Sobrados, V. Diez-Gomez and M. L. Sanjuan, *J. Mater. Chem.*, 2015, DOI: 10.1039/C4TA04570J.
81. T. Lina and V. Thangadurai, *Inorg. Chem.*, 2012, 51, 1222-1224.
82. L. Truong, M. Howard, O. Clemens, K. S. Knight, P. R. Slater and V. Thangadurai, *J. Mater. Chem.*, 2013, 1, 13469-13475.
83. C. Galven, E. Suard, D. Mounier, M. P. Crosnier-Lopez and F. Le Berre, *J. Mater. Res.*, 2013, 28, 2147-2153.
84. C. Liu, K. Rui, C. Shen, M. E. Badding, G. X. Zhang and Z. Y. Wen, *J. Power. Sources.*, 2015, 282, 286-293.
85. Y. X. Gao, X. P. Wang, W. G. Wang, Z. Zhuang, D. M. Zhang and Q. F. Fang, *Solid. State. Ionics.*, 2010, 181, 1415-1419.
86. R. Murugan, V. Thangadurai and W. Weppner, *Ionics.*, 2007, 13, 195-203.
87. R. Murugan, W. Weppner, P. Schmid-Beurmann and V. Thangadurai, *Mater. Sci. Eng. B-Solid State Mater. Adv. Technol.*, 2007, 143, 14-20.
88. R. Murugan, W. Weppner, P. Schmid-Beurmann and V. Thangadurai, *Mater. Res. Bull.*, 2008, 43, 2579-2591.
89. S. Narayanan, F. Ramezanipour and V. Thangadurai, *J. Phys. Chem. C*, 2012, 116, 20154-20162.
90. S. Narayanan and V. Thangadurai, *J. Power. Sources.*, 2011, 196, 8085-8090.
91. S. Narayanan and V. Thangadurai, *J. Power. Sources.*, 2011, 196, 8085-8090.
92. M. P. O'Callaghan and E. J. Cussen, *Chem. Commun.*, 2007, 20, 2048-2050.
93. J. Percival, D. Apperley and P. R. Slater, *Solid. State. Ionics.*, 2008, 179, 1693-1696.
94. I. P. Roof, M. D. Smith, E. J. Cussen and H. C. zur Loye, *J. Solid. State. Chem.*, 2009, 182, 295-300.
95. V. Thangadurai, S. Adams and W. Weppner, *Chem. Mat.*, 2004, 16, 2998-3006.
96. V. Thangadurai and W. Weppner, *Adv. Funct. Mater.*, 2005, 15, 107-112.
97. V. Thangadurai and W. Weppner, *J. Solid. State. Chem.*, 2006, 179, 974-984.
98. V. Thangadurai and W. Weppner, *J. Power. Sources.*, 2005, 142, 339-344.
99. V. Thangadurai and W. Weppner, *J. Am. Ceram. Soc.*, 2005, 88, 411-418.
100. M. Xu, M. S. Park, J. M. Lee, T. Y. Kim, Y. S. Park and E. Ma, *Phys. Rev. B*, 2012, 85.
101. C. Y. Yoo, S. C. Kim, S. S. Lee and S. J. Kim, *Acta Crystallogr. Sect. E.-Struct Rep. Online*, 2009, 65, I74-U161.
102. M. P. O'Callaghan, D. R. Lynham, E. J. Cussen and G. Z. Chen, *Chem. Mat.*, 2006, 18, 4681-4689.
103. D. Mazza, *Mater. Lett.*, 1988, 7, 205-207.
104. H. Hyooma and K. Hayashi, *Mater. Res. Bull.*, 1988, 23, 1399-1407.
105. M. Kotobuki and K. Kanamura, *Ceram. Int.*, 2013, 39, 6481-6487.
106. R. Murugan, V. Thangadurai and W. Weppner, *Appl. Phys. A-Mater. Sci. Process.*, 2008, 91, 615-620.
107. E. J. Cussen and T. W. S. Yip, *J. Solid. State. Chem.*, 2007, 180, 1832-1839.
108. R. Murugan, V. Thangadurai and W. Weppner, *J. Electrochem. Soc.*, 2008, 155, A90-A101.
109. J. Awaka, N. Kijima, Y. Takahashi, H. Hayakawa and J. Akimoto, *Solid. State. Ionics.*, 2009, 180, 602-606.
110. H. Xie, Y. Li, J. Han, Y. Dong, M. P. Paranthaman, L. Wang, M. Xu, A. Gupta, Z. Bi, C. A. Bridges, M. Nakanishi, A. P. Sokolov and J. B. Goodenough, *J. Electrochem. Soc.*, 2012, 159, A1148-A1151.
111. R. Murugan, V. Thangadurai and W. Weppner, *Angew. Chem. Int. Ed.*, 2007, 46, 7778-7781.
112. Y. Zhong, Q. Zhou, Y. Guo, Z. Li and Y. Qiang, *Ionics.*, 2013, 19, 697-700.
113. W. G. Zeier, S. L. Zhou, B. Lopez-Bermudez, K. Page and B. C. Melot, *ACS Appl. Mater. Interfaces*, 2014, 6, 10900-10907.
114. Y. Li, J.-T. Han, C.-A. Wang, S. C. Vogel, H. Xie, M. Xu and J. B. Goodenough, *J. Power. Sources.*, 2012, 209, 278-281.
115. J. Awaka, N. Kijima, H. Hayakawa and J. Akimoto, *J. Solid. State. Chem.*, 2009, 182, 2046-2052.
116. J. Percival, E. Kendrick, R. I. Smith and P. R. Slater, *Dalton. Trans.*, 2009, 26, 5177-5181.

117. R. Murugan, V. Thangadurai and W. Weppner, *Angew. Chem. Int. Ed.*, 2007, 46, 7778-7781.
118. H. Xie, J. A. Alonso, Y. T. Li, M. T. Fernandez-Diaz and J. B. Goodenough, *Chem. Mat.*, 2011, 23, 3587-3589.
119. A. Kuhn, S. Narayanan, L. Spencer, G. Goward, V. Thangadurai and M. Wilkening, *Phys. Rev. B*, 2011, 83.
120. I. Kokal, M. Somer, P. H. L. Notten and H. T. Hintzen, *Solid. State. Ionics.*, 2011, 185, 42-46.
121. C. A. Geiger, E. Alekseev, B. Lazic, M. Fisch, T. Armbruster, R. Langner, M. Fechtelkord, N. Kim, T. Pettke and W. Weppner, *Inorg. Chem.*, 2011, 50, 1089-1097.
122. Y. X. Wang and W. Lai, *Electrochem. Solid. St.*, 2012, 15, A68-A71.
123. G. T. Hitz, E. D. Wachsman and V. Thangadurai, *J. Electrochem. Soc.*, 2013, 160, A1248-A1255.
124. E. Rangasamy, J. Wolfenstine and J. Sakamoto, *Solid. State. Ionics.*, 2012, 206, 28-32.
125. A. Kuhn, J.-Y. Choi, L. Robben, F. Tietz, M. Wilkening and P. Heitjans, *Z. Phys. Chem.*, 2012, 226, 525-537.
126. A. Duevel, A. Kuhn, L. Robben, M. Wilkening and P. Heitjans, *J. Phys. Chem. C*, 2012, 116, 15192-15202.
127. J. M. Lee, T. Kim, S. W. Baek, Y. Aihara, Y. Park, Y. I. Kim and S. G. Doo, *Solid. State. Ionics.*, 2014, 258, 13-17.
128. J. Wolfenstine, J. Ratchford, E. Rangasamy, J. Sakamoto and J. L. Allen, *Mater. Chem. Phys.*, 2012, 134, 571-575.
129. R. Jalem, M. J. D. Rushton, W. Manalastas, M. Nakayama, T. Kasuga, J. A. Kilner and R. W. Grimes, *Chem. Mat.*, 2015, 27, 2821-2831.
130. L. Dhivya, N. Janani, B. Palanivel and R. Murugan, *AIP. Adv.*, 2013, 3.
131. K. Ishiguro, Y. Nakata, M. Matsui, I. Uechi, Y. Takeda, O. Yamamoto and N. Imanishi, *J. Electrochem. Soc.*, 2013, 160, A1690-A1693.
132. S. Song, B. Yan, F. Zheng, D. Hai Minh and L. Lu, *Solid. State. Ionics.*, 2014, 268, 135-139.
133. T. Thompson, J. Wolfenstine, J. L. Allen, M. Johannes, A. Huq, I. N. David and J. Sakamoto, *J. Mater. Chem.*, 2014, 2, 13431-13436.
134. S. Ramakumar, L. Satyanarayana, S. V. Manorama and R. Murugan, *Phys. Chem. Chem. Phys.*, 2013, 15, 11327-11338.
135. X. Tong, V. Thangadurai and E. D. Wachsman, *Inorg. Chem.*, 2015, 54, 3600-3607.
136. E. Hanc, W. Zajac and J. Molenda, *Solid. State. Ionics.*, 2014, 262, 617-621.
137. A. Dumon, M. Huang, Y. Shen and C. W. Nan, *Solid. State. Ionics.*, 2013, 243, 36-41.
138. M. P. O'Callaghan, A. S. Powell, J. J. Titman, G. Z. Chen and E. J. Cussen, *Chem. Mat.*, 2008, 20, 2360-2369.
139. S. Ramakumar, N. Janani and R. Murugan, *Dalton. Trans.*, 2015, 44, 539-552.
140. A. K. Baral, S. Narayanan, F. Ramezanipour and V. Thangadurai, *Phys. Chem. Chem. Phys.*, 2014, 16, 11356-11365.
141. Y. X. Wang, A. Huq and W. Lai, *Solid. State. Ionics.*, 2014, 255, 39-49.
142. R. Jalem, Y. Yamamoto, H. Shiiba, M. Nakayama, H. Munakata, T. Kasuga and K. Kanamura, *Chem. Mat.*, 2013, 25, 425-430.
143. Y. Wang, M. Klenk, K. Page and W. Lai, *Chem. Mat.*, 2014, 26, 5613-5624.
144. S. G. Kang and D. S. Sholl, *J. Phys. Chem. C*, 2014, 118, 17402-17406.
145. K. H. Kim, Y. Iriyama, K. Yamamoto, S. Kumazaki, T. Asaka, K. Tanabe, C. A. J. Fisher, T. Hirayama, R. Murugan and Z. Ogumi, *J. Power. Sources.*, 2011, 196, 764-767.
146. M. Kotobuki, H. Munakata, K. Kanamura, Y. Sato and T. Yoshida, *J. Electrochem. Soc.*, 2010, 157, A1076-A1079.
147. S. Ohta, J. Seki, Y. Yagi, Y. Kihira, T. Tani and T. Asaoka, *J. Power. Sources.*, 2014, 265, 40-44.
148. C. Bernuy-Lopez, W. Manalastas, J. M. L. del Amo, A. Aguadero, F. Aguesse and J. A. Kilner, *Chem. Mat.*, 2014, 26, 3610-3617.
149. Y. Jin and P. J. McGinn, *J. Power. Sources.*, 2013, 239, 326-331.
150. Y. X. Wang and W. Lai, *J. Power. Sources.*, 2015, 275, 612-620.
151. L. Truong, J. Colter and V. Thangadurai, *Solid. State. Ionics.*, 2013, 247, 1-7.

152. C. Ma, E. Rangasamy, C. Liang, J. Sakamoto, K. L. More and M. Chi, *Angew. Chem. Int. Ed.*, 2015, 54, 129-133.
153. M. Matsui, K. Sakamoto, K. Takahashi, A. Hirano, Y. Takeda, O. Yamamoto and N. Imanishi, *Solid. State. Ionics.*, 2014, 262, 155-159.
154. M. Matsui, K. Takahashi, K. Sakamoto, A. Hirano, Y. Takeda, O. Yamamoto and N. Imanishi, *Dalton. Trans.*, 2014, 43, 1019-1024.
155. Y. Zhang, F. Chen, R. Tu, Q. Shen and L. Zhang, *J. Power. Sources.*, 2014, 268, 960-964.
156. R. Djenadic, M. Botros, C. Benel, O. Clemens, S. Indris, A. Choudhary, T. Bergfeldt and H. Hahn, *Solid. State. Ionics.*, 2014, 263, 49-56.
157. Y. Ren, H. Deng, R. Chen, Y. Shen, Y. Lin and C.-W. Nan, *J. Eur. Ceram. Soc*, 2015, 35, 561-572.
158. C.-W. Ahn, J.-J. Choi, J. Ryu, B.-D. Hahn, J.-W. Kim, W.-H. Yoon, J.-H. Choi and D.-S. Park, *J. Electrochem. Soc.*, 2015, 162, A60-A63.
159. H. Katsui and T. Goto, *Thin Solid Films*, 2015, 584, 130-134.
160. *Targets for Onboard Hydrogen Storage Systems for Light-Duty Vehicles Technical report*, Office of Energy Efficiency and Renewable Energy and The FreedomCAR and Fuel Partnership, 2009.
161. E. Zintl and G. Brauer, *Z. Elktrochem. Angew. P.*, 1935, 41, 102-107.
162. A. Rabenau and H. Schulz, *J. Less-Common. Met.*, 1976, 50, 155-159.
163. M. Mali, J. Roos and D. Brinkmann, *Phys. Rev. B*, 1987, 36, 3888-3890.
164. H. J. Beister, S. Haag, R. Kniep, K. Strossner and K. Syassen, *Angew. Chem. Int. Ed.*, 1988, 27, 1101-1103.
165. D. E. Sands, D. H. Wood and W. J. Ramsey, *Acta Crystallogr.*, 1963, 16, 316-&.
166. E. Zintl and G. Brauer, *Z. Elktrochem. Angew. P.*, 1935, 41, 297-303.
167. W. Li, G. Wu, C. M. Araujo, R. H. Scheicher, A. Blomqvist, R. Ahuja, Z. Xiong, Y. Feng and P. Chen, *Energy Environ. Sci.*, 2010, 3, 1524-1530.
168. O. Ruff and H. Goerges, *Ber. Dtsch. Chem. Ges.*, 1911, 44, 502-506.
169. D. J. Bull, N. Sorbie, G. Baldissin, D. Moser, M. T. F. Telling, R. I. Smith, D. H. Gregory and D. K. Ross, *Faraday. Discuss.*, 2011, 151, 263-270.
170. P. Chen, Z. T. Xiong, J. Z. Luo, J. Y. Lin and K. L. Tan, *Nature*, 2002, 420, 302-304.
171. P. Chen, Z. T. Xiong, J. Z. Luo, J. Y. Lin and K. L. Tan, *J. Phys. Chem. B*, 2003, 107, 10967-10970.
172. T. Ichikawa, S. Isobe, N. Hanada and H. Fujii, *J. Alloys Compd.*, 2004, 365, 271-276.
173. E. Weidner, D. J. Bull, I. L. Shabalin, S. G. Keens, M. T. F. Telling and D. K. Ross, *Chem. Phys. Lett.*, 2007, 444, 76-79.
174. D. J. Bull, E. Weidner, I. L. Shabalin, M. T. F. Telling, C. M. Jewell, D. H. Gregory and D. K. Ross, *Phys. Chem. Chem. Phys.*, 2010, 12, 2089-2097.
175. L. Fernandez-Albanesi, P. Arneodo Larochette and F. C. Gennari, *J. Power. Sources.*, 2012, 197, 210-217.
176. R. Demir-Cakan, W. S. Tang, A. Darwiche and R. Janot, *Energy Environ. Sci.*, 2011, 4, 3625-3631.
177. G. L. Xia, D. Li, X. W. Chen, Y. B. Tan, Z. W. Tang, Z. P. Guo, H. K. Liu, Z. W. Liu and X. B. Yu, *Adv. Mater.*, 2013, 25, 6238-6244.
178. A. W. Titherley, *J. Chem. Soc. Trans.*, 1894, 65, 504-522.
179. I. P. Jain, P. Jain and A. Jain, *J. Alloys Compd.*, 2010, 503, 303-339.
180. Y. H. Hu and E. Ruckenstein, *J. Phys. Chem. A*, 2003, 107, 9737-9739.
181. T. Ichikawa, N. Hanada, S. Isobe, H. Y. Leng and H. Fujii, *J. Phys. Chem. B*, 2004, 108, 7887-7892.
182. A. L. Ortiz, W. Osborn, T. Markmaitree and L. L. Shaw, *J. Alloys Compd.*, 2008, 454, 297-305.
183. Z. T. Xiong, G. T. Wu, H. J. Hu and P. Chen, *Adv. Mater.*, 2004, 16, 1522-+.
184. L. Weifang, *J. Alloys Compd.*, 2004, 381, 284-287.
185. B. X. Dong, Y. L. Teng, J. Ge, L. Song and S. Y. Zhang, *RSC Adv.*, 2013, 3, 16977-16980.
186. Y. F. Liu, C. Li, B. Li, M. X. Gao and H. G. Pan, *J. Phys. Chem. C*, 2013, 117, 866-875.

187. L. F. Albanesi, P. A. Larochette and F. C. Gennari, *Int. J. Hydrog. Energy*, 2013, 38, 12325-12334.
188. L. H. Jepsen, D. B. Ravnsbaek, C. Grundlach, F. Besenbacher, J. Skibsted and T. R. Jensen, *Dalton. Trans.*, 2014, 43, 3095-3103.
189. B. Bogdanovic and M. Schwickardi, *J. Alloys Compd.*, 1997, 253, 1-9.
190. B. Bogdanovic, R. A. Brand, A. Marjanovic, M. Schwickardi and J. Tolle, *J. Alloys Compd.*, 2000, 302, 36-58.
191. J. J. Vajo, S. L. Skeith and F. Mertens, *J. Phys. Chem. B*, 2005, 109, 3719-3722.
192. W. I. F. David, M. O. Jones, D. H. Gregory, C. M. Jewell, S. R. Johnson, A. Walton and P. P. Edwards, *J. Am. Chem. Soc.*, 2007, 129, 1594-1601.
193. H. O. A. Gotoh, R. Nagai, S. Mochizuki, T. Kudo, *US Patent*, 1983, 4 411 971
194. M. Matsuo, T. Sato, Y. Miura, H. Oguchi, Y. Zhou, H. Maekawa, H. Takamura and S.-i. Orimo, *Chem. Mat.*, 2010, 22, 2702-2704.
195. A. Borgschulte, M. O. Jones, E. Callini, B. Probst, S. Kato, A. Zuettel, W. I. F. David and S.-i. Orimo, *Energy Environ. Sci.*, 2012, 5, 6823-6832.
196. R. A. Davies and P. A. Anderson, *Int. J. Hydrog. Energy*, 2015, 40, 3001-3005.
197. R. A. Davies, D. R. Hewett, E. Korkiakoski, S. P. Thompson and P. A. Anderson, *J. Alloys Compd.*, 2015, DOI: 10.1016/j.jallcom.2014.12.130.
198. R. A. Davies, D. R. Hewett and P. A. Anderson, *Advances in Natural Sciences: Nanoscience and Nanotechnology*, 2015, 6.
199. B. Li, Y. F. Liu, C. Li, M. X. Gao and H. G. Pan, *J. Mater. Chem.*, 2014, 2, 3155-3162.
200. H. Cao, J. Wang, Y. Chua, H. Wang, G. Wu, Z. Xiong, J. Qiu and P. Chen, *J. Phys. Chem. C*, 2014, 118, 2344-2349.
201. H. Sattlegger and H. Hahn, *Z. Anorg. Allg. Chem.*, 1971, 379, 293-299.
202. R. Marx, *J. Solid. State. Chem.*, 1997, 128, 241-246.
203. R. Marx, *J. Alloys Compd.*, 1997, 256, 196-206.
204. R. Marx, *Eur. J. Solid State Inorg. Chem.*, 1998, 35, 197-209.
205. R. Marx, *Z. Naturforsch. B.*, 1995, 50, 1061-1066.
206. R. Marx and R. M. Ibberson, *J. Alloys Compd.*, 1997, 261, 123-131.
207. R. Marx and H.-M. Mayer, *J. Solid. State. Chem.*, 1997, 130, 90-96.
208. R. Marx and H. M. Mayer, *Z. Naturforsch. B.*, 1996, 51, 525-530.
209. R. Marx and H. M. Mayer, *Z. Naturforsch. B.*, 1995, 50, 1353-1358.
210. P. Hartwig, W. Weppner and W. Wichelhaus, *Mater. Res. Bull.*, 1979, 14, 493-498.
211. R. Bloch and H. Moller, *Z. Phys. Chem. A-Chem. T.*, 1931, 152, 245-U245.
212. R. J. Cava, F. Reidinger and B. J. Wuensch, *Solid. State. Commun.*, 1977, 24, 411-416.
213. P. Hartwig, W. Weppner, W. Wichelhaus and A. Rabenau, *Solid. State. Commun.*, 1979, 30, 601-603.
214. A. K. Cheetham and P. Day, *Solid State Chemistry: Techniques*, Oxford University Press, 1st edn., 2001.
215. M. Laue, *Ann. Phys.*, 1913, 41, 989-1002.
216. W. L. Bragg and J. J. Thomson, *Proc. Annu. Power. Sources. Conf.*, 1914, 17, 43-57.
217. X. Suryanarayana and M. G. Norton, *X-ray diffraction a practical approach*, Springer, 1998.
218. W. J. Moore, *Physical Chemistry*, Longman: London, 1972.
219. C. Hammond, *The Basics of Crystallography and Diffraction*, Oxford University Press: Oxford, 2001.
220. E. H. Kisi and C. J. Howard, *Applications of Neutron Powder Diffraction*, Oxford Science Publications, 2008.
221. H. M. Rietveld, *Acta Crystallogr.*, 1966, S 21, A228-&.
222. H. M. Rietveld, *Acta Crystallogr.*, 1967, 22, 151-&.
223. H. M. Rietveld, *J. Appl. Crystallogr.*, 1969, 2, 65-&.
224. R. A. Young, *The Rietveld Method*, IUCr Monographs on Crystallography, Oxford University Press, 1993.
225. A. C. Larson and R. B. Von Dreele, *GSAS: General Structure Analysis System, user manual*, Los Alamos National Laboratory, 2004.
226. A. Coelho, *Topas technical reference manual*, Bruker AXS, 2005.

227. R. W. Cheary, A. A. Coelho and J. P. Cline, *J. Res. Natl. Inst. Stan.*, 2004, 109, 1-25.
228. J. R. Macdonald, *Impedance Spectroscopy: Emphasizing solid materials and systems*, John Wiley & Sons, 1987.
229. J. T. S. Irvine, D. C. Sinclair and A. R. West, *Adv. Mater.*, 1990, 2, 132-138.
230. J. H. Slutyers, *Recl. Trav. Chim. Pay-B.*, 1960, 79, 1092-1096.
231. J. E. Bauerle, *J. Phys. Chem. Solids.*, 1969, 30, 2657-&.
232. Armstron.Rd, *J. Electroanal. Chem.*, 1974, 52, 413-419.
233. R. D. Armstrong and K. Taylor, *J. Electroanal. Chem.*, 1975, 63, 9-17.
234. D. Johnson, *ZView: a Software Program for IES Analysis*, 2008, 2.8.
235. B. A. Boukamp and R. A. Huggins, *Mater. Res. Bull.*, 1978, 13, 23-32.
236. R. J. Abraham, J. Fisher and P. Loftus, *Introduction to NMR Spectroscopy*, John Wiley & Sons LTD 1991.
237. M. E. Smith and E. R. H. van Eck, *Prog. Nucl. Mag. Res. Sp.*, 1999, 34, 159–201.
238. H. A. Szymanski, *Raman Spectroscopy : Theory and Practice*, Plenum Publishing Corporation 1970.
239. M. Linscheid, *Mass Spectrometry. Ullmann's Encyclopedia of Industrial Chemistry*, Wiley, 2001.
240. F. A. Mellon, R. Self, J. R. Startin and P. S. Belton, *Introduction to Principles and Practice of Mass Spectrometry*, RSC Publishing, 2000.
241. A. Blazek, *Thermal Analysis*, Van Nostrand Reinhold Company, 1973.